BURN CONTROL MECHANISMS IN TOKAMAK FUSION REACTORS

A Dissertation
Presented to
The Academic Faculty

By

Maxwell Donald Hill

In Partial Fulfillment
of the Requirements for the Degree
Doctor of Philosophy in the
Nuclear and Radiological Engineering Program

Georgia Institute of Technology

May 2019

BURN CONTROL MECHANISMS IN TOKAMAK FUSION REACTORS

Approved by:

Dr. Weston Stacey, Advisor
Department of Nuclear Engineering
Georgia Institute of Technology

Dr. Bojan Petrovic
Department of Nuclear Engineering
Georgia Institute of Technology

Dr. Dan Kotlyar
Department of Nuclear Engineering
Georgia Institute of Technology

Dr. Thomas Petrie
Research Scientist
General Atomics, San Diego

Dr. Eugenio Schuster
Department of Mechanical
Engineering and Mechanics
Lehigh University

Date Approved: December 7, 2018

“Sometimes science is more art than science, Morty. A lot of people don’t get that.”

Rick Sanchez

ACKNOWLEDGEMENTS

First, I would like to express my sincere gratitude to my advisor, Professor Weston Stacey, for his guidance and mentorship during my doctoral work. Besides my advisor, I would like to thank the rest of my thesis committee: Professor Petrovic, Professor Kotlyar, Professor Schuster, and Dr. Petrie, for their insightful comments and encouragement.

I would like to thank my fellow graduate students in the Fusion Research Center for their feedback, cooperation, and friendship and wish them the best of luck in their future endeavors. A special mention for Richard King is needed, as his willingness to share his superior mathematical talents resulted in creative solutions to many problems that may otherwise have gone unsolved.

My tenure as a graduate student was enriched by my participation in the Ti:GER program. I would like to thank my Ti:GER team for the good times we shared as we developed and pitched the idea that building a multibillion-dollar fusion-fission hybrid reactor was a viable and economical solution to the nuclear waste problem. Thanks also to Professor Marie Thursby for creating the program and to Margi Berbari and Anne Rector for their guidance and assistance during my time in the program.

I would like to thank my many friends in The Noble Order of the Gray Duck for the radical intellectual growth I have experienced through our countless challenging and entertaining conversations.

Last but not least, I would like to thank and acknowledge my wife, Rebecca, without whose loving support and encouragement I would not have even started a PhD program, much less completed one.

TABLE OF CONTENTS

LIST OF TABLES

LIST OF FIGURES

DESCRIPTION OF CODES REFERENCED

GT3

GT3, short for Georgia Tech Tokamak Tools, is a new tokamak analytics code that unifies and extends the functionality of most codes developed and used by the Fusion Research Center (FRC) at Georgia Tech, including calculations related to ion orbit loss, neutral beam deposition, thermal instability onset, impurity radiation, and radial transport. It interfaces with NEUTPY for neutral particle transport calculations.

NEUTPY

NEUTPY is a python implementation of the two-group transmission escape probability (TEP) neutral transport methodology previously used in the GTNEUT code. Neutpy calculates neutrals densities and ionization rates everywhere in the plasma chamber. It is described in greater detail in Appendix C.

ADPAK

The ADPAK atomic physics routines, developed by Russell Hulse, are used to obtain the ionization and recombination rates for each charge state of various ion species. These are then used to obtain relative charge state densities and power loss from impurity radiation.

STRAHL

STRAHL is an interactive, stand-alone impurity transport code which is used to interpret spectroscopic measurements. It calculates the impurity ionization balance on the basis of given plasma parameters and empirical transport models, and specially designed atomic physics data sets. Although not used explicitly in the course of this thesis, conclusions about impurity transport that were arrived at using STRAHL are described in Chapter 4.

RAYTEC

RAYTEC is an electron cyclotron radiation (ECR) transport code developed by Ferran Albajar to investigate ECR in plasmas with arbitrary cross section. It is dicussed in greater detail in Chapter 3.

SUMMARY

The D-T fusion cross section has a significantly positive temperature dependence in the range of temperatures that ITER is expected to operate in. As a result, ITER must have active and preferably also passive control mechanisms that will limit inadvertent plasma power excursions that could trigger runaway fusion heating. Existing predictions of thermal stability are based on models that fail to consider many important physics mechanisms, and the impending operation of ITER provides a strong incentive to revisit this issue. We have identified and investigated the potential of several "burn control" mechanisms including electron cyclotron radiation (ECR), ion-orbit loss (IOL), impurity seeding, and Multi-faceted Asymmetric Radiation From the Edge (MARFE) instabilities that could limit sudden increases in fusion power in the inner core.

ECR is the most significant passive burn control mechanism identified, and it becomes particularly important at higher temperatures (30+ keV). EC losses are a function of wall reflectivity and the amount of EC radiation that is generated in the inner core and absorbed elsewhere in the plasma. Because ECR generated in the core by hot electrons can be absorbed in other plasma regions, it can function as an instantaneous transfer of power from fusion α particles in the central core to other regions of the plasma. This would have the effect of instantaneously cooling the center of the plasma and heating the outer core and edge regions, in contrast with the way energy transport is typically modeled.

Several active burn control mechanisms are also investigated including adjusting fuel pellet composition, controlling impurity concentrations using on-axis EC current drive, and deliberate MARFE-initiated H-L transitions.

Finally, it is concluded that we have likely exhausted the utility of simple 0-D treatments of the plasma for modeling burn control scenarios, and that these should be replaced with multi-nodal dynamics models that treat various important plasma regions in a more granular way. The equations for such a model are developed using two nodes for the confined

plasma, one node for the scrape-off layer, and one node for the divertor regions.

CHAPTER 1
INTRODUCTION

Albert Einstein's famed equation for the equivalence of mass and energy [1]

$$E = mc^2 \tag{1.1}$$

has, over the last 112 years, served as the basis for a significant expansion in technologies with which we can satisfy the ever-expanding demand of our species for electricity. One of the most promising of those technologies is nuclear fusion, in which hydrogen atoms are fused to produce helium, neutrons, and a significant amount of energy.

1.1 Fusion

Every atomic nucleus has less mass than the sum of the masses of the protons and neutrons that comprise it. The difference in mass was converted to energy and lost from the system in order to form a bound state, just as a ball held above the ground must lose energy to form a "bound" state with the Earth. That amount of energy, the "binding energy," (BE) of the nucleus is the amount of energy that must be lost from a system of particles to form a bound nucleus, or the amount of energy that must be added back into the nucleus to get separate constituent particles. The BE can be calculated according to Equation 1.1, where m is the mass difference. For example, a helium nucleus (also known as an α-particle) weighs about 4.8×10^{-29} kg less than the sum of the masses of the protons and neutrons that comprise it. According to Equation 1.1, an α-particle has a binding energy of about 28.3 MeV or 4.534×10^{-12} Joules.

We can a good idea of how tightly bound a nucleus is by looking at the total amount of binding energy in a nucleus divided by the number of particles (nucleons) that that energy

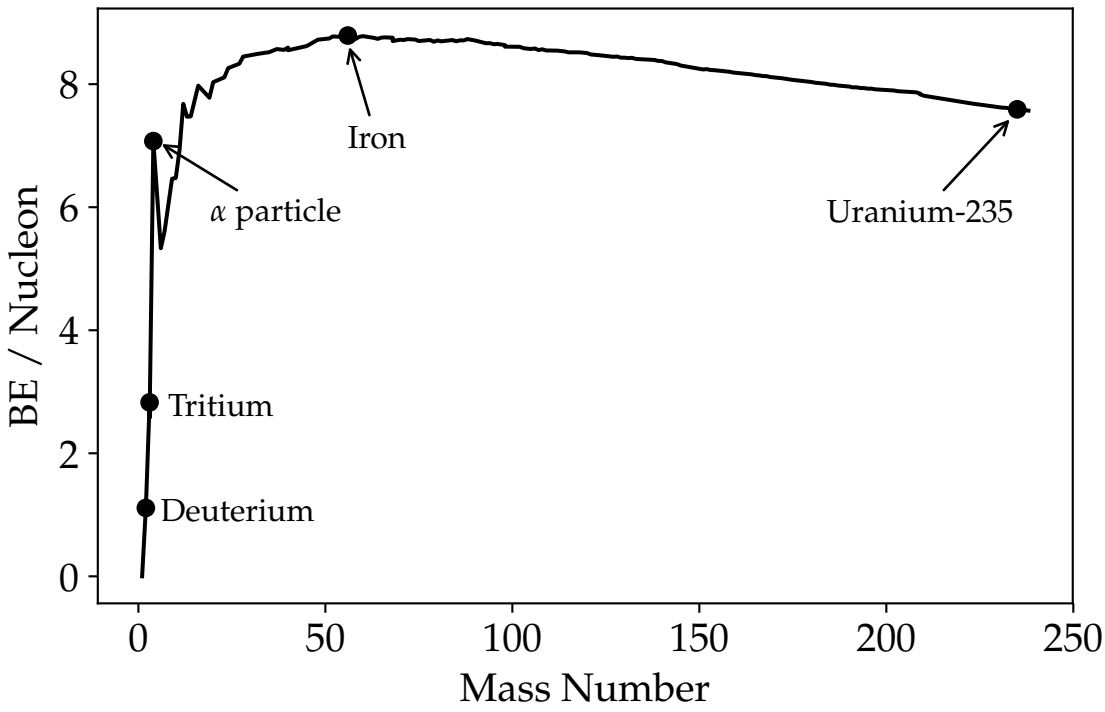

Figure 1.1: The binding energy per nucleon for common isotopes.

is binding. The binding energy per nucleon for common elements is shown in Figure 1.1. The more BE per nucleon for a given nucleus, the more energy would have to be added to split the nucleus into its component protons and neutrons. In other words, the higher the BE per nucleon, the more stable the nucleus.

If a collection of nucleons, bound to other nucleons or otherwise, can be rearranged such that the system becomes more stable, energy is necessarily released from the system in an amount equal to the BE of the more stable state minus the BE of the less stable state. This energy is released either in the form of electromagnetic radiation or as the kinetic energy of the resulting particles.

Consider the interaction between two isotopes of hydrogen, deuterium (1 proton, 1 neutron) and tritium (1 proton, 2 neutrons). Deuterium has a BE of 2.224 MeV and tritium has a BE of 8.48 MeV. As illustrated in Figure 1.1, an α-particle is an unusually stable combination of nucleons. If a deuterium nucleus and a tritium nucleus could be rearranged

(in this case, fused) to form an α-particle and a neutron (no binding energy), $(28.3 + 0) - (2.224 + 8.48) \sim 17.6$ MeV could be release from the system in the form of the kinetic energy in the α-particle and neutron. To release that 17.6 MeV by fusing hydrogen into helium, capture the released energy, and convert it into electricity at an economical scale, has been the goal of most peaceful fusion research to date.

1.2 Magnetic Confinement Fusion Research

To fuse deuterium and tritium (or any other two nuclei), the two nuclei must be close enough that the strong nuclear force in each nucleus can act on the nucleons of the other. Unfortunately, the Coulomb repulsion between the two positively charged nuclei makes this difficult. To overcome the Coulomb repulsion, the two nuclei must have a significant amount of kinetic energy.

The most obvious way to fuse hydrogen might be to use a particle accelerator, however this is far too expensive and produces far too few fusion events to be practical as a power source. An alternative approach is to take a volume of hydrogen, and heat it up to the point that hydrogen will fuse often enough through random collisions that a meaningful amount of energy can be generated. The latter approach has been, and continues to be the most promising approach to generating fusion power, both terrestrially and in the heavens.

An analysis similar to the one at the beginning of this chapter reveals that the binding energy between a nucleus and its electrons is rather small in comparison to nuclear binding energies ($\sim$ 13.6 eV for the electron of a hydrogen atom). The energies necessary to overcome the Coulomb repulsion are several orders of magnitude greater, which means that the electrons will have already been stripped off of any hydrogen nuclei that have the energy necessary to fuse. A volume of gas that consists primarily of separate ions and electrons is known as a plasma. Because of the unusual behavior of plasma in response to electromagnetic fields, it is generally regarded as the fourth state of matter.

The use of magnetic fields to confine, control, and even heat the plasma, has been an

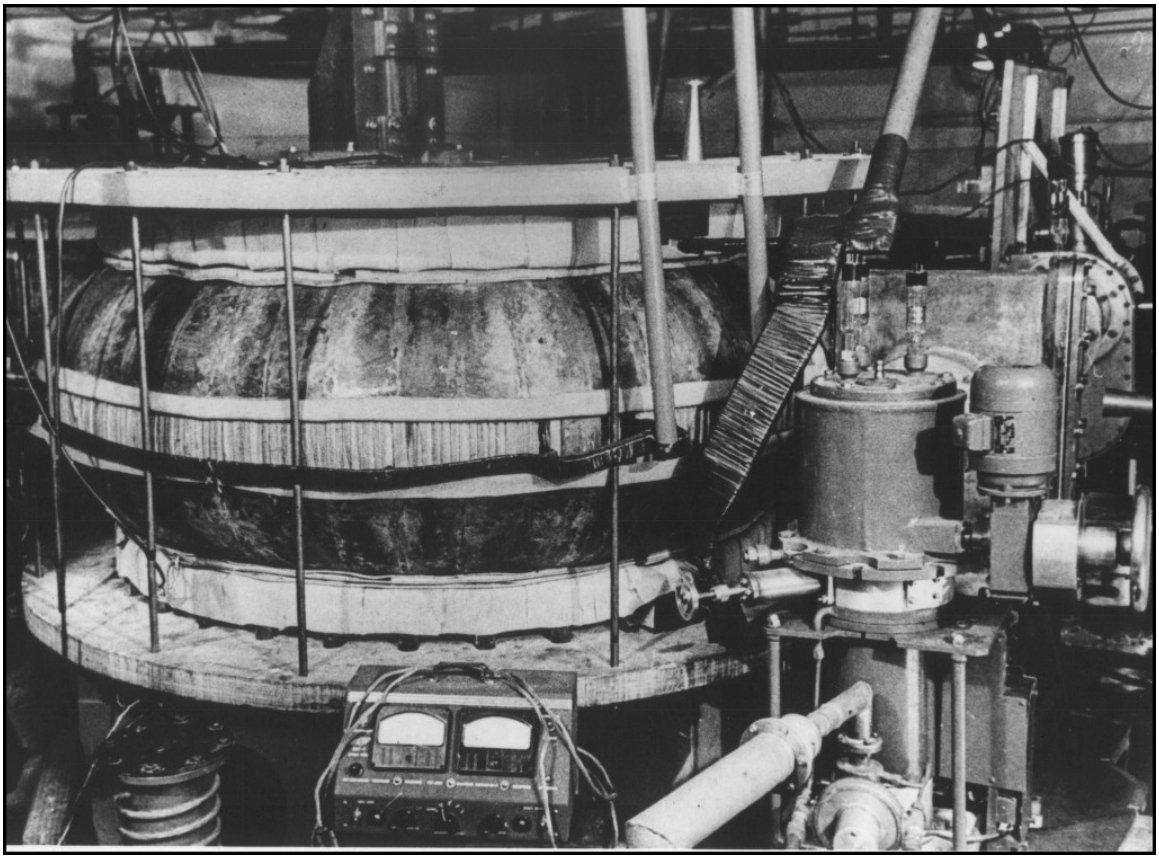

Figure 1.2: The first tokamak, the T-1, began operation in Russia in 1958. It had a major radius of 0.67 m, a minor radius of 0.17 m, a toroidal magnetic field strength of 1.5 T, and a plasma current of 100 kA [3].

area of active research since the 1950's. Since then, a variety of magnetic field configurations have been explored. Of these devices, the most successful has been a design first developed in Russia known as a tokamak.

1.3 Tokamaks

Tokamak is a transliteration of the Russian acronym токамак, which was coined by Igor Golovin and stands for тороидальная камера с магнитными катушками, which means "toroidal chamber with magnetic coils." [2] A picture of the first tokamak, T-1, is shown in Figure 1.2

Tokamaks confine the plasma, which is far too hot to be allowed to regularly come into contact with the reactor walls, using a series of magnetic fields. The strongest of these

fields is the toroidal field, which is generated by several coils going around the torus (current flowing in the poloidal direction). A poloidal field is superimposed onto the toroidal field, and is generated primarily by passing a current through the plasma itself in the long, toroidal direction. The superimposed poloidal field causes field lines to spiral around the plasma. Spiralled field lines force plasma ions and electrons to spend approximately the same amount of time in the upper half of the plasma as the lower half. This is necessary to offset the oppositely directed upward and downward "drift" motion of ions and electrons resulting from the curved and non-uniform toroidal field that would otherwise make it impossible to confine the plasma. So although a strong toroidal field is necessary to create the geometry and for other stability-related reasons, it is, in fact, the poloidal field driven by the plasma current that is primarily responsible for enabling a tokamak to confine a plasma.

Additional contributions to the poloidal field are created by a central solenoid and large "ring" coils above, below, and radially outboard of the plasma. The central solenoid exists primarily to induce the current in the plasma at startup, and the ring coils exist primarily for shaping the plasma and stabilizing its position, however both contribute somewhat to the poloidal field strength inside the plasma. These fields and the electromagnets that create them are illustrated in Figure 1.3.

The densities and temperatures of plasma ions and electrons are not uniform within the plasma. Rather, they tend to be peaked in the center of the plasma, i.e. $\rho \sim 0$, where ρ is the normalized minor radius of the torus. As a result, most fusion power production occurs primarily in the "inner core" of the plasma, where $\rho \lesssim 0.5 - 0.6$. The region of plasma where $\sim 0.6 \lesssim \rho \lesssim 0.9$ is known as the "outer core" and the plasma "edge" refers to the region where $\rho \gtrsim 0.9$, which is usually characterized by steeper density and temperature gradients than those in the inner and outer cores.

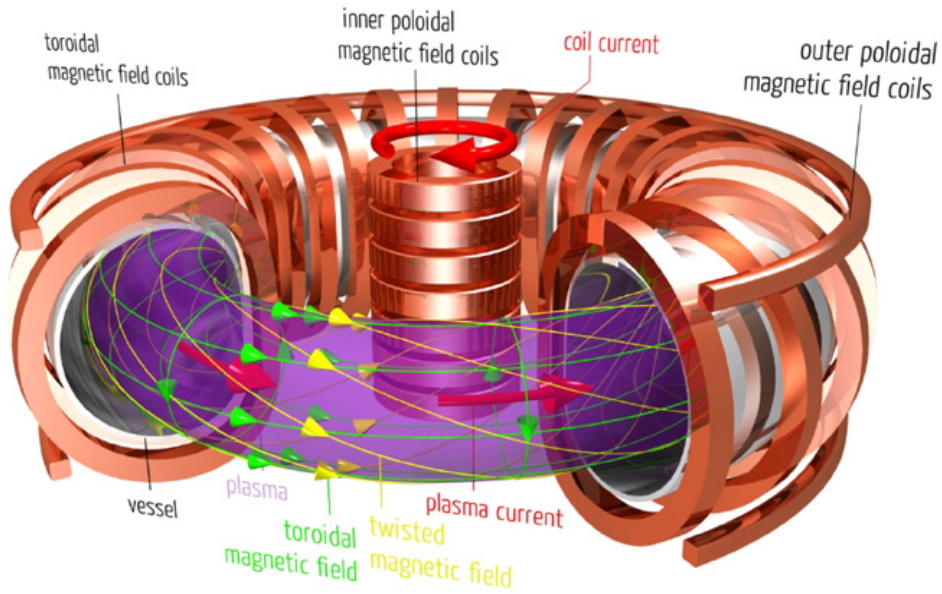

Figure 1.3: Diagram of a tokamak showing key coil systems, plasma current, magnetic fields, and other key components.

1.4 ITER and Beyond

Since the early days of tokamak research, it was known [4, 5, 6] that a tokamak capable of generating more fusion power than the power required to heat the plasma would have to be much larger than tokamaks then in existence. Planning for such a reactor over several decades has resulted in the International Thermonuclear Experimental Reactor (ITER), which is currently under construction in southern France. A diagram of ITER is shown in Figure 1.4. The goal of ITER is to demonstrate the physics and engineering requirements necessary for a demonstration fusion power reactor to be constructed.

ITER is expected to have its first plasma in 2025 [7]. For the first approximately 10 years, all of ITER's plasmas will be deuterium only, rather than the mix of deuterium and tritium discussed earlier in this chapter. Running in "D-D" mode rather than "D-T" affords researchers an opportunity to learn about the physics of the reactor without the complications of producing and managing radioactive tritium.

Additionally, because D-T fusion is much more probable than D-D fusion for most of

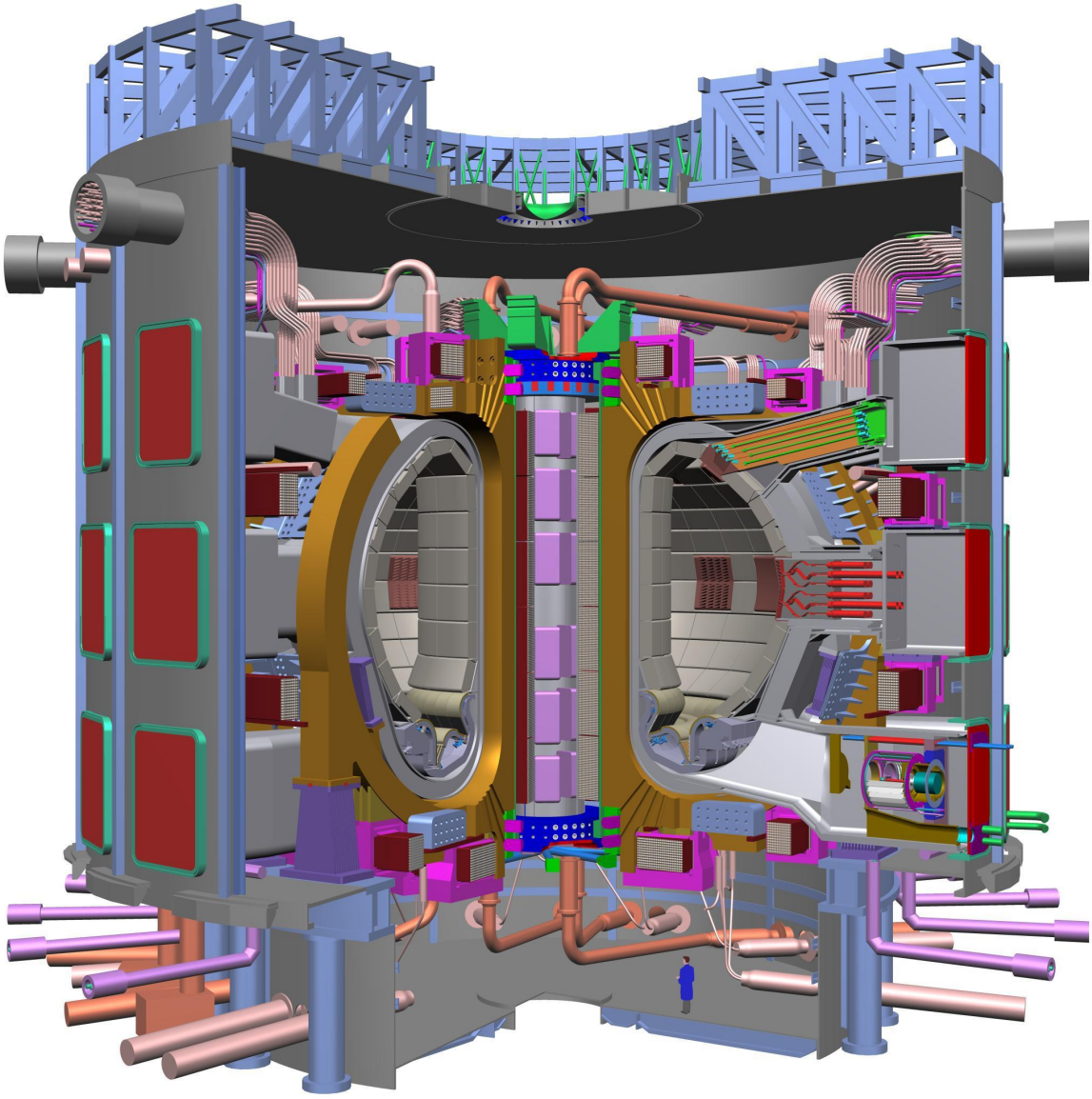

Figure 1.4: A cutaway diagram of the ITER tokamak under construction in France. Note the person underneath the reactor vessel for a sense of scale.

the relevant temperature range, D-T fusion results in a significantly larger heating source to the plasma than D-D fusion. Fusion plasmas that generate a significant amount of fusion heating power are known as "burning plasmas."

It could be said that the "holy grail" of fusion research is to operate a reactor in such a way that the vast majority of the necessary heating power to keep the plasma at the necessary temperature is provided by fusion within the plasma itself. This condition is known as "ignition." So long as fresh fuel (deuterium and tritium) is constantly delivered to the plasma and the materials surrounding the plasma remain in good condition, such a reactor could operate in steady-state for months or even years with comparatively little additional power input. Although operating at ignition is conceivably possible, fusion reactors will generally be operated in steady-state with a small amount of external heating power for control purposes.

Although ITER is not designed to achieve ignition, it will achieve a Q_P (the ratio of fusion power to external power) of greater than 10. Furthermore, it will demonstrate important burning plasma physics that have heretofore been explored in theory only. This thesis explores some important dynamical phenomena that can occur in a burning plasma such as those that will be present in ITER and in subsequent fusion power reactors.

CHAPTER 2

GLOBAL STABILITY AND BURN CONTROL

2.1 Global Dynamics Equations

Many dynamic tokamak phenomena can be understood in the context of a relatively simple set of 0-D particle and power balance equations such as those shown below [8].

$$\frac{dn_i}{dt} = S_i - \frac{1}{2}n_i^2 \left\langle \sigma v \right\rangle_f - \frac{n_i}{\tau_P^i} \tag{2.1}$$

$$\frac{dn_\alpha}{dt} = S_\alpha + \frac{1}{4}n_i^2 \left\langle \sigma v \right\rangle_f - \frac{n_\alpha}{\tau_P^\alpha} \tag{2.2}$$

$$\frac{dn_z}{dt} = S_z - \frac{n_z}{\tau_P^z} \tag{2.3}$$

$$\frac{3}{2}\frac{d}{dt}\left(n_e T_e\right) = P_\Omega + P_{aux}^e + \frac{1}{4}n_i^2 \left\langle \sigma v \right\rangle_f U_\alpha^e - Q_{ie} - P_R - \frac{3}{2}\frac{n_e T_e}{\tau_E^e} \tag{2.4}$$

$$\frac{3}{2}\frac{d}{dt}\left(n_i T_i\right) = P_{aux}^i + \frac{1}{4}n_i^2 \left\langle \sigma v \right\rangle_f U_\alpha^i + Q_{ie} - \frac{3}{2}\frac{n_i T_i}{\tau_E^i} \tag{2.5}$$

Here, n_i, n_α, and n_z, are the average hydrogen ion (deuterium + tritium), α-particle, and impurity ion densities, respectively. T_e and T_i are, respectively, the average electron and ion temperatures. The fusion reactivity, $\left\langle \sigma v \right\rangle_f$, is discussed more in subsequent sections. The quantities τ_P^i, τ_P^α, τ_P^z, τ_E^e, and τ_E^i, are the ion, α-particle, and impurity particle confinement times and electron and ion energy confinement times, respectively. Q_{ie} is the collisional energy transfer from electrons to ions. If the local ion temperature is hotter than the local

electron temperature, then Q_{ie} will be negative. Q_{ie} can be calculated from [8]

$$Q_{ie} = \frac{n_i n_e \left(e_i e_e\right)^2 m_e \ln\left(\Lambda\right) \left(1 - \frac{T_i}{T_e}\right)}{2\pi\epsilon_0^2 \left(2\pi m_e T_e\right)^{1/2} m_i \left[1 + \frac{4\sqrt{\pi}}{3}\left(\frac{3m_e T_i}{2m_i T_e}\right)^{3/2}\right]} \tag{2.6}$$

Of particular interest to the problem of controlling the burn condition in a D-T fusion reactor are the fusion-α heating terms in Equations 2.4 and 2.5. The amount of plasma heating is a function of the fuel density (n_i), the probability of fusion occurring ($\langle\sigma v\rangle_f$), and the amount of the fusion energy that is released in the form of kinetic energy of the α-particle (U_α = 3.5MeV [8]). That 3.5 MeV is subsequently transferred first to the electrons (U_α^e), and later to the ions (U_α^i) after the α particle has slowed down significantly. Because of the high energy of the α particles, almost all of their energy is collisionally transferred to the electron population.

To avoid complications associated with the use of tritium, current experiments typically use deuterium or helium plasmas in which very little fusion takes place at currently achievable temperatures. Consequently, the fusion-α terms in the power balance equations (as well as the α-particle balance equation) can safely be neglected in present experiments. In ITER and other future reactors, not only will the fusion-α heating terms be important, but they will also represent the primary (or only) heating source for the reactor after startup [9]. As discussed in Chapter 1, the condition in which a fusion reactor generates all the energy necessary to heat itself and requires only new fuel is called "ignition." Fusion reactors are expected to operate somewhat sub-ignited for reasons related to the control of the reactor.

Like all tokamaks, ITER will present many control-related challenges [10], including those introduced by the presence of a strong fusion-α heating source. "Burn control" is the area of research that is principally concerned with controlling this heating source and understanding the implications that control actions may have on the global power balance. It is within that subcategory of fusion reactor research that this thesis falls.

The purpose of this chapter is to explore the history of burn control research and de-

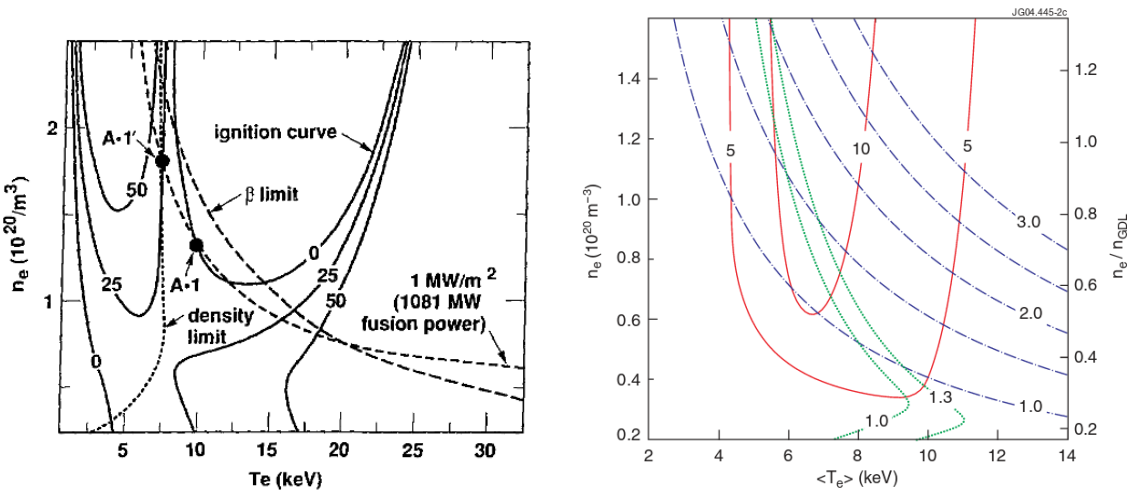

(a) Early POPCON analysis for ITER [11]. The numbers on the contours indicate the amount (MW) of auxiliary heating power necessary to maintain equilibrium.

(b) More Recent POPCON analysis for ITER [12]. The red lines are contours of constant fusion gain, the blue lines are constant normalized beta, and the green lines are constant heating power (MW) as a fraction of the power necessary to stay in H-mode.

Figure 2.1: Examples of POPCON analyses that have been done for ITER.

scribe the motivation for this project.

2.2 History of Burn Control Research

Global stability can be explored in several different ways using Equations 2.1 through 2.5. One technique that has been used extensively throughout the study of fusion reactor stability is to fix density and temperature and solve for the auxiliary heating power necessary to satisfy the balance equations [8]. Repeating this analysis for a range of densities and temperatures results in contours in n-T space of constant heating power needed to maintain the sub-ignition fusion plasma. Other useful quantities that are functions of density and temperature (fusion gain, β, etc.) can also be plotted. These plots became known as Plasma Operating Contours, or POPCONS. An example of an early POPCON plot for ITER is shown in Figure 2.1a [11]. A more recent POPCON plot for ITER is shown in 2.1b [12].

Several insights about the desirability and stability of various potential operating points

can be obtained from these plots. For example, Figure 2.1a identifies two potential operating points: A-1, which would achieve ignition and another point A-1', which would afford greater control of the burn condition than a fully-ignited plasma.

The stability of the system against temperature perturbations can also be analyzed. For example, if an ITER discharge was in a stable equilibrium at operating point A-1' in Figure 2.1a and experienced a sudden increase in temperature, it would move to a contour on which less power would be needed to maintain the equilibrium. Without a rapid reduction in heating power, this could result in the plasma reaching an operating point at which more heating power was available than was necessary to maintain a stable equilbrium. This would increase the temperature of the plasma, which could result in further heating power increases. Based on the assumptions that went into the POPCON plot of Figure 2.1a, it could be said that the point A-1' may be unstable against thermal power excursions. Furthermore, the proximity of the A-1' operating point to the β-limit suggests that a power excursion would almost certainly result in a disruption.

Figure 2.1b plots somewhat different quantities. Here, the red lines are fusion gain, the blue lines are normalized beta, and the green lines are heating power as a fraction of the power necessary to stay in H-mode. Based on the confinement assumptions that went into making this POPCON plot, it would be predicted that an operating point at around 8 keV and a density at approximately 80% of the Greenwald density limit [13] would be stable against thermal power excursions, as an increase in temperature would move the operating point into a region characterized by reduced fusion gain.

Presently, most fusion researchers [14] expect ITER to have access to globally stable operating points, based mostly on early stability studies. However, the impending operation of ITER provides a strong incentive to revisit this issue.

2.3 Energy Transfer Following a Fusion Event

The sequence of events involved in a fusion event are typically thought of as follows:

1. A fusion reaction occurs, consuming a deuterium ion and a tritium ion, and creating a 3.5 MeV α-particle and a 14.1 MeV neutron. Both the α-particles and the neutrons are distributed isotropically in direction.

2. The neutron streams out of the plasma, which has a negligible fast neutron macroscopic cross section. It is absorbed in the surrounding first wall or breeding blanket, where it is used to create tritium and its energy is captured to produce electricity.

3. The α-particle either A) leaves the plasma through direct ion orbit loss or B) is confined and transfers its energy first to electrons on or near the flux surface on which it was born and then, after it loses sufficient energy to the electrons, to the local ions.

4. Fast α-particles that are not ion orbit lost initially give their energy preferentially to the electron species. As these α-particles slow down, the fraction of the fusion power transferred directly to ions increases.

5. As the magnetically confined electrons are heated, they convert some of their energy into EC (electron cyclotron, "syncrotron") radiation, which is essentially instantaneously deposited in the first wall or reabsorbed elsewhere in the plasma. The electrons then collisionally transfer much of their remaining energy to the cooler ions. This occurs on a timescale of a couple hundred milliseconds [8]. Due to the high energy (3.5 MeV) at which α's are born, it is expected that they will give the vast majority of their energy to the core plasma electrons, and that most ion heating as a result of fusion will be through collisions with these heated electrons.

6. The direct alpha and indirect electron collisional energy transfer to the ions heats the ions, which increases the fusion rate. The deuterium and tritium ions that were consumed in fusion are replaced through neutral beam injection (NBI), pellet injection, massive gas injection, or recycling from the chamber wall.

This "reference" scenario will serve as the basis for the modeling in this chapter, although some of these assumptions will be revisited in later chapters.

2.4 Power Excursions

It has long been a matter of concern [15] that the strong positive temperature dependence of the fusion cross section raises the possibility of a positive power excursion. In such an event, a positive ion temperature perturbation in a steady-state system could increase the fusion cross section, resulting in a higher rate of fusion, which would drive the core temperature higher, etc. This process would continue until the core density and temperature found a new stable operating point or, more likely, a disruption occurred. In either case, such an unmitigated power excursion will significantly increase the heat and particle fluxes to first wall and divertor.

The temperature sensitivity of the α-heating term, which dominates the power balance in a D-T reactor, can be seen by plotting the fusion reactivity $\langle \sigma v \rangle_f$ as a function of temperature [16], as in Figure 2.2. Because derivatives on a log-scale plot are difficult to grasp intuitively, the temperature gradient and normalized temperature gradient of $\langle \sigma v \rangle_f$ are shown in Figure 2.3 for an ITER-relevant temperature range. The normalized temperature gradient of $\langle \sigma v \rangle_f$ can be interpreted as the percent change in fusion heating power (assuming constant n_i) that would result from a temperature change of 1 keV at a given temperature.

According to the plot in Figure 2.3a, a plasma with an average core temperature of 10 keV would experience an increase in the fusion heating power of between 10 and 15% for each 1 keV increase in ion temperature. That 10 or 15% could be quite significant in a discharge in which fusion α-heating is the dominant source of heating. Unchecked, that additional heating power could quickly increase the temperature further, resulting in further increases in the fusion heating power. It is not hard to envision a situation in which the core temperature could rapidly increase by 5 or even 10 keV, resulting in significant heat loads

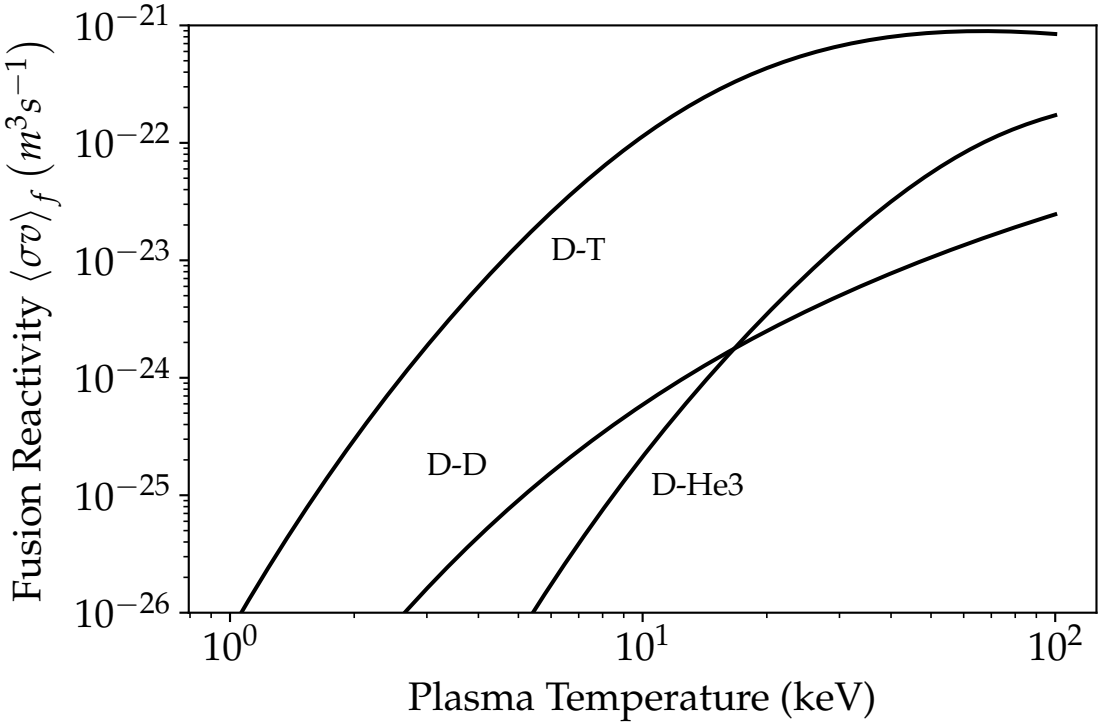

Figure 2.2: The fusion reactivity for several fusion reactions as a function of ion temperature from the Bosch-Hale model. [16]

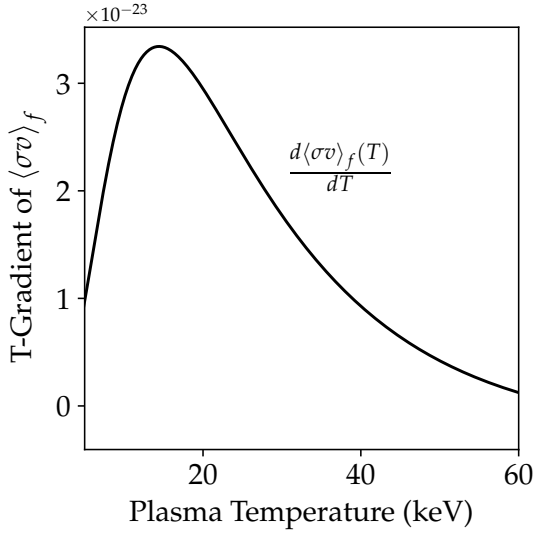

(a) The temperature derivative of the D-T fusion reactivity as a function of ion temperature.

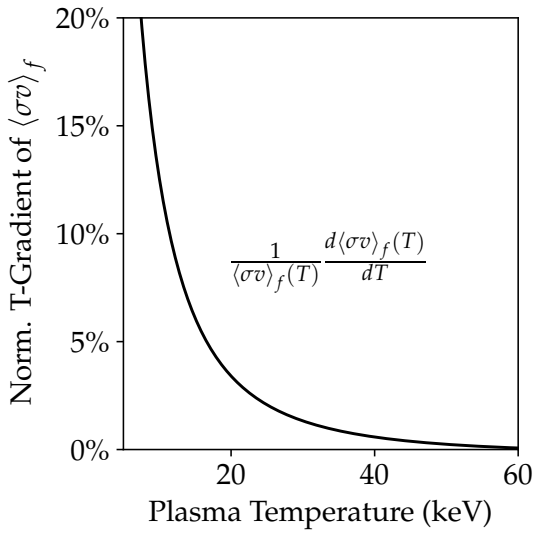

(b) The normalized temperature derivative of the D-T fusion reactivity as a function of ion temperature.

Figure 2.3: The temperature derivative and normalized temperature derivative of the fusion reactivity as functions of ion temperature.

on the divertor and a possible disruption of a plasma with even more stored energy than it had during steady-state operation.

Sudden changes in temperature that could lead to a power excursion can result from a variety of events and may not always be controllable or avoidable. Such events may include unexpected activation of heating sources, local non-homogeneities in the fuel ion density, unexpected expulsion of impurities from the core (reducing the radiative power losses from those impurities), changes to confinement characteristics, and almost certainly a variety of currently unanticipated phenomena.

Although POPCON-based analyses like those discussed in the previous section certainly provide a case for optimism, they should not be the end of our analysis. The prospect of a positive power excursion remains a significant issue for several reasons:

1. Time derivatives are set to zero when solving the equations to construct the POPCON charts [8]. As a result, they are unlikely to be useful in modeling dynamic phenomena, especially when it comes to phenomena that occur on timescales shorter than an energy confinement time, such as the fusion α energy deposition rate.

2. The IPB98(y,2) confinement time scaling law, which is often used to estimate confinement times in ITER, was constructed using data from discharges that were approximately in steady-state [9]. In a previous analysis [17], attempts to use only the IPB98(y,2) scaling law to predict shot dynamics in DIII-D largely failed to capture those dynamics without additional tuning parameters. The IPB98(y,2) scaling law was constructed to obtain reasonable predictions of equilibrium ITER performance, not to model rapidly evolving tokamak dynamics.

3. Models for the temperature dependence of the transport losses in a tokamak that are derived from the IPB98(y,2) scaling law implicitly include energy loss mechanisms that occur on a variety of timescales, some of which are longer than the timescale on which power excursions are likely to occur.

4. Global, 0-D models necessarily use an average density and temperature that is chosen to be representative of the entire plasma. The dynamics of a power excursion, however, are likely to depend primarily on the density and temperature in the hotter inner core.

5. There are many non-linear effects and complex temperature-dependent phenomena that occur in tokamaks that are not well-accounted for in simple models like the one represented by Equations 2.1 through 2.5. The transport of electron cyclotron (EC) radiation produced by α-heating of core electrons from the inner core to other plasma regions [18, 19], which will be further discussed in a later chapter, is an important example of such a phenomenon.

2.5 The Temperature Dependence of Transport Losses

Some investigations of ITER's thermal stability have focused on the temperature dependence of global energy loss and transport characteristics. One fit for transport losses (including radiative losses) has been derived by recasting the IPB98(y,2) scaling law [9] in terms of physics parameters. This transport losses "scaling law," which makes the temperature dependence of the IPB98(y,2) scaling law more clear is

$$P_{\text{loss}}\,(\text{MW}) = \left(1.8 \times 10^{5}\right) \frac{n_{20}^{1.6} T_{10}^{2.86} R_m^{0.11} \kappa^{0.8}}{B_T^{3.03} M^{0.37} H_H^{2.86}} \left(\frac{aB}{I}\right)^{2.6} \left(\frac{a}{R}\right)^{1.49} \tag{2.7}$$

Here, T_{10} denotes the volume average temperature in units of 10 keV, H_H is a confinement multiplier, and the other variables have their usual meanings as associated with the IPB98(y,2) scaling law given in Equation 2.15.

The ITER Physics Basis document[9] argues that the reactor is likely to be thermally stable after ignition because the transport losses in Equation 2.7, i.e.

$$P_{\text{loss}} \propto n_e^{1.6} \left(\frac{T}{H_H}\right)^{2.86} \tag{2.8}$$

scale more strongly with temperature than the fusion power, i.e.

$$P_{\text{fusion}} \propto d\left(n_e T\right)^2 \tag{2.9}$$

where d is a dilution factor $d = n_T n_D / n_e^2$ [9].

Although Equation 2.7 is not an unreasonable way to estimate equilibrium transport losses in ITER based on the results of current experiments, it ignores several factors that may be important in the event of a thermal power excursion. First, the impurity losses that are implicitly included in the IPB98(y,2) scaling law include impurity radiation in the edge regions of tokamaks. Since most fusion power generated in the inner core (an informal designation which we use to describe the region of the plasma with $\rho \lesssim$ 0.4-0.6) will take approximately an energy confinement time to reach the edge, edge radiation is unlikely to be successful in directly offsetting a core power excursion, which could occur on a timescale significantly faster than a confinement time, as will be shown in the next section. This is especially true in shots with enhanced confinement characteristics. Furthermore, the mix of impurity species in the tokamaks that created the data used in the IPB98(y,2) fit is different than the impurity mix in ITER [20]. As will be discussed in Chapter 4, the temperature dependence of impurity radiation is complex and varies significantly with the species of impurity, the local temperature, and the concentration of neutral hydrogen.

As a result of these concerns, this analysis will approach things somewhat differently. To get a better estimate of the extent to which a reduction in energy confinement can offset a power excursion in real time, the losses resulting from several power loss mechanisms will be calculated. Careful attention will be given to the timescales on which they could effect the ion temperature in the inner core, where excursions are most likely to start. The effectiveness of loss mechanisms will be quantified by comparing their effects on the fusion reactivity gain (dP_{fus}/dT). A value of dP_{fus}/dT that is approximately zero or negative would indicate thermal stability, as an increase in the temperature T would reduce the

fusion power output. Even if a negative fusion power gain cannot be achieved, any negative contributions to it will assist in the active control of the burn condition.

2.6 A Simple Model of a Thermal Power Excursion

To quantify the magnitude and timescale of this problem based on the reference scenario described above, a simple model was constructed based on Equations 2.1 through 2.5. The ion particle balance was used as shown in equation 2.1. The ion and electron power balance equations were combined into a single global equation and solved for an equation for the evolution of the global temperature, where it is assumed that T_i = T_e = T. The resulting equations, which can be readily solved for n_i and T as functions of time, are shown below.

$$\frac{dn_i}{dt} = S_i - \frac{1}{2}n^2 \left\langle \sigma v \right\rangle_f - \frac{n}{\tau_P} \tag{2.10}$$

$$\frac{dT}{dt} = \frac{2}{3}\left(\frac{P_{\text{aux}} - P_{\text{R}}}{n} + \frac{1}{4}n \left\langle \sigma v \right\rangle_f U_\alpha - \frac{3}{2}\frac{T}{\tau_E}\right) - T\left(\frac{S_i}{n} - \frac{1}{2}n \left\langle \sigma v \right\rangle_f - \frac{1}{\tau_P}\right) \tag{2.11}$$

A steady-state solution to these equations was found using parameters representative of a steady-state ITER discharge [21]. The global particle confinement time τ_P was set equal to the energy confinement time τ_E, for which a typical value found in the literature of 3.7 seconds was used [22]. ~40 MW of beam heating power and ~47 MW of radiated power were assumed constant. Holding the radiated power constant rather than increasing it with temperature results in a deliberately conservative model, against which specific radiative loss mechanisms can be benchmarked. The fusion reactivity was calculated using the widely-used Bosch-Hale model [16], which is reproduced in Equations 2.12 through 2.14. Table 2.1 contains the coefficients for several fusion reactivities.

$$\left\langle \sigma v \right\rangle_f = C_1 \theta \sqrt{\xi / \left(m_r c^2 T^3\right)} e^{-3\xi} \tag{2.12}$$

Table 2.1: Coefficients for the Bosch & Hale fusion reactivity fit for several types of fusion events

Coefficient	$\mathrm{T(d,n)\,^4He}$	$\mathrm{^3He(d,p)\,^4He}$	$\mathrm{D(d,p)T}$	$\mathrm{D(d,n)\,^3He}$
B_G ($\sqrt{\mathrm{keV}}$)	34.3827	68.7508	31.3970	31.3970
$m_r c^2$ (keV)	1 124 656	1 124 572	937 814	937 814
C_1	$1.173\,02 \times 10^{-9}$	$5.510\,36 \times 10^{-10}$	$5.657\,18 \times 10^{-12}$	$5.433\,60 \times 10^{-12}$
C_2	$1.513\,61 \times 10^{-2}$	$6.419\,18 \times 10^{-3}$	$3.412\,67 \times 10^{-3}$	$5.857\,78 \times 10^{-3}$
C_3	$7.518\,86 \times 10^{-2}$	$-2.028\,96 \times 10^{-3}$	$1.991\,67 \times 10^{-3}$	$7.682\,22 \times 10^{-3}$
C_4	$4.606\,43 \times 10^{-3}$	$-1.910\,80 \times 10^{-5}$	0	0
C_5	$1.350\,00 \times 10^{-2}$	$1.357\,76 \times 10^{-4}$	$1.050\,60 \times 10^{-5}$	$-2.964\,00 \times 10^{-6}$
C_6	$-1.067\,50 \times 10^{-4}$	0	0	0
C_7	$1.366\,00 \times 10^{-5}$	0	0	0
T_i range (keV)	$0.2 - 100$	$0.5 - 190$	$0.2 - 100$	$0.2 - 100$
$(\Delta \langle \sigma v \rangle)_{\max}$ (%)	0.25	2.5	0.35	0.3

$$\theta = T / \left[1 - \frac{T\left(C_2 + T\left(C_4 + TC_6\right)\right)}{1 + T\left(C_3 + T\left(C_5 + TC_7\right)\right)} \right] \tag{2.13}$$

$$\xi = \left(\frac{B_G^2}{4\theta} \right)^{1/3} \tag{2.14}$$

All fusion reactions were assumed to be D-T fusion events and S_i was assumed to be entirely from the 1 MeV neutral deuterium beams [9]. For each power source and sink in the equations, it was assumed that half of the power applied to the ion species (which was being simulated) and half to the electrons (which were not explicitly being simulated). This approximation was made for simplicity and is effectively equivalent to ignoring the temperature equilibration time between the ions and electrons.

The density and temperature of this system were simulated for one second for instantaneous temperature increases (occurring at time t=0) of 10%, 20%, and 30% relative to the steady-state solution. The density decreased by about 2% over the course of each simulation. The absolute and relative temperature histories, as well the Q value and the amount

of fusion α heating are shown in Figure 2.4. It is observed that significant increases in the α-heating source can be achieved in less than a second, given a large enough initial increase in the core temperature.

A second simulation was run to determine how quickly the beams would need to be shut off in order to reverse the temperature excursion. It was found that turning off the beam power within 800 ms was sufficient to turn around a power excursion resulting from a 30% temperature change, while a more minor temperature change of 10% afforded a longer interval of 3100 ms. Based on the assumptions in this model, the failure to turn off the auxiliary power within those time limits would result in continued temperature increases even if the beams were subsequently shut down. More drastic corrective actions would then become necessary.

It should be noted that these simulations used the IPB98(y,2) scaling law for the global energy confinement time given below without any confinement enhancement factors [9]. The confinement performance of current experiments is often compared against what would be predicted by the IPB98(y,2) scaling law using a factor $H_{98} = \tau_E/\tau_E^{98}$. Experiments now routinely exceed H_{98}=1, so it is reasonable to expect ITER to operate with high confinement times as well. Although higher confinement times can be beneficial from the perspective of power output, they could also make power excursions occur on even faster timescales.

$$\tau_E^{98} = 0.0562 I^{0.93} B^{0.15} P^{-0.69} n^{0.41} M^{0.19} R^{1.97} \epsilon^{0.58} \kappa_a^{0.78} \tag{2.15}$$

2.7 Passive and Active Control Mechanisms

Of particular interest to this thesis research are physics mechanisms that could rapidly decrease particle or energy confinement in response to an increase in temperature without action having to be taken by the control system and without significantly increasing the risk of a disruption. These "passive" control mechanisms can be thought of as being analogous to fuel-bowing, Doppler broadening, and other negative feedback mechanisms found

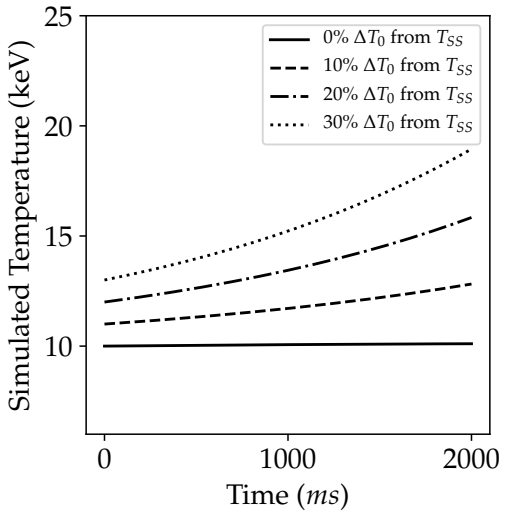

(a) Ion and Electron Temperature

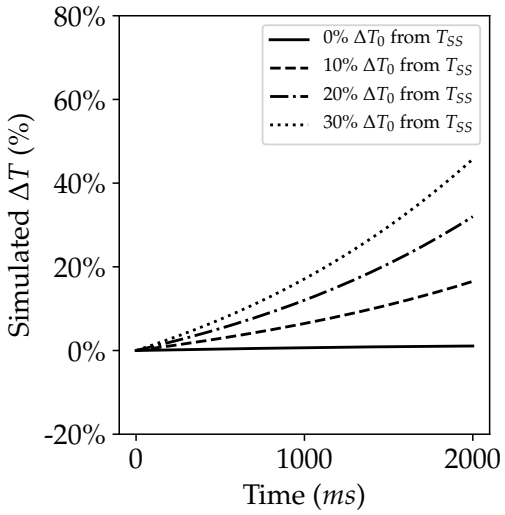

(b) Relative change in temperature

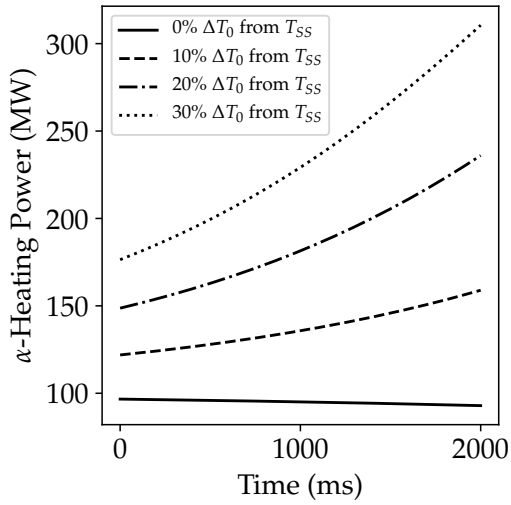

(c) α-heating

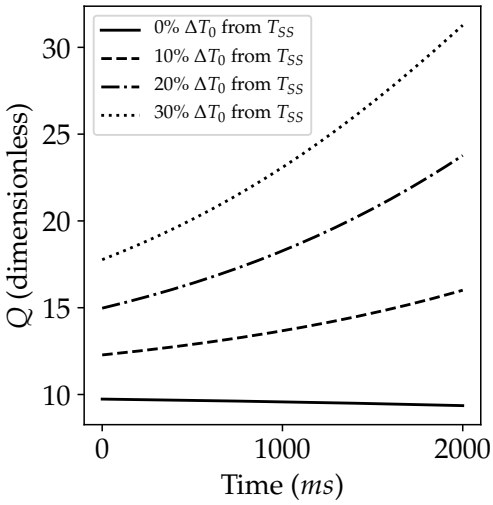

(d) Q

Figure 2.4: Simulated temperature (a), relative change in temperature (b), α-heating power (c), and Q as functions of time for several power excursion simulations (d). T_{ss} denotes the steady-state initial temperature.

in fission reactors, in which a temperature increase affects a reduction in reactor power without the need for any active control actions. Active mechanisms are those that require deliberate control of the various actuators in a tokamak by control algorithms in response to diagnostic signals.

Several physics mechanisms that could potentially offset a thermal power excursion were identified over the course of this project. These mechanisms include direct ion orbit loss (IOL), Multi-faceted Asymmetric Radiation From the Edge (MARFEs), Edge Localized Modes (ELMs), electron cyclotron (EC) radiation from the core plasma, impurity radiation from the core and edge plasma, divertor power balance effects [23], stabilized 3/2 neoclassical tearing modes, and several others. The most promising were then selected for more detailed investigation. The following chapters describe the physics of promising mechanisms, outline approaches for evaluating their viability, report the results of those calculations, and draw conclusions.

2.8 Thesis Objectives

Having summarized the history of burn control research and provided the motivation for this research, the objectives of this thesis can be summarized as follows:

1. Identify and quantify possible passive mechanisms that could limit incipient fusion power excursions in tokamaks.

2. Improve our understanding of the physical mechanisms involved in both active and passive control measures.

3. Improve our understanding of the timescales involved in power excursions and the subsequent energy transport processes that remove energy from the inner core.

CHAPTER 3

CYCLOTRON RADIATION AS A NEGATIVE FEEDBACK MECHANISM

Significant power losses in tokamak reactors result from several important radiative phenomena. Broadly speaking, these radiative loss mechanisms can be divided into radiation resulting from the interaction of electrons with magnetic fields, and those resulting from the interaction of electrons with ions. Cyclotron radiation, the focus of this chapter, results from the centrifugal acceleration of charged particles as they spiral about magnetic field lines. Other sources of radiative power losses and their implications for thermal power excursions will be explored in Chapter 4.

3.1 Cyclotron Radiation Overview

Charged particles in a magnetic field execute a circular orbit with a radius $r_L = v_\perp / |\Omega|$. Here $v_\perp$ is the perpendicular component of the particle's velocity and $\Omega = -eB/m$, where e the charge of the particle, B is the strength of the magnetic field, and m is the particle's mass. The centrifugal acceleration of the particle as it executes its gyro-orbit results in radiation, which is usually referred to as cyclotron radiation. It is occasionally referred to as synchrotron radiation because the radiation was first observed in synchrotron devices, [24] however "cyclotron" appears to be the more commonly used term in the scientific literature.

The amount of power radiated through cyclotron radiation by a single particle can be calculated [8] as

$$\frac{dW_{\mathrm{rad}}}{dt} = \frac{e^2}{6\pi\epsilon_0 c^3} \frac{r_L^2 \Omega^4}{\left[1 - \left(\frac{r_L \Omega}{e}\right)^2\right]^2} \tag{3.1}$$

The magnitude of dW_{rad}/dt is shown for several relevant species over a range of ITER-

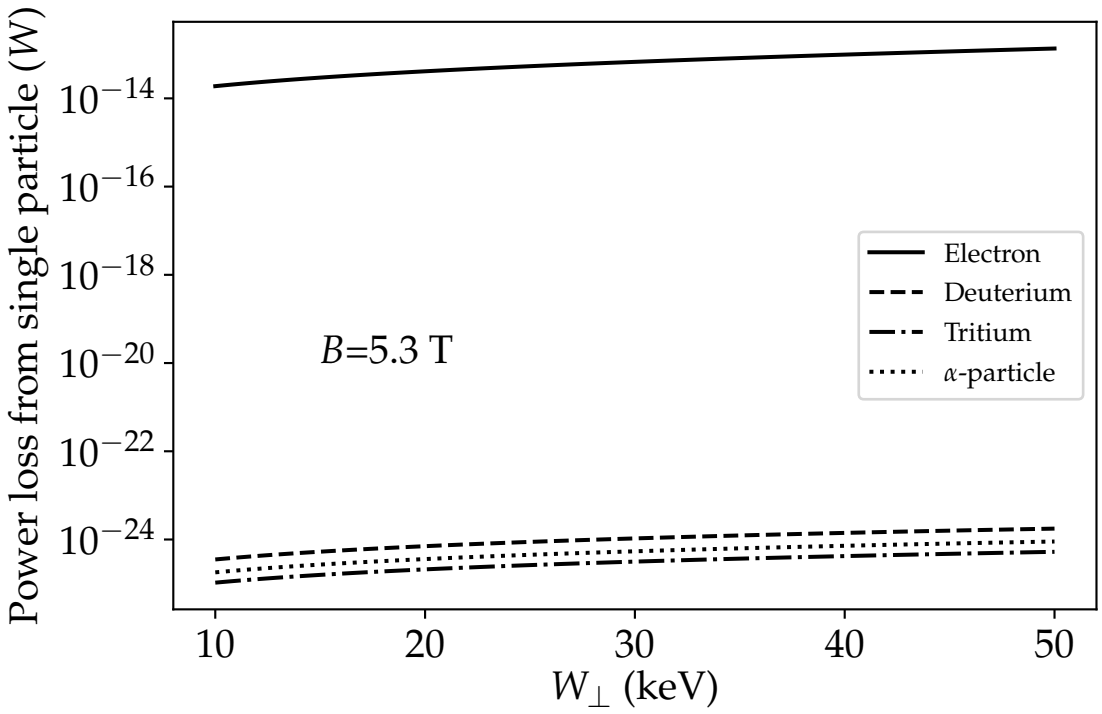

Figure 3.1: The power loss per particle from cyclotron radiation as a function of temperature for several species. For plasma densities of $\sim 1 \times 10^{20}$, EC would radiate $\sim$1-10 MW/m^3, some of which would be reabsorbed in the plasma.

relevant temperatures in Figure 3.1.

Figure 3.1 clearly shows that electron cyclotron (EC) radiation far exceeds the cyclotron radiation of other species. Simple calculations reveal that EC radiation is capable of producing several MW of radiated power per cubic meter in an ITER-like tokamak, while the other species combined would barely produce a watt. Consequently, this analysis will focus on EC radiation.

3.2 EC Power Losses in ITER

Section 2.3 described the conventional thinking that almost all of the energy given to the electrons is subsequently collisionally distributed locally between the electrons and ions as they attempt to come into equilibrium. The presence of a significant amount of EC radiation forces us to reevaluate that picture. It is critically important to recognize that any

fusion power given to electrons by α-particles during a power excursion and then lost from the electrons through EC radiation is not available to locally heat ions. Rather, some of the fusion α heating of the electrons is immediately lost from the central core as EC energy, which is deposited elsewhere in the plasma or surrounding wall. In essence, we can rewrite the total effective fusion power source in a volume V as

$$P_{\mathrm{fus,eff}} = \int_V \frac{1}{4} n_i^2 \left\langle \sigma v \right\rangle_{\mathrm{fus}} dV + \int_V P_{\mathrm{EC}} dV \tag{3.2}$$

where $P_{\mathrm{EC}} < 0$ is the power loss density from electron cyclotron radiation. It is this amount, $P_{\mathrm{fus,eff}}$, that then gets distributed to the electrons and ions in the central core plasma.

To assess the effectiveness of EC radiation in mitigating power excursions, we must quantify the timescale on which it operates, the total amount of power that can be radiated, and how the amount of radiated power changes with temperature.

There are two timescales of interest for EC radiation. The first is the loss of power from the inner core to the wall or other plasma regions, which occurs on a short enough timescale that it can be regarded as instantaneous. The second involves the energy that is radiated from the inner core, deposited in other regions of the plasma, and subsequently dissipated through other mechanisms [18, 19, 25].

The calculation of EC power loss is quite complex and requires the use of computationally expensive 3D transport solvers that account for the energies and frequencies of the radiation, the probability of being absorbed in the plasma, and the probability of reflecting off the wall, among other things. Fortunately, a fit has been developed [26] based on many EC simulations. In this fit, the total power loss $P_{EC,\mathrm{tot}}$ from EC (already integrated over

volume) can be calculated from

$$P_{EC,\mathrm{tot}}\,(MW) = 3.84\times10^{-8}\,(1-r)^{1/2}\,Ra^{1.38}\kappa^{0.79} \times B_t^{2.62} n_{e_0(20)}^{0.38} T_{e_0}\,(16+T_{e_0})^{2.61} \times \left(1+0.12\frac{T_{e_0}}{p_{a_0}^{0.41}}\right)^{-1.51} K\,(\alpha_n,\alpha_T,\beta_T)\,G\,(A) \quad (3.3)$$

Here, r is the wall reflectivity for radiation in the EC frequency range, which is not well-known, but is estimated to be in the range of 0.8 - 0.9. R, a, κ, and B_t are the tokamak's major radius, minor radius, elongation, and toroidal magnetic field strength, respectively. $n_{e_0(20)}$ is the core electron density divide by 1×10^{20} and T_{e_0} is the core electron temperature in units of keV. The p_{a_0} coefficient is calculated as

$$p_{a_0} = 6.04\times10^{3}\frac{a n_{e_0(20)}}{B_t} \quad (3.4)$$

K, given in Equation 3.5, is a function of the shape of the radial density and temperature profiles, which are parameterized as shown below.

$$K\,(\alpha_n,\alpha_T,\beta_T) = (\alpha_n+3.87\alpha_T+1.46)^{-0.79} \times (1.98+\alpha_T)^{1.36}\,\beta_T^{2.14}\left(\beta_T^{1.53}+1.87\alpha_T-0.16\right)^{-1.33} \quad (3.5)$$

$$n_e\,(\rho) = n_{e_0}\left(1-\rho^2\right)^{\alpha_n} \quad (3.6)$$

$$T_e\,(\rho) = (T_{e_0}-T_{e_a})\left(1-\rho^{\beta_T}\right)^{\alpha_T}+T_{e_a} \quad (3.7)$$

The total EC power loss in ITER was calculated using Equation 3.3 for a range of values of the core temperature, T_{e_0}. The temperature at the seperatrix, T_{e_a}, was held constant,

Table 3.1: ITER parameters used to calculate EC power losses.

R_0	6.2 m	T_{e_0}	10-60 keV
a	2.0 m	T_{e_a}	1 keV
κ	1.7	α_T	8.0
B_T	5.3 T	β_T	5.0
n_{e_0}	1.4×10^{20} m^{-3}	r	0.8
α_n	0.5		

* T_i is assumed to be equal to T_e for these calculations unless otherwise specified. Example density and temperature profiles are shown in Figure 3.3. Example parameters from several non-inductive reference scenarios for ITER given in the ITER Technical Basis [27] are shown in Appendix A for reference.

as the analysis is primarily concerned with temperature increases in the core. Other parameters were characteristic of ITER and are shown in Table 3.1. The resulting total EC power loss as a function of core temperature is plotted in Figure 3.2a. The chart shows that the total power loss from EC is significant and increases faster than linearly with increasing core temperature, especially at higher temperatures.

3.3 The Effects of EC Radiation in a Power Excursion

To quantify the effect of EC on the fusion power gain, we must first calculate the total fusion power based on the density and temperature profile parameterizations in Equations 3.6 and 3.7. The fusion power density as a function of minor radius (dP_α/dV) was calculated as shown in Equation 3.8 for the same range of T_{e_0} as the P_{EC} calculation above. The total fusion power to the plasma per unit volume is given by Equation 3.8 with U_α = 3.5 MeV, and includes the energy given to both the ions, U_α^i, and to the electrons U_α^e.

$$\frac{dP_\alpha}{dV} = \frac{1}{4} n_i^2(\rho) \left[\langle \sigma v \rangle_f (T_i(\rho)) \right] U_\alpha \tag{3.8}$$

The total fusion power was obtained by multiplying dP_α/dV by the differential volume as a function of minor radius dV/dr, which was approximated by $dV/d\rho = 4\pi^2 \kappa R_0 a^2 \rho$.

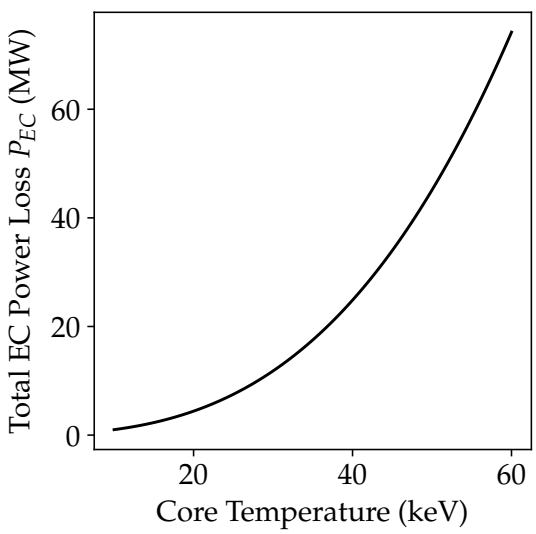

(a) The total amount of EC radiated power as a function of core electron temperature T_{e_0} resulting from Equation 3.3.

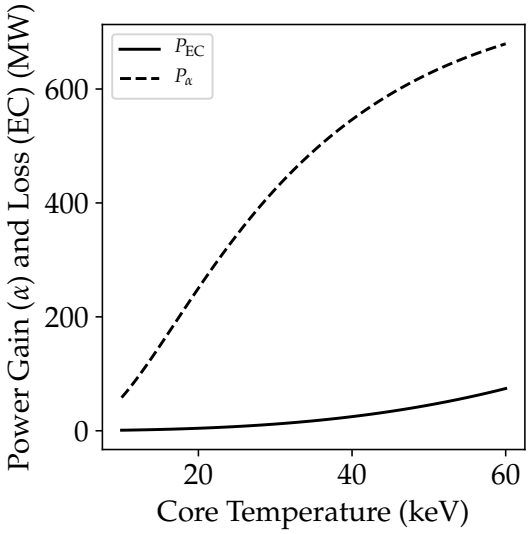

(b) The plot in (a) compared with the total fusion power as a function of core temperature

Figure 3.2: The total amount of EC radiated power in ITER as a function of core temperature, compared with the total amount of fusion α heating for reference.

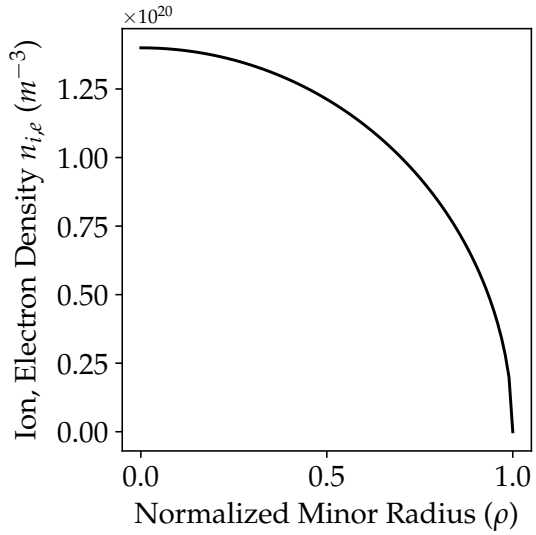

(a) Density

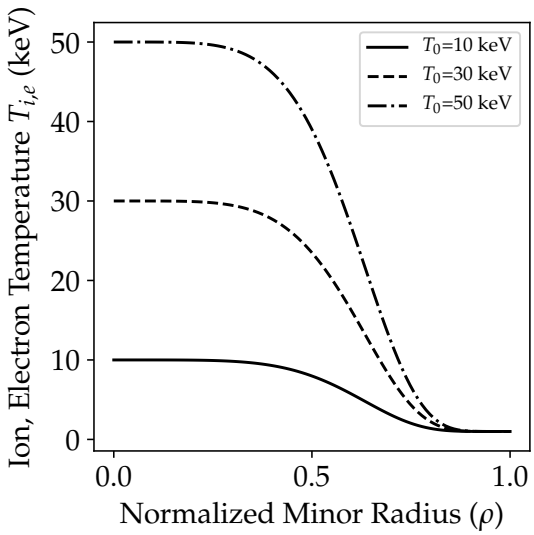

(b) Temperature

Figure 3.3: Density and temperature radial profiles that are representative of an ITER discharge and synthesized using the model in Equations 3.6 and 3.7.

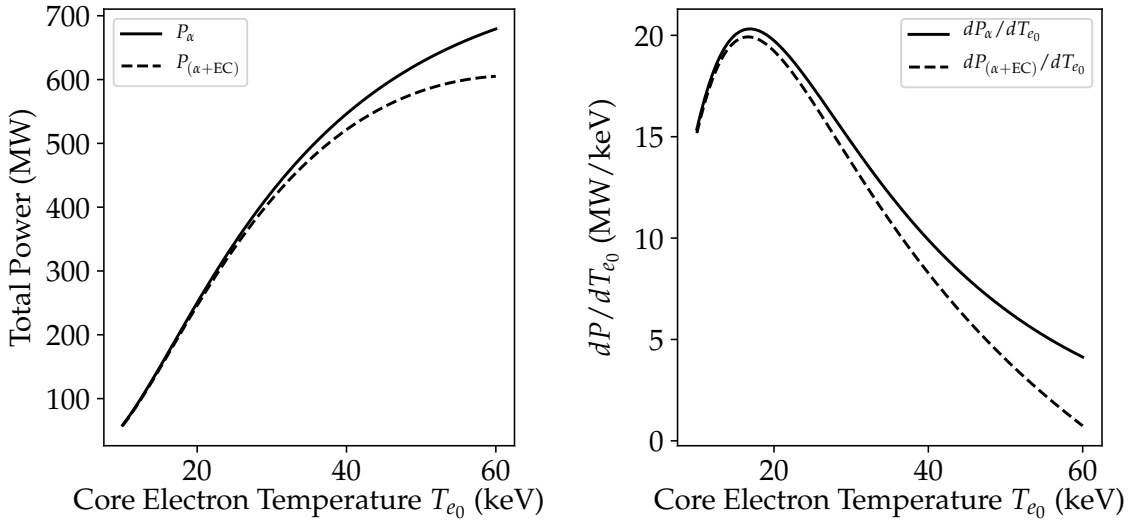

(a) Total α heating power in ITER with and without EC losses as a function of core temperature.

(b) The derivatives of the plots in (a) with respect to core temperature.

Figure 3.4: Total fusion α heating power in ITER and its temperature derivative both with and without EC radiation.

The resulting function, $dP_\alpha/d\rho$ was then integrated over minor radius to obtain $P_\alpha\left(T_{e_0}\right)$ for a range of core temperatures. The effects of EC were included by calculating $P_{(\alpha+\mathrm{EC})}$ as shown below

$$P_{(\alpha+\mathrm{EC})}\left(T_{e_0}\right) = \int_V P_\alpha\left(T_{e_0}\right) + P_{\mathrm{EC}}\left(T_{e_0}\right) dV \tag{3.9}$$

The calculated EC losses are compared with the fusion power P_α in Figure 3.4a. The derivative of these functions with respect to core temperature, dP/dT_{e_0} is shown in Figure 3.4b.

It is ultimately the energy that is given to the ions in the plasma core that is of interest for burn control purposes. If we assume that the power that is not lost through EC radiation is distributed approximately evenly between the electrons and the ions (either through direct α heating of the ions or through subsequent collisional heating of the ions by the electrons), then we can calculate the total power to the ions and its temperature derivative. These quantities are shown in Figure 3.5

From these plots, it can be seen that EC power loss has a significant effect on effective

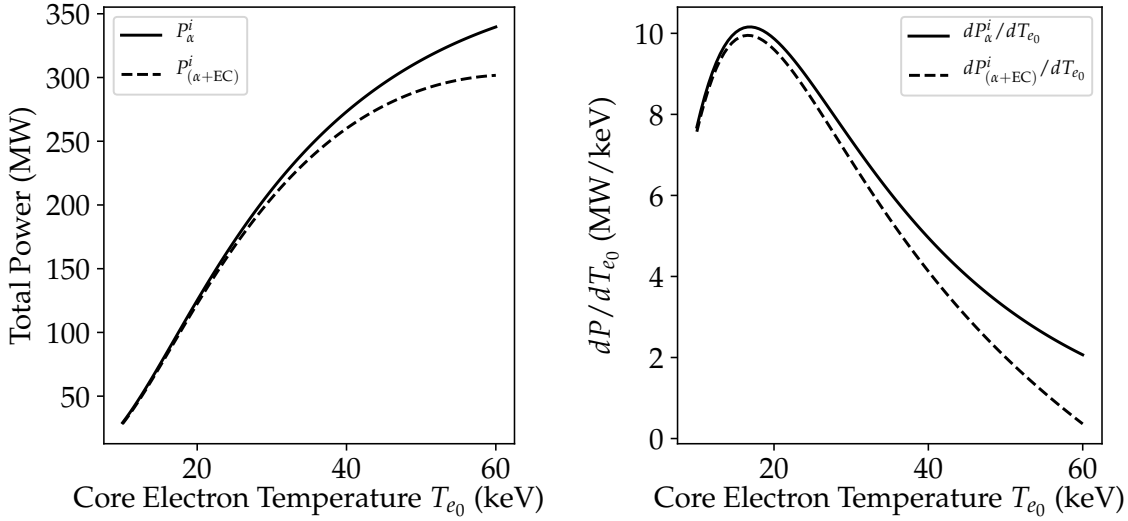

(a) Total α heating given to the ions with and without EC assuming that power that is not lost to EC radiation is divided equally between electrons and ions.

(b) The derivatives of the plots in (a) with respect to core temperature.

Figure 3.5: ITER fusion α heating power given to the ions and its temperature derivative both with and without EC radiation.

α-heating power of the plasma and its temperature derivative, especially for core temperatures greater than 30-40 keV. Although EC losses aren't enough to guarantee thermal stability ($dP/dT_{e_0} \leq 0$) for the range of core temperatures predicted in ITER, they enable greater thermal stability than would be predicted without their inclusion in the model.

3.4 Correcting the Core EC Power Loss for Intra-Plasma EC Transport

The frequency of EC radiation is in the 100 GHz frequency range. At those frequencies, electrons in the plasma are not totally transparent to the EC radiation. (Were this not the case, electron cyclotron resonance heating (ECRH) would not be possible.) The first researchers to describe this intra-plasma EC radiation transport were Trubnikov [28], and Drummond and Rosenbluth [29]. Their work was built on by Tamor [18] and, more recently, by Albajar *et al.* who investigated intra-plasma EC radiation transport in ITER using the RAYTEC code. [25, 19, 30] One notable result is a calculation of the net cooling

of the inner core in ITER, as well as the net heating power in the outer core and edge.

The partial opacity of the outer core and edge plasma regions to EC radiation raises the possibility that EC radiation transport within the plasma could have a measurable effect on the power balance in the inner core. In effect, EC radiation is an instantaneous "transport" mechanism for electron energy from the core to the edge plasma and wall. This matters for burn control because the power absorbed in the outer core is, in fact, lost from the inner core even though it is not accounted for in Equation 3.3. By estimating the amount of power that is reabsorbed in the outer core and edge, we can estimate the extent to which Equation 3.3 understates the effect of EC in the inner core. For this analysis, we will use a calculated volumetric radiative loss profile for ITER given in Reference [25]. This profile is reproduced in Figure 3.6.

To calculate the total power generated in the inner core and the total net power absorbed in the outer core and edge, we first obtain the total (as opposed to volumetric) power loss profile by multiplying the dP_{EC}/dV profile in Figure 3.6 by $dV/d\rho$, as described previously. The resulting total power loss profile $dP_{\mathrm{loss,EC}}/d\rho$ is shown in Figure 3.7.

A root-finder was used to identify the radial location at which the profile changes from a net power loss to a net gain as ρ = 0.626. Integrating from ρ = 0 to ρ = 0.626, and then from ρ = 0.626 to ρ = 1, reveals that for this EC transport calculation, there is a net loss of $\sim$41.5 MW from the inner core and a net power gain of $\sim$3.1 MW in the outer core. The remaining power, approximately 38.4 MW, is lost from the system, presumably to the first wall. This occurs over the course of many reflections off of the wall and subsequent paths through the plasma, with energy being deposited to the wall with each reflecton and to the plasma each time it passes through it. Figures 3.6 and 3.7 take this into account and represent the net effect, as calculated by the RAYTEC code. This 38.4 MW loss from the system would correspond to what would be calculated by Equation 3.3. This means that the amount of EC power lost from the inner core, which is what is of the most interest for burn control, is approximately 8% (41.5 / 38.4 $\sim$ 1.08) greater than what we would calculate

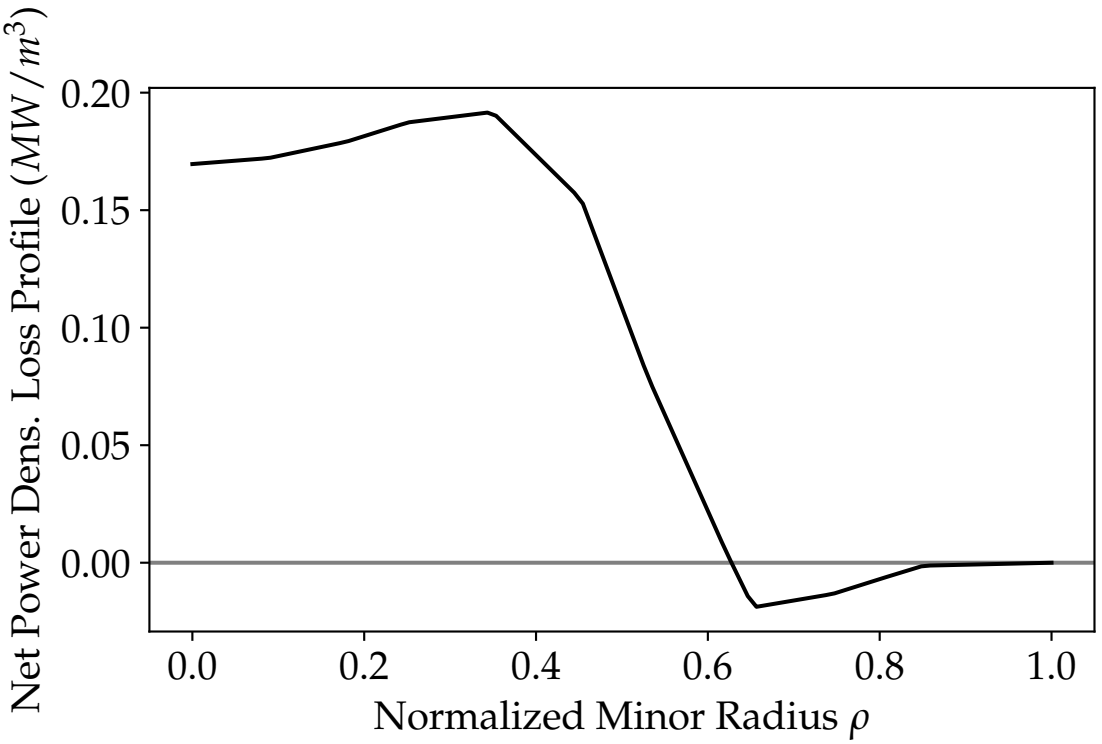

Figure 3.6: Volumetric power loss from EC radiation as a function of ρ. This chart, which was taken from the literature [25], shows a significant power density loss from the plasma electrons inside of $\rho \sim 0.6$ from EC radiation and an increase in power density for $\rho \gtrsim 0.6$ from that EC radiation being redeposited. Here, the power loss is being shown as a positive number, which must be subtracted from the total α power produced to obtain the net α heating power.

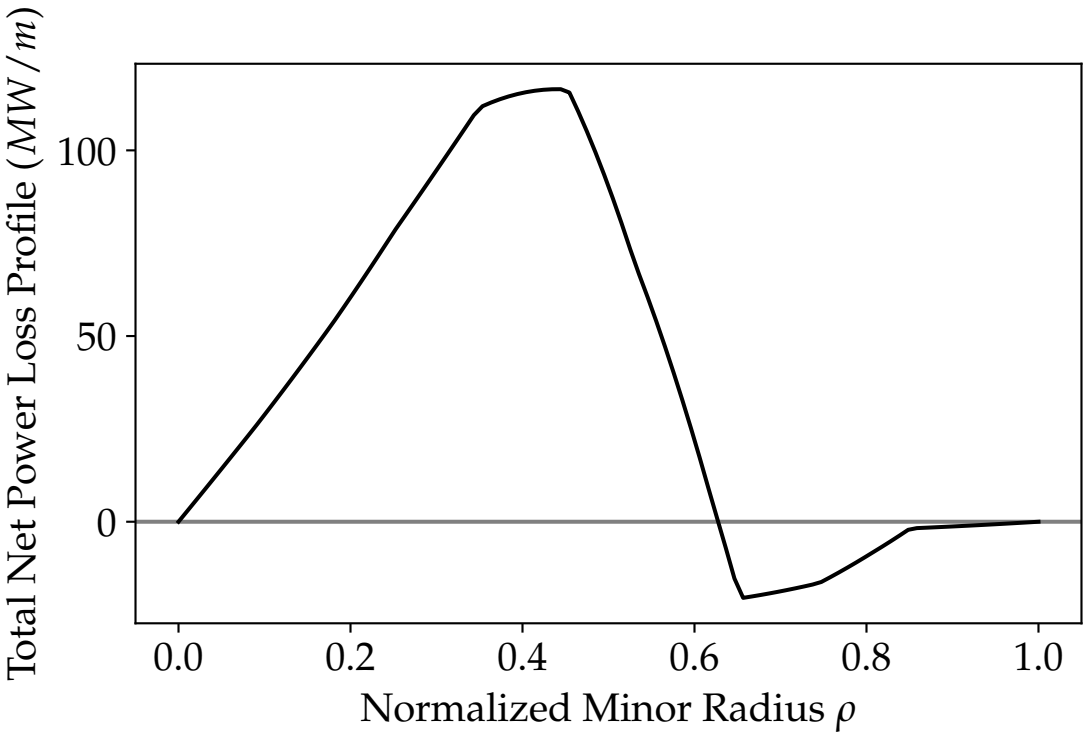

Figure 3.7: Total EC Power loss from ITER as a function of normalized minor radius ($dP_{EC}/d\rho$). For this simulation, $\sim$41 MW was lost from the region inside ρ = 0.626 and $\sim$3 MW was absorbed outside of that region.

from Equation 3.3. Further analyses using RAYTEC or another EC radiation transport code could be used to confirm this estimate.

As shown by the plots in Figure 3.8, this "correction" to the EC losses obtained by Equation 3.3 has a small but noticeable effect on the extent to which EC reduces the temperature dependence of the fusion heating power. The next section will explore ways in which this phenomenon could be used to enhance EC losses and further reduce the temperature dependence of the fusion heating power.

3.5 Opportunities for EC Power Loss Enhancement

Much of the power in the central core that leaves the core is later reabsorbed in the inner core because A) that is the location where the EC radiation is most likely to encounter a resonance and B) because of the higher electron densities in the central core. For burn control, it is desirable to reduce the amount of EC radiation that can return to the inner core by depositing it in the first wall or in the outer regions of the plasma. There are two ways that power radiated from the inner core can be prevented from returning to the inner core and being reabsorbed:

1. By reducing the reflectivity of the wall at EC frequencies, since much of the EC power generated in the inner core is reabsorbed in the inner core after reflecting off the wall. It is, after all, the net power loss (rather than the absolute power loss) from the inner core that is useful for burn control.

2. By increasing the ability of the outer core and edge plasmas to absorb EC radiation generated in the inner core. Although this may create other heat removal problems, any power absorbed in the outer core or edge regions is no longer available to be absorbed in the inner core.

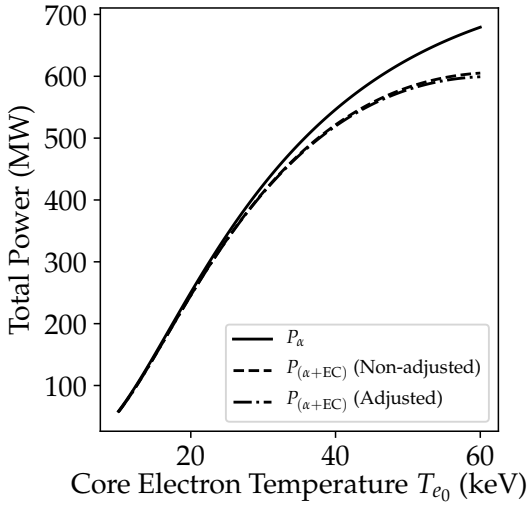

(a) Total fusion power including the effect EC power losses

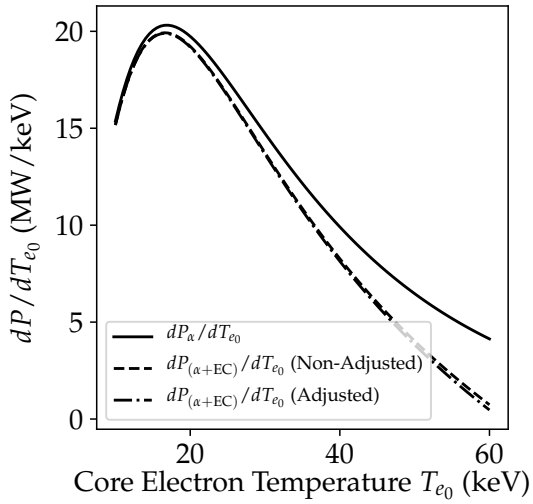

(b) Temperature derivative of the plots in (a)

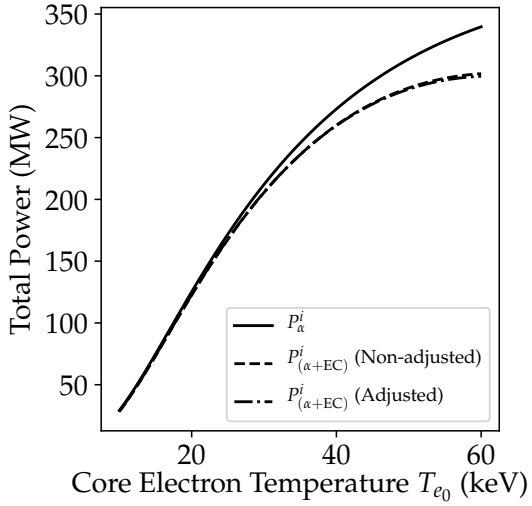

(c) Total fusion power to the ions including the effect of EC power losses

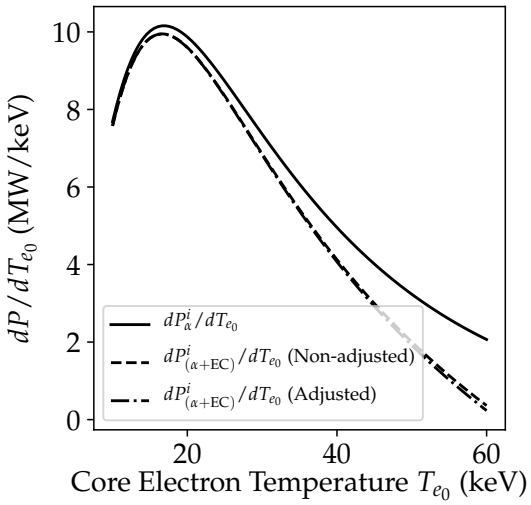

(d) Temperature derivative of the plots in (c)

Figure 3.8: Comparison of the effects of EC losses from the inner core before (non-adjusted) and after (adjusted) accounting for power reabsorbed in the outer core and edge, which is not included in Equation 3.3. The adjustment results in a small but noticeable increase in radiative losses that increases with increasing temperature.

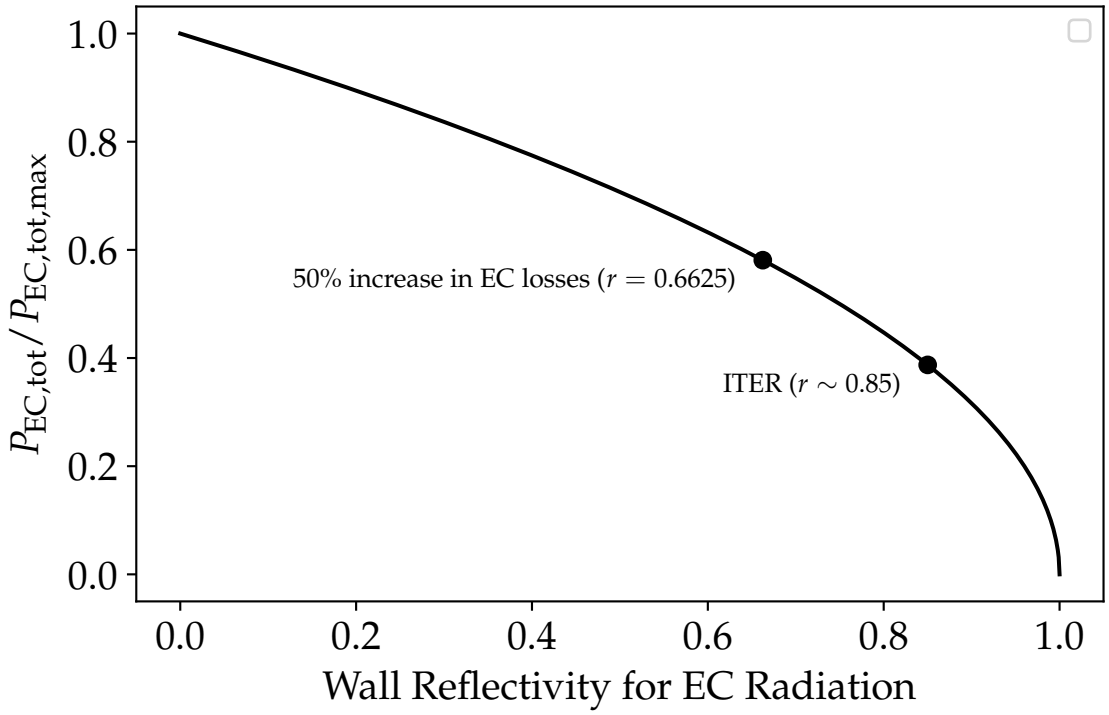

Figure 3.9: The effect of changes in wall EC reflectivity on total EC losses. A $\sim$22% reduction in wall reflectivity relative to what is estimated for ITER would result in a 50% increase in EC losses, which could enhance thermal stability in the event of a power excursion.

3.5.1 Modifying Wall Reflectivity to Enhance EC Losses

According to Equation 3.3, the total losses from EC radiation in an ITER-like plasma scale as $\sqrt{1-r}$, where r is the reflectivity of the wall panels. Obviously, if the walls were totally reflective at EC frequencies, the losses would approach zero. Similarly, the losses would reach a maximum for a highly absorbing first wall. The dependence of total EC losses on wall reflectivity is illustrated in Figure 3.9.

The relative decrease in wall reflectivity needed to achieve a desired increase in EC losses, y, can be calculated from

$$\Delta r = r_{\text{new}} - r_{\text{old}} = (1 - r_{\text{old}})\left(1 - y^2\right) \tag{3.10}$$

As illustrated in Figure 3.9, a 50% increase in EC power losses could be achieved by reduc-

ing the EC reflectivity of the wall tiles by $\sim$22%. Evaluating the feasibility of modifying the EC reflectivity of ITER's first wall is beyond the scope of this thesis, however it is interesting to note that EC radiative losses could conceivably be significantly enhanced by modifying the reflective characteristics of the first wall through materials research.

3.5.2 Modifying EC Absorption in the Outer Plasma to Increase Effective EC Losses

EC transport within a plasma is a complicated function of wave frequency, plasma density and temperature, the direction of propagation, and the local magnetic field strength along the direction of propagation [18, 25, 19, 30]. The most important dynamic, however, is that EC radiation emitted with a frequency Ω_c interacts most strongly wherever $\Omega = n\Omega_c$, where n in an integer. As discussed previously, these resonances are functions of the magnetic field strength B for a given species with charge e and mass m. In tokamaks, the toroidal magnetic field strength varies approximately as 1/R. For the reference ITER parameters used in this analysis (B_0 = 5.3 T, R_0 = 6.2 m, a = 2.0 m), the toroidal magnetic field varies from about 7.8 T at the inboard mid-plane to about 4.0 T at the outboard mid-plane, as illustrated in Figure 3.10.

Clearly, resonances at n=1 are most likely to occur along the vertical plane that includes the magnetic axis (for EC emitted very near the magnetic axis). It seems likely that without any other modifications to the magnetic environment, that the inner core and the plasma regions directly above and below it would absorb the most EC energy, although EC transport analyses would need to be conducted to confirm this.

It is conceivable that by modifying the magnetic field strength in the vicinities of the inboard and outboard mid-planes, the EC energy absorption in those regions could be increased. Additionally, increasing the electron density in regions characterized by greater EC absorption could also increase EC absorption. Unfortunately, the practicality and quantification of these effects must be left for future work due to the need for complex EC transport codes.

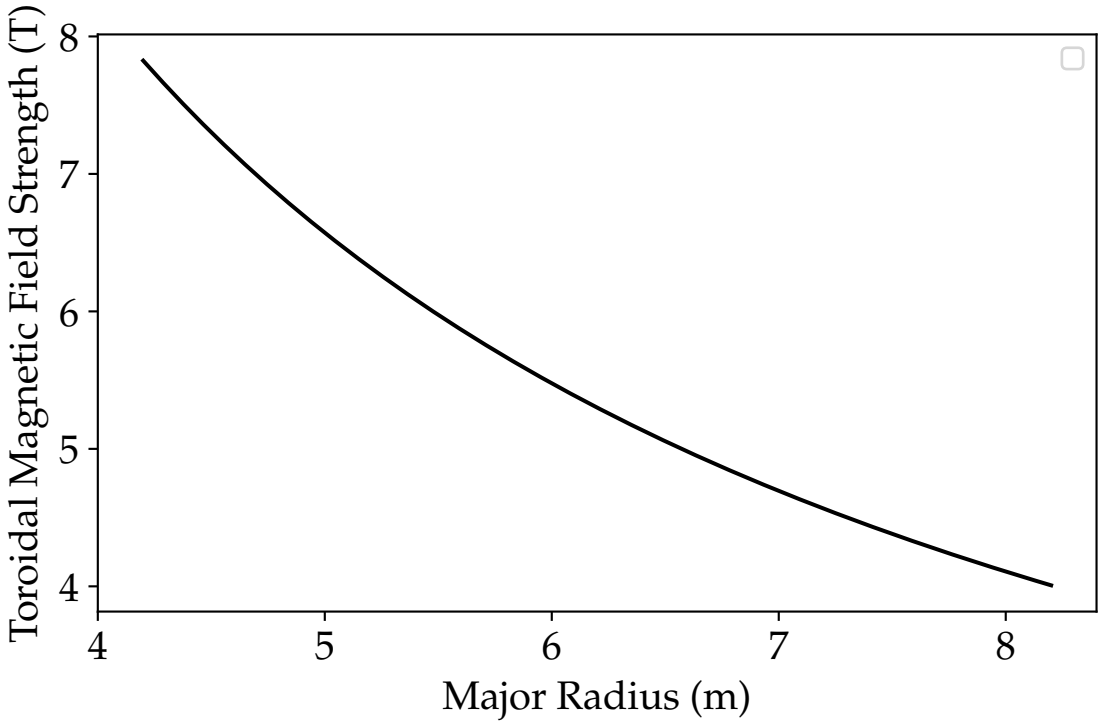

Figure 3.10: The toroidal magnetic field strength in ITER going from the inboard mid-plane to the outboard mid-plane

3.6 EC Radiation Conclusions

Although EC radiation is not particularly important in currently operating tokamaks, it is likely to be a significant source of energy transfer and loss in ITER. Furthermore, the partial opacity of the plasma to EC radiation generated in the inner core could have significant effects on the radial temperature profile.

Its strong temperature dependence combined with the fact that it results in a nearly instantaneous power loss allow EC radiation to act as a significant negative feedback mechanism in the event of a power excursion. The preceding calculations indicate that EC power loss provides a loss of as much as 2 MW/keV, and is especially pronounced for temperatures $\gtrsim$ 40 keV.

The effectiveness of EC radiation as a negative feedback mechanism could conceivably be enhanced by reducing the reflectivity of the first wall or by increasing EC absorption in the outer core and edge, since any power transmitted to and absorbed in the outer core is no longer available to be reabsorbed in the inner core. This latter goal could be achieved by increasing the electron density in regions of EC resonance or by increasing the volume of the plasma where electrons would experience an EC resonance with EC radiation produced in the inner core.

It should also be noted that EC radiation during a power excursion has implications for the first wall heat removal system. Although EC radiation is emitted perpendicular to the field line and uniformly in poloidal direction [8, 31], it may not be deposited uniformly on the first wall due to the partial opacity of the plasma and the shorter distance that radiation would have to travel to escape at the inboard and outboard mid-planes. The effects of both the increase in heat to the first wall, as well as any effects from the non-uniformity could be an important subject for future research.

CHAPTER 4
THE EFFECTS OF IMPURITY RADIATION

In addition to the EC radiation discussed in the previous chapter, significant power losses in tokamak reactors result from the interactions of electrons with ions, especially impurity ions. Brehmsstrahlung (German for "braking") radiation results from the acceleration that electrons experience as they collide with ions. The radiation resulting from the capture of energetic electrons into empty impurity orbital electron states followed by a radiative loss of electron energy is known as recombination radiation. Lastly, the excitation of impurity orbital electrons followed by radiative transition back into the ground state is known as line radiation.

For any of these radiative processes to be useful in mitigating a power excursion, the radiative losses must increase in response to the excursion. There are two ways in which this can occur:

1. An “intrinsic” increase in radiation due to a positive electron temperature dependence of radiative power losses for impurity ions already in the plasma

2. A “controlled” increase in radiation due to increased impurity content, such as pellet injection, gas injection, or by actively changing impurity transport characteristics.

Various fits have been developed to estimate total radiative losses from a tokamak. Bremsstrahlung radiation can be estimated as [8]

$$P_{\mathrm{brem}}\left(W/m^3\right) \simeq 1.7 \times 10^{-38} z^2 n_i n_e T_e^{1/2} \tag{4.1}$$

where T_e is in units of keV and all others are MKS. Similar fits for line and recombination

radiation are given in Equations 4.2 and 4.3, respectively.

$$P_{\text{line}}\left(MW/m^3\right) \simeq 1.8 \times 10^{-44} \frac{z^4 n_e n_z}{T_e^{1/2}} \tag{4.2}$$

$$P_{\text{rec}}\left(MW/m^3\right) \simeq 4.1 \times 10^{-46} \frac{z^6 n_e n_z}{T_e^{3/2}} \tag{4.3}$$

In all of these fits, densities are in units of m^{-3} and temperatures are in units of keV.

Another fit [8] that attempts to capture all impurity-related radiative losses (including bremsstrahlung, line, and recombination) is

$$P_{\text{imp}}\left(MW/m^3\right) \simeq (1 + 0.3T_e) \times 10^{-43} n_e n_z z^{(3.7 - 0.33 \ln T_e)} \tag{4.4}$$

Here, again, T_e is in units of keV and other variables are in MKS units.

Bremsstrahlung radiation, like EC, increases monotonically with increasing temperature [8] and is therefore a potential negative feedback mechanism. The temperature dependence of recombination and line radiation is much more complex.

The purpose of this chapter is to explore these radiative loss mechanisms and evaluate the extent to which they can be used to offset thermal power excursions.

4.1 Calculating the Impurity Emissivity Function

The radiation losses from a plasma can be represented as

$$P_{\text{rad}} = \sum_k n_k n_e L_{z,k}\left(T_e\right) \tag{4.5}$$

where n_k is the density of the impurity species, n_e is the electron density, and L_z is the impurity radiation emissivity function. The temperature dependence of L_z is the result of a great deal of atomic physics and depends on the impurity ion species, the relative

mix of charge states, the local electron temperature, and even the local neutral density. For intrinsic impurity radiation to be useful as a feedback mechanism, L_z must have a significantly positive temperature derivative at the temperature of interest.

When calculating the $L_z(T_e)$ function for an impurity species, it is common to assume that the various charge states of an impurity ion come into a "coronal equilibrium," which assumes that time scales for atomic processes are short compared to other time scales of interest and that spatial gradients are not significant [8]. With those assumptions, we can write a coupled set of "coronal equilibrium" equations for the densities of impurity ions of the various charge states $z > 0$.

$$n_e \left(I_{z-1} n_{z-1} + R_{z+1} n_{z+1} - I_z n_z - R_z n_z \right) = 0 \tag{4.6}$$

Here, I_z and R_z are the ionization and recombination rate coefficients. These coefficients can be obtained either from various fits or, preferably, from a reliable atomic physics database. For this work, these coefficients were obtained from the venerable ADPAK routines developed by Russell Hulse [32]. The ADPAK routines have the added benefit of computing bremsstrahlung, recombination, and line radiation coefficients, as well as the effects of neutral hydrogen at the same time. The presence of neutrals increases the likelihood of charge exchange and partial recombination events, both of which can significantly increase radiative losses relative to an environment in which there are fewer neutral particles [8].

After the relative abundances of the various impurity charge states have been determined as functions of temperature, the impurity radiation emissivity function L_z can be determined as a function of electron temperature T_e and neutral fraction $nf = n_n/n_e$. The L_z function for several tokamak-relevant impurity species is shown in Figure 4.1.

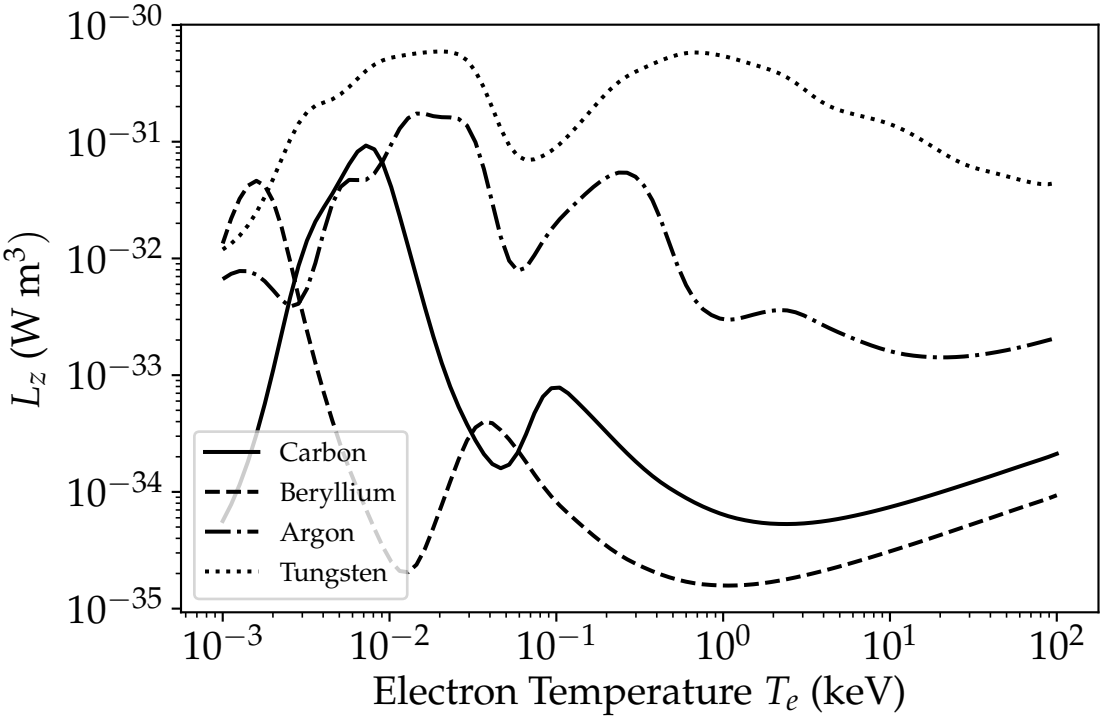

Figure 4.1: L_z as a function of temperature for several tokamak-relevant species (nf=0), as calculated from ADPAK data using the GT3 code, which is discussed in greater detail in Appendix B.

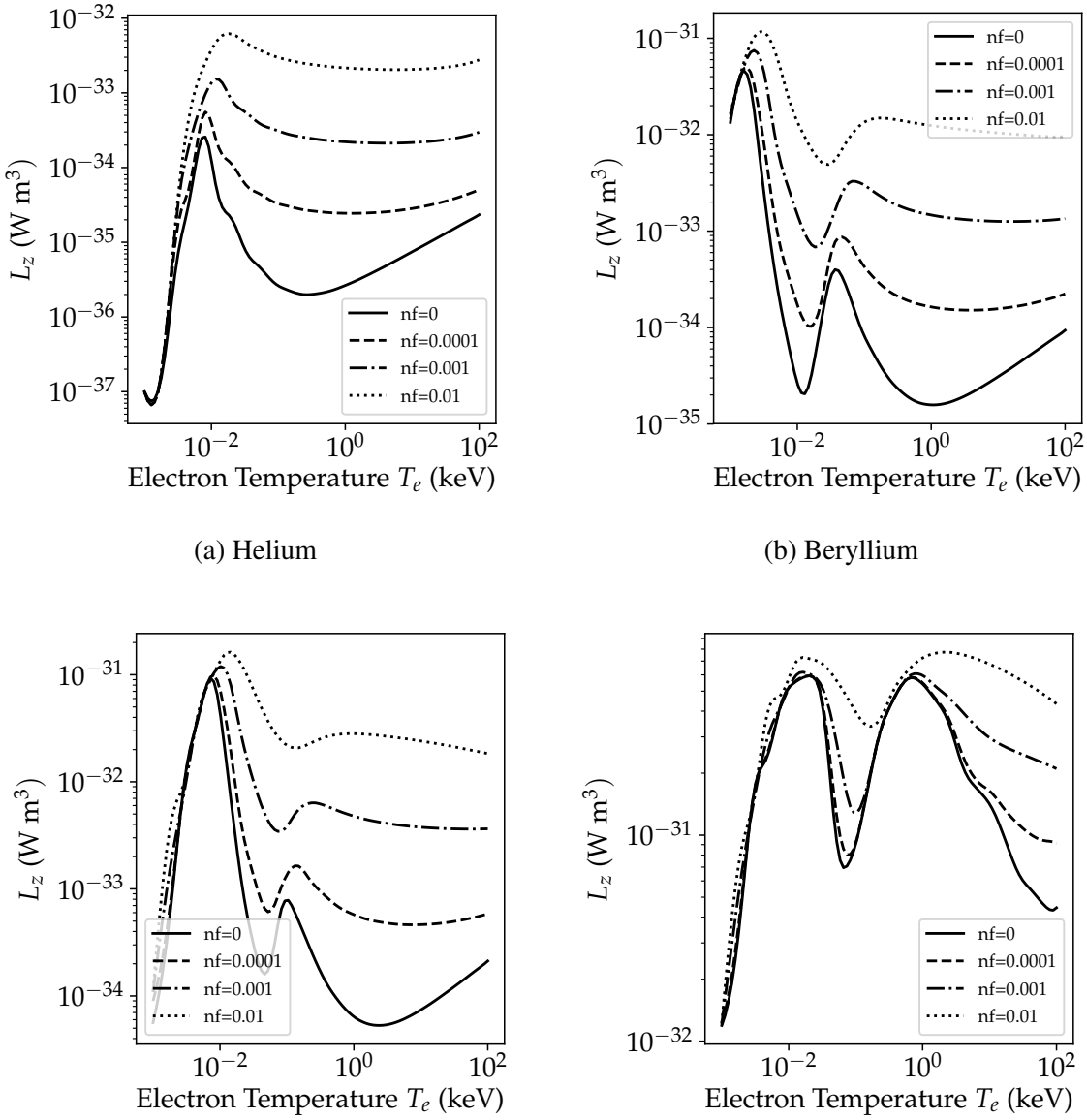

(a) Helium

(b) Beryllium

(c) Carbon

(d) Tungsten

Figure 4.2: The impurity radiation emissivity (L_z) as a function of temperature and neutral fraction for several tokamak-relevant species. These were calculated from ADPAK data using the GT3 code.

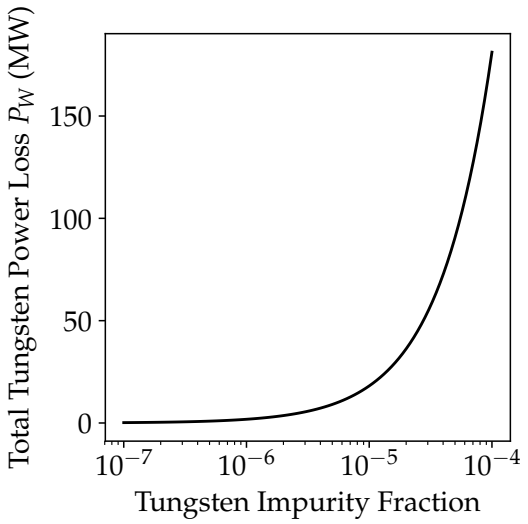

(a) Total power losses in ITER from Tungsten as a function of impurity fraction

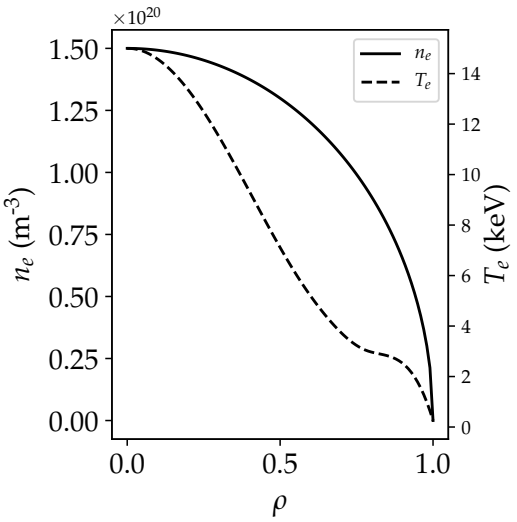

(b) Density and temperature profiles used in the calculation of the plots in (a).

Figure 4.3: Total power losses in ITER from Tungsten as a function of impurity fraction and the density and temperature profiles used to calculate them. These were calculated using ADPAK data and the GT3 tokamak analytics code described in Appendix B. Uniform impurity fractions were assumed.

4.2 Passive Impurity Radiation in the Core

One of the most significant challenges facing ITER is the accumulation of tungsten in the core of the reactor. Because tungsten (z=74) is not fully ionized even at the temperatures expected in ITER's inner core, concentrations as low as $\sim 10^{-5}$ could radiate enough power out of the plasma to pose problems for the power balance. Modeling the transport of impurities in tokamaks has been an area of active research for several decades [33], and preliminary simulations [34, 35, 36] suggest that it will be possible to keep the tungsten concentration below 10^{-5}. To meaningfully contribute to that overall research effort is beyond the scope of this thesis, however Figure 4.3a shows the total amount of radiation that can be expected from tungsten for the reference problem for a range of tungsten impurity fractions. These were calculated using ADPAK and zero neutrals fraction.

Figure 4.4a suggests that, all else being equal, we can expect tungsten radiation to decrease somewhat with increasing temperature for 1 keV $\lesssim T_e \lesssim$ 100 keV. This is detri-

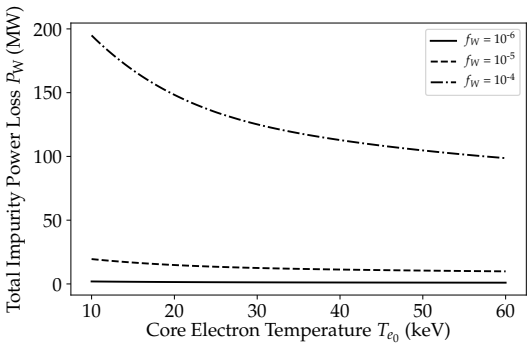

(a) Tungsten

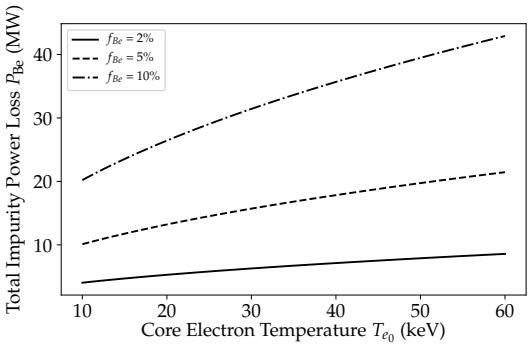

(b) Beryllium

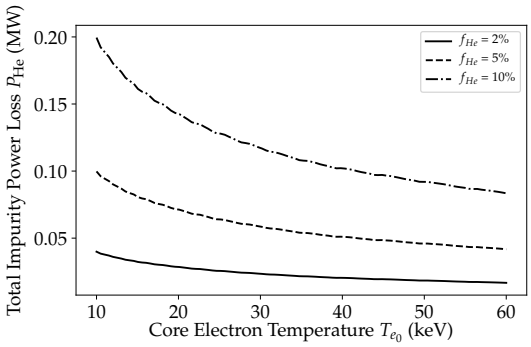

(c) Helium

Figure 4.4: Total power loss from for ITER-relevant species as functions of core temperature for several impurity fractions calculated using ADPAK data and the GT3 code. Due to the need to vary the core temperature, these were obtained using the density and temperature profile parameterizations described in Chapter 3

.

mental to the goal of thermal stability, although potentially beneficial from the perspective of attaining high power. To quantify this, the total radiated power from tungsten was evaluated for a range of core temperatures, as was done in previous sections. Because of the uncertainty in the tungsten impurity fraction, the analysis was repeated for impurity fractions 10^{-6}, 10^{-5}, and 10^{-4}, and the results are shown in Figure 4.4a. The results of similar calculations for beryllium and helium (i.e. fusion α-particles) are also shown in Figure 4.4. Impurity fractions of 2%, 5%, and 10% were modeled for beryllium and helium, based on the range of values predicted in the literature [36, 37, 38].

These results also suggest that while tungsten and beryllium impurity radiation are both

clearly relevant for the power balance, radiation from α-particles is not. These results also agree with the general consensus [39, 40] that tungsten concentrations in the core higher than $\sim 10^{-5}$ radiate far more power than can be tolerated in a steady-state discharge.

4.2.1 Implications Intrinsic Impurities for Passive Burn Control

As expected from Figure 4.1, tungsten impurity radiation decreases with increasing temperature, though not strongly in the higher temperature range for tungsten concentrations of $\lesssim 10^{-5}$. Radiation from beryllium increases with increasing temperature, also as expected. To better quantify the extent to which tungsten, beryllium, and helium would exacerbate or offset an incipient power excursion, the derivatives of these functions with respect to the core temperature were calculated for the same impurity concentrations.

It can be seen from Figure 4.5 that positive contribution to dP/dT from tungsten, especially at lower temperatures, will more than offset any helpful negative contributions from Beryllium and Helium at low temperatures.

The effects of radiation from intrinsic impurities on fusion power are compared with the effects of EC in Figure 4.6. The derivatives of those plots are shown in Figure 4.7. It is clear from Figure 4.7 that increased radiation from intrinsic impurities in response to a temperature increase will do very little to passively offset the increase in fusion rate during a temperature excursion, especially at higher temperatures.

4.3 Actively Controlled Core Impurity Radiation

ITER will be equipped with shattered pellet injection (SPI) systems capable of rapidly shooting frozen pellets of fuel and/or impurity species toward the plasma and shattering them just prior to their entry into the plasma chamber [9]. Experimental evidence [41] indicates that these systems will be much more effective at penetrating the core plasma than massive gas injection (MGI), which is only capable of effecting conditions in the edge region of the confined plasma. This is illustrated in Figure 4.8.

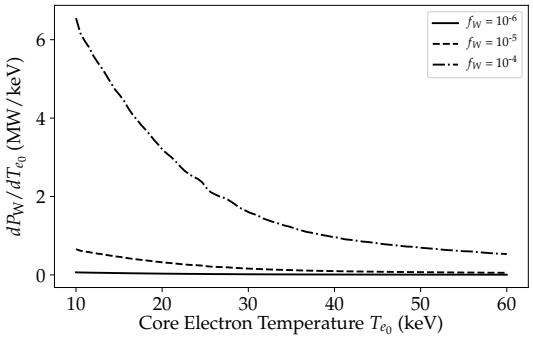

(a) Tungsten

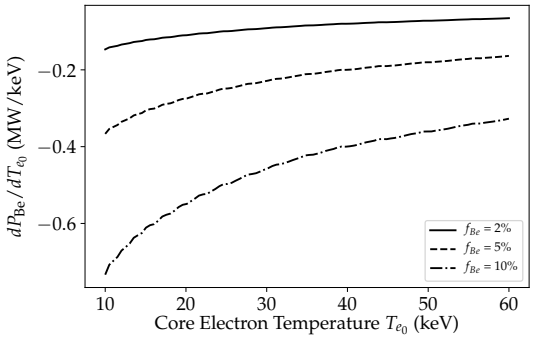

(b) Beryllium

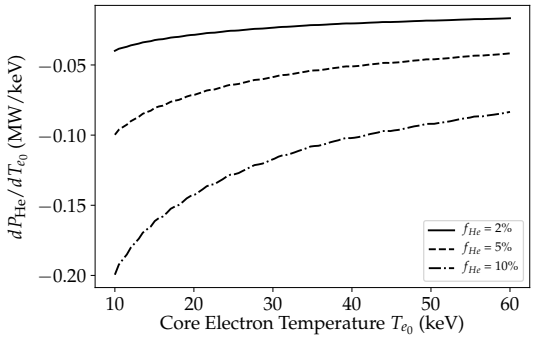

(c) Helium

Figure 4.5: Differential power loss with increasing temperature as a function of core temperature for impurity radiation from several ITER-relevant species. These are the derivatives of the plots in Figure 4.4

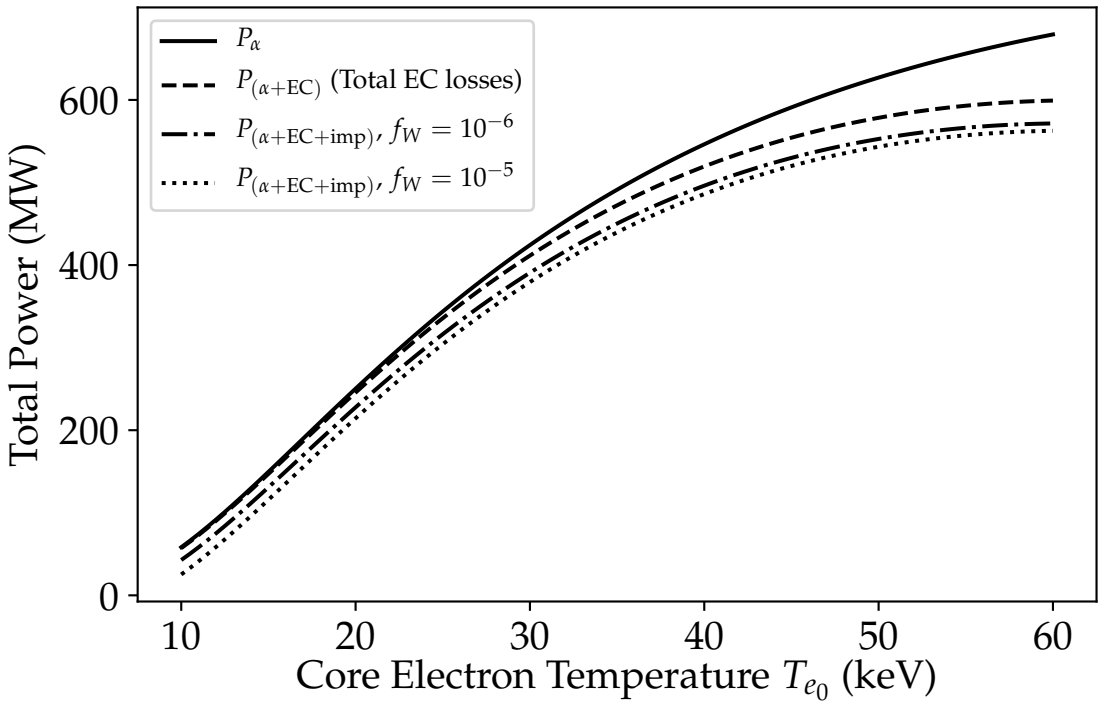

Figure 4.6: The effective fusion α heating after accounting for various radiative loss mechanisms, including tungsten impurity radiation at various impurity fractions. Calculated using the density and temperature parameterizations of Chapter 3 ADPAK data.

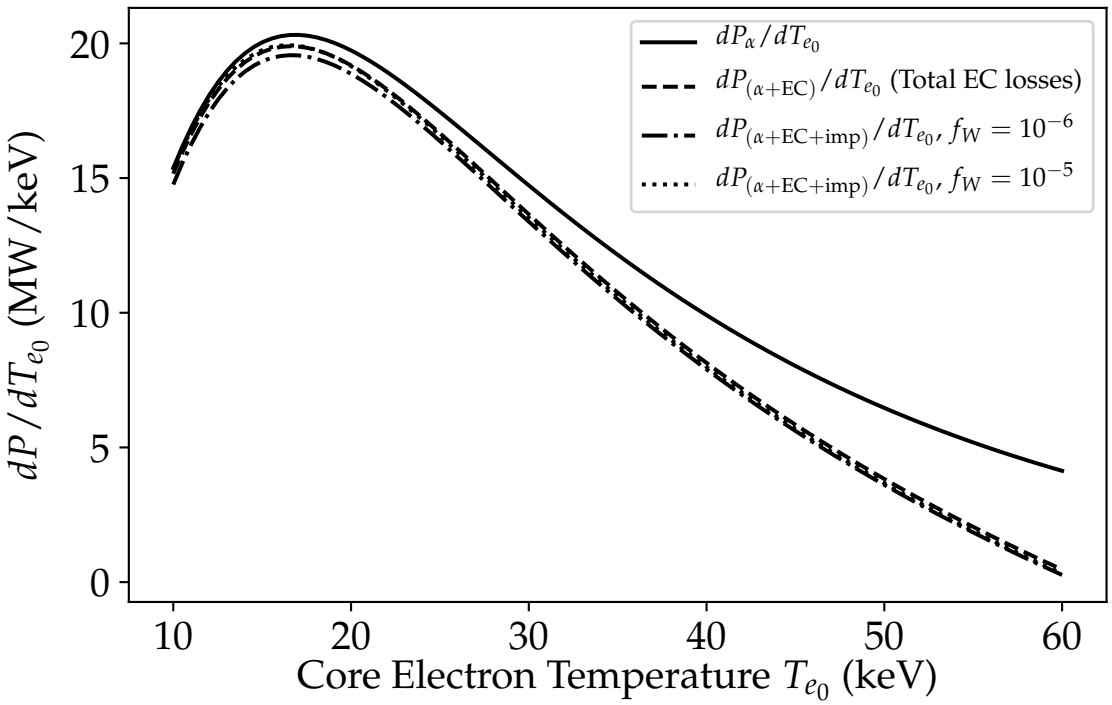

Figure 4.7: The derivatives of the plots in Figure 4.6 with respect to core temperature. Although increasing the tungsten impurity fraction has a significant effect on the effective heating power (as seen in Figure4.6, it has a much smaller effect on the way in which that power source changes with temperature.

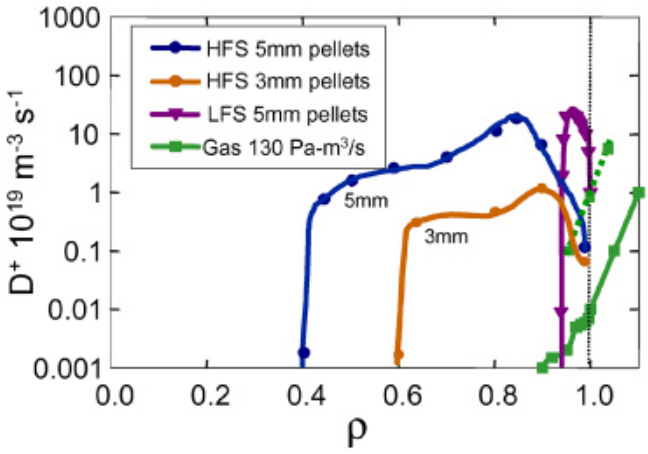

Figure 4.8: Comparison of pellet fuelling and gas fuelling source profiles for ITER. The dashed gas curve is calculated from the SOLPS code in actual ITER geometry. The solid gas curve is from a B2-Eirene slab calculation. Reproduced from Reference [42]

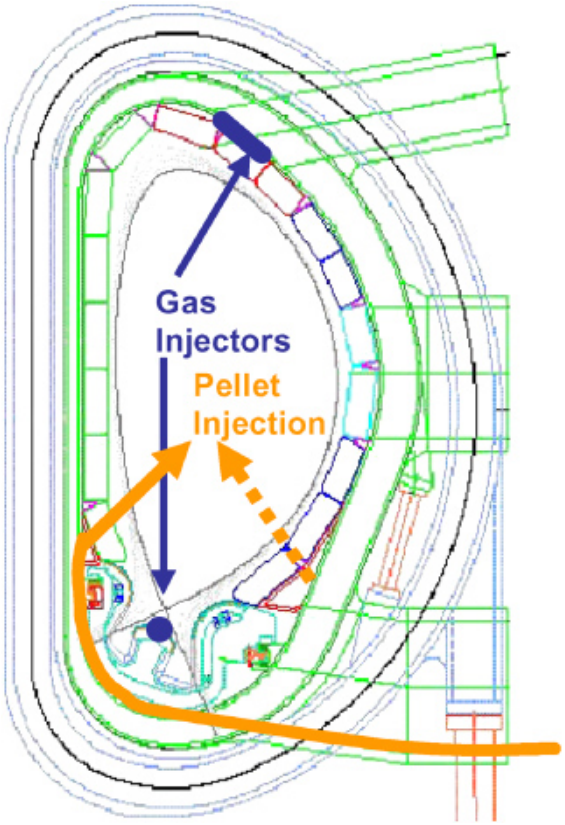

Figure 4.9: Cross section of ITER showing the pellet injection and gas injection locations. The dashed pellet trajectory is the proposed low field side location for Edge Localized Mode (ELM) triggering. Figure reproduced from Reference [42].

The pellet injection systems, which are diagrammed in Figure 4.9, are primarily intended to be used for two primary purposes: core fueling and disruption mitigation. Fueling pellets are composed of an approximately equal mix of deuterium and tritium. "Killer" pellets, such as would be used in disruption avoidance and mitigation, include a significant fraction of impurity elements that are designed to radiate as much energy out of the plasma as possible, as quickly as possible, without damaging reactor components.

It is conceivable that a third category of pellets could be developed to help maintain the desired fusion α power in the event of a thermal power excursion. These pellets would be designed to increase radiative losses or decrease the fusion rate, potentially without quenching the plasma. They would likely consist of a mix of hydrogenic species, helium, and trace amounts of noble gases. Increasing the amount of deuterium in the pellet relative

to the amount of tritium may provide a way to keep the ion density at the desired level while limiting the amount of fuel available to fuse.

As was shown in Chapter 2, power excursions are likely to occur on timescales of hundreds of milliseconds, which gives ample time for the pellet injection system to respond. Among active burn control solutions, this approach may be preferable to modulating beam and other heating sources, as those sources may also be driving rotation and helping to maintain a desired current profile.

To design these pellets and simulate their ablation and transport in the plasma is beyond the scope of this thesis, however we can perform some calculations to predict which impurity species are most likely to be useful for this purpose and how much power they could radiate from the core. Figure 4.10 shows the impurity fractions (assumed constant in the plasma) for helium, neon, argon, and krypton and the amount of power that would be radiated from the plasma.

The plots in Figure 4.10 show that radiative power losses of between 10 and 100 MW can be readily achieved using argon concentrations of 10^{-3} to 10^{-2} or using neon concentrations of between 10^{-2} to 10^{-1}. Even trace amounts of krypton can radiate significant amounts of power, which may make it sub-optimal for precise tailoring of the pellet's effects on the power balance. The optimal mix of impurity species in a burn control will depend on the capabilities of the pellet creation system and the impurity transport characteristics in ITER, however this analysis suggests that precise isotopic tailoring of pellets for burn control should be possible.

4.4 Controlling Core Impurity Concentrations using Targeted EC Current Drive

An alternative way to get impurities into the core (or keep them out of the core) is to alter the transport characteristics of impurity transport for impurities already inside the plasma by modifying the current or heating profiles. It was recently observed [43] in DIII-D that the location at which auxiliary EC current drive (ECCD) is injected into the plasma can

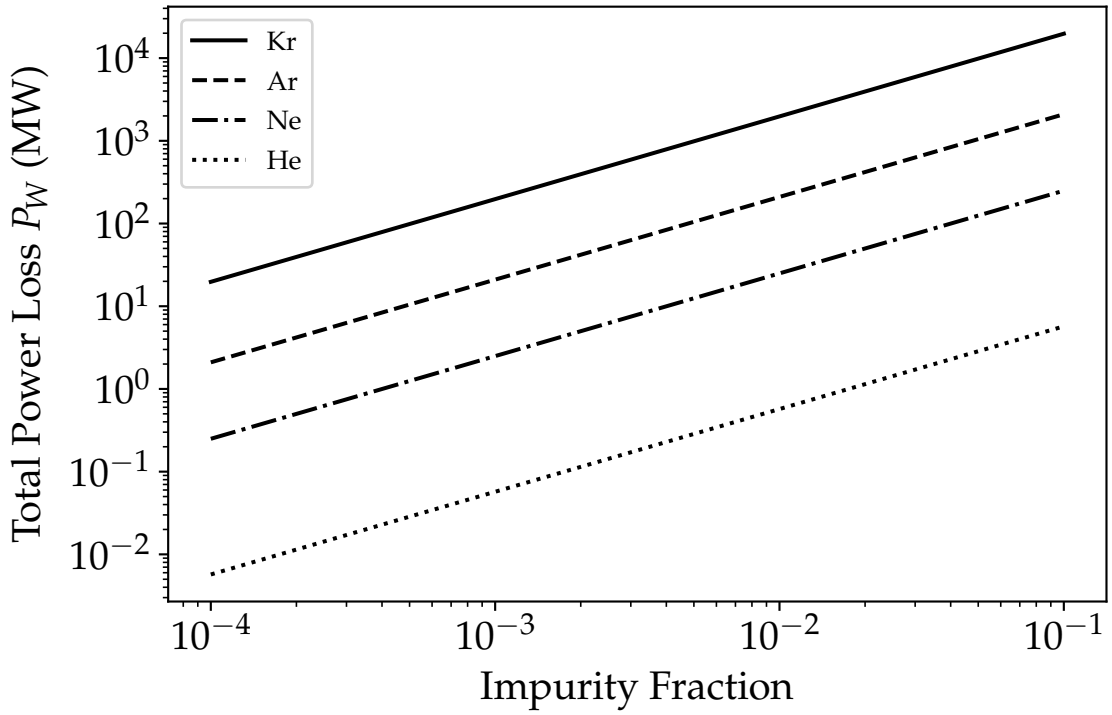

Figure 4.10: Total radiated power loss from ITER for a range of plasma impurity fractions for helium, neon, argon, krypton. These were calculated using ADPAK data and the GT3 tokamak analytics code described in Appendix B. Density and temperature profiles were the same as shown in Figure 4.3b. For simplicity, uniform impurity fractions were assumed, however it should be noted that radial impurity fraction profiles tend to be somewhat peaked in the center, especially for higher-z impurities like Tungsten.

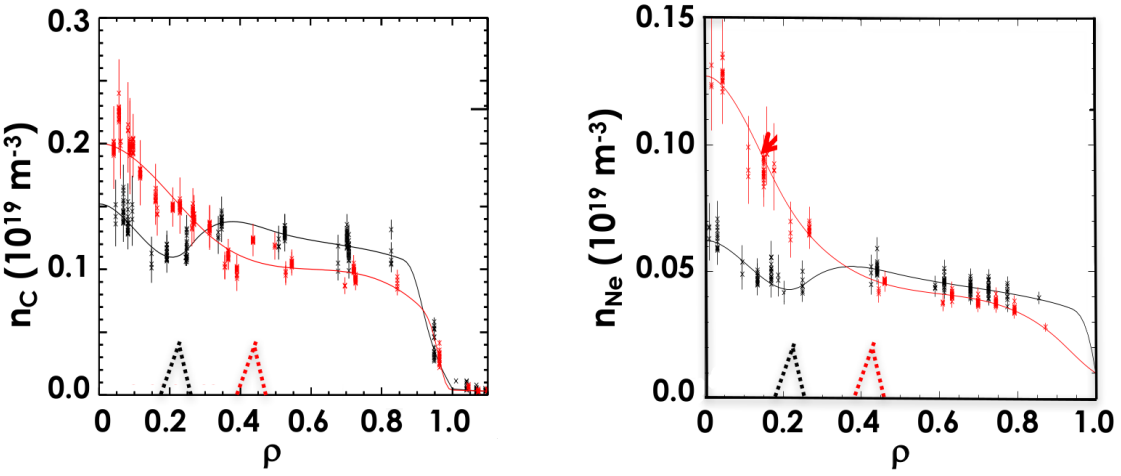

(a) Carbon

(b) Neon

Figure 4.11: Plots of radial carbon (a) and neon (b) densities in two comparable DIII-D shots with different ECCD injection locations. Injecting ECCD closer to the axis reduced impurity concentrations in the inner core. These plots are reproduced from a conference poster by Dr. Tom Petrie [43].

control the rate of impurity transport into the inner core. Similar observations have been made in other reactors, including ASDEX[44, 45]. The DIII-D results are illustrated in Figure 4.11, where carbon and neon radial density profiles are compared for shots with different ECCD injection locations.

Analysis of the DIII-D data using the STRAHL code [46] suggested that there was much stronger inward convection when ECCD was deposited farther out in the plasma. The results suggest that on-axis current drive could mitigate the concentration of tungsten and other impurities in the plasma [43]. For burn control purposes, it also suggests that reducing on-axis ECCD power could increase the flux of impurities into the core where they could radiate excess energy.

Most calculations of impurity transport in the core of ITER have focused on predicting steady-state impurity concentrations rather than modeling the dynamic evolution of radial impurity density profiles. As a result, it is difficult to predict the timescale on which changes in on-axis ECCD could increase radiative power losses in response to an incipient power excursion.

These results also suggest that on-axis ECCD could also be used to tune radiative power losses by controlling core impurity concentrations in real time. This approach could be used to prevent the onset of thermal power excursions.

4.5 Passive Impurity Feedback in the Edge

Although mechanisms effecting the power balance in the core plasma should be the focus of a burn control strategy, mechanisms that work in the edge region are also important for at least three reasons:

1. Preventing pressure increases resulting from a power excursion from reaching the q=2 surface, which could potentially lead to a disruption
2. Removing power that was deposited in the edge by EC radiation
3. Supporting the more rapid core feedback mechanisms, albeit on a slower time scale ($\sim \tau_E$)

Because of the complex temperature dependence of impurity radiation, especially at the lower temperatures that might be found in the edge plasma, it is conceivable that a steady-state distribution of noble gas impurity ions in the edge plasma could respond to an increase in T_e with increased radiative losses. Figures 4.2 and 4.12 also raise the possibility of enhancing radiative power losses by increasing the concentration of neutrals relative to the background plasma density.

Low-Z noble gases have long been investigated [8] for radiative power exhaust because they become fully ionized (and thus less radiative) at lower temperatures than those found in the core plasma. As a result, they are less likely to quench the core than higher-Z impurity atoms, such as tungsten.

The relative charge state abundances and impurity radiation emissivity functions were computed for each of the noble gases of interest and other elements of interest over temperatures ranging from $1 \times 10^{-3}\,\mathrm{keV}$ to $1 \times 10^{2}\,\mathrm{keV}$ and over values of the neutral fraction

(nf) ranging from 0 to 1×10^{-1}. Radon, being a higher-z element than even tungsten, is unlikely to be useful as a seeded impurity. Plots of $L_z(T, nf)$ are shown for Neon, Argon, Krypton, and Xenon in Figure 4.12.

Several important observations can be made from Figure 4.12: First, none of the noble gases, have a significantly positive temperature derivative in the range of temperatures that are expected to be found in the ITER edge region, i.e. $T_e \sim$ 1-5 keV [21, 47, 48, 49]. The inclusion of neutrals has the effect of further "washing out" any significant positive temperature derivatives of the L_z function for all but the lowest of temperature ranges. This suggests that impurity seeding alone is unlikely to be an effective *passive* feedback mechanism in the edge.

4.6 Active Enhancement of Impurity Radiation Losses in the Edge

Impurity radiation from the edge can be increased in three primary ways.

1. The plasma can be seeded with impurities via gas injection.

2. Radiative losses can be enhanced by increasing the neutral deuterium fraction in a region with an existing impurity population through gas puffing or deuterium pellet injection. Figure 4.12 shows that impurity radiation can be enhanced by as much as an order of magnitude by increasing the neutral fraction.

3. Impurities deposited in the core can be transported radially outward into the edge region. This process is slower than the preceding mechanisms.

To quantify the effects of deliberate impurity seeding, impurity radiation loss profiles in ITER were calculated for Neon, Argon, Krypton, and Xenon at several concentrations spanning the range of what has been predicted for ITER [48, 50, 9]. The results are shown in Figure 4.13. The total radiative losses (i.e. $\int_0^1 d\rho dP/d\rho$) for each profile are listed in the legends.

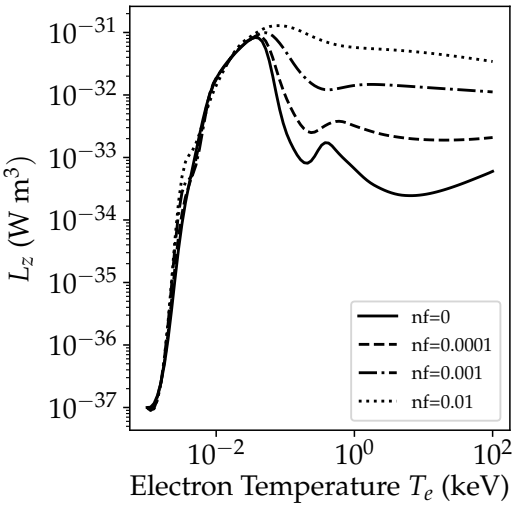

(a) Neon

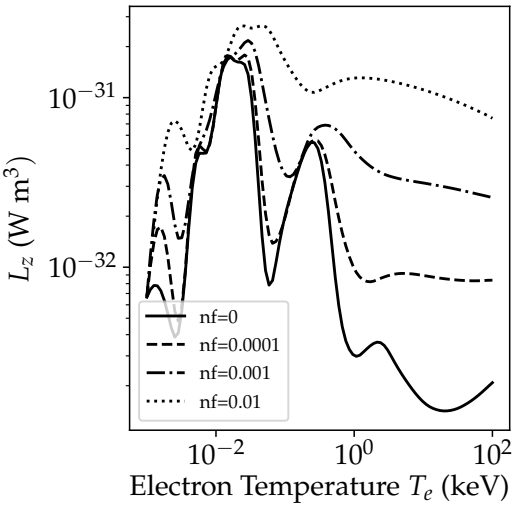

(b) Argon

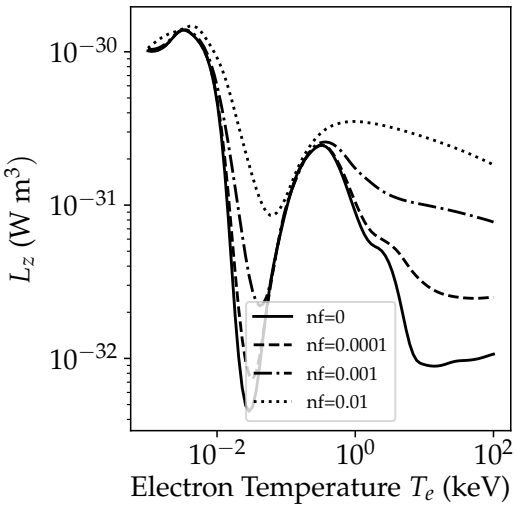

(c) Krypton

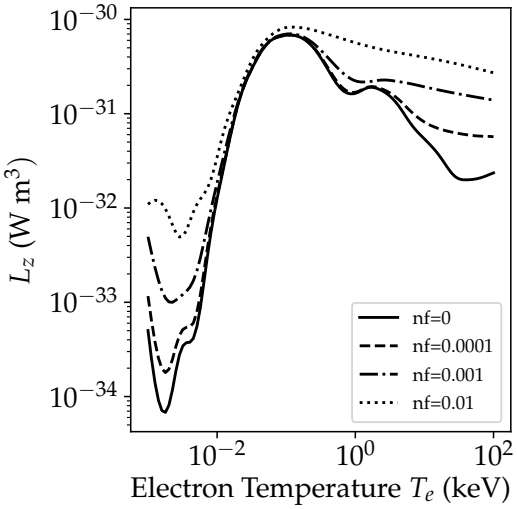

(d) Xenon

Figure 4.12: L_z as a function of temperature and neutral fraction for several noble gases, calculated using ADPAK data and the GT3 tokamak analytics code described in Appendix B. nf refers to the fraction of neutrals relative to the electron density, i.e. n_n/n_e.

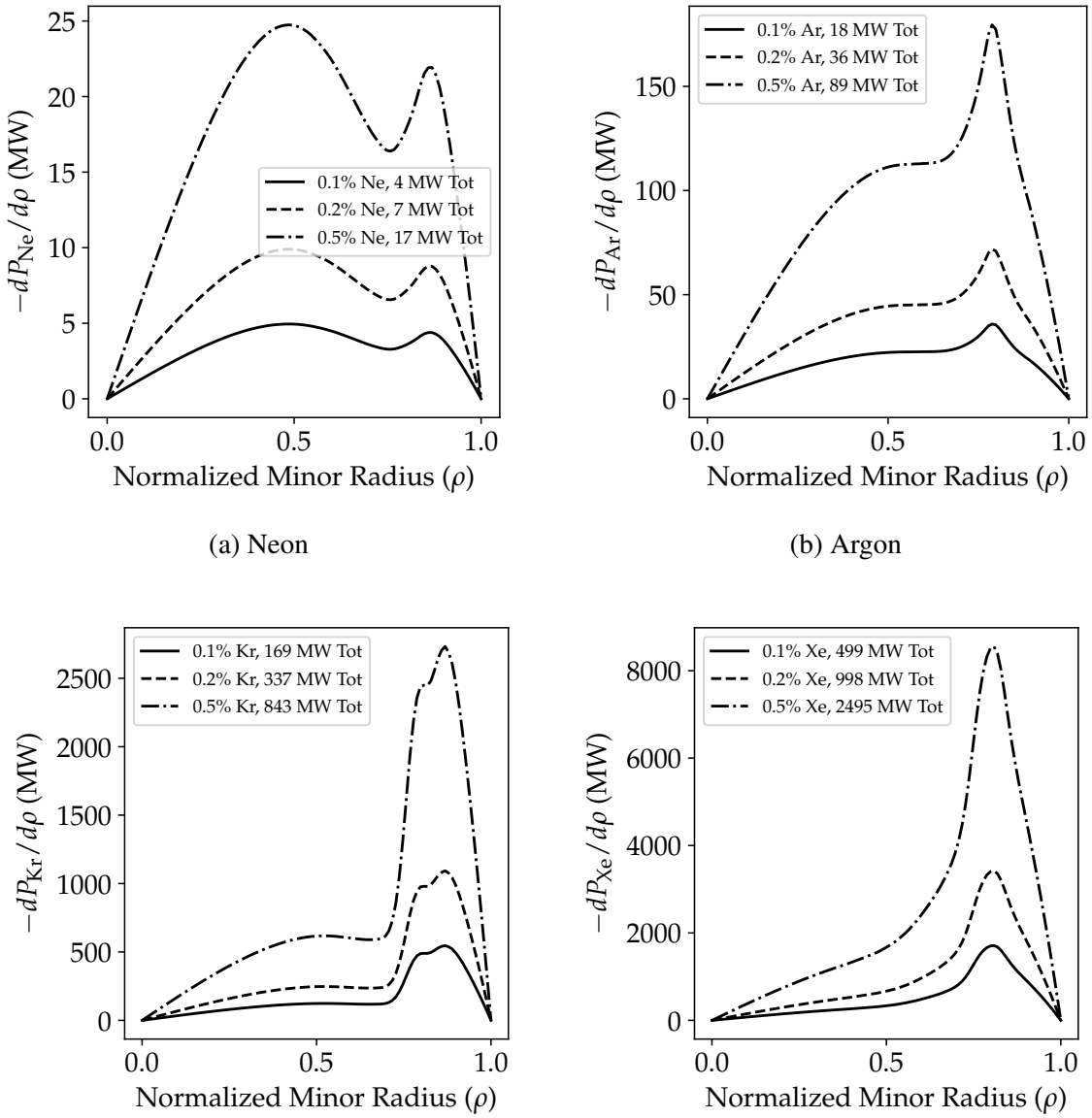

(a) Neon

(b) Argon

(c) Krypton

(d) Xenon

Figure 4.13: Total Radial Loss profiles $dP/d\rho\,(\rho)$ for noble gases for several impurity concentrations. These were calculated using ADPAK data and the GT3 tokamak analytics code described in Appendix B

Although the radial radiative loss profiles of krypton and xenon are both peaked in the edge, the total amount of power radiated is too high, which is consistent with the data shown in Figure 4.10. Argon's loss profile is peaked in the edge and the total amount power loss that could be achieved would be neither too large nor too small for meaningful control to be achieved.

4.7 Impurity Radiation and Burn Control Conclusions

This chapter has explored the possibilities of using impurity radiation as part of a burn control strategy. Unfortunately, this analysis suggests that impurities will offer little in the way of a passive stability mechanism due to the lack of significantly positive temperature dependences in the various species' L_z functions in the temperature range expected in ITER.

Active impurity seeding, however, is likely to play an important role in controlling the burn condition. Noble gases have long been investigated for radiative power exhaust because of their non-reactive properties, and of the noble gases, neon and argon are the most useful. Krypton and higher-z noble gases would likely radiate too strongly. Radiative power exhaust of between 10 and 100 MW can be achieved using reasonable neon and argon concentrations. These concentrations could be achieved using dedicated burn control pellets or, potentially massive gas injection. Argon's radial power loss profile is peaked in the edge, which could make it particularly useful for removing power deposited in the edge via EC or in response to an edge power excursion.

Finally, recent results at DIII-D suggest that by varying the on-axis ECCD, plasma controllers could modify impurity concentrations in the inner core. This could prove to be an important active burn control mechanism as it is one of relatively few actuators that can directly effect conditions in the inner core. Additional research is necessary to determine the timescale on which this mechanism could respond to power excursions, but it could also be used to tune the power balance to prevent power excursions.

CHAPTER 5

ION ORBIT LOSS AND POWER EXHAUST

A framework for quantifying the direct ion orbit loss (IOL) of energetic ions from the plasma was developed by Miyamoto [51] and has since been investigated [52] as a potentially important mechanism for a wide variety of tokamak phenomenon, including the shape of the radial electric field E_r [52] and heat and particle transport in the edge [53, 54]. Of particular interest to this research is the temperature dependence implicit in the calculation of particle, energy, and momentum ion orbit loss fractions. As will be discussed in subsequent sections, the threshold velocity for a particle to be lost v_{esc} is independent of temperature of the background plasma. As a result, an increase in the overall ion temperature distribution would increase the number of energetic particles with velocities $v \geq v_{esc}$ that would be lost. It is plausible that this phenomenon could act as a passive feedback mechanism against positive power excursions. The purpose of this chapter is to explore this possibility.

5.1 Ion Orbit Loss Theory

5.1.1 Basic Equations

The criteria for an ion to be lost can be obtained by conserving energy, magnetic moment, and canonical toroidal angular momentum, shown below in Equations 5.1 through 5.3 respectively.

$$\frac{1}{2}m\left(V_{\parallel}^2 + V_{\perp}^2\right) + Ze\phi = \text{const} = \frac{1}{2}mV_0^2 + Ze\phi_0 \tag{5.1}$$

$$\frac{mV_{\perp}^2}{2B} = \text{const} = \frac{mV_{\perp,0}^2}{2B_0} \tag{5.2}$$

$$RmV_{\parallel} f_{\phi} + Ze\psi = \text{const} = R_0 m V_{\parallel,0} f_{\phi,0} + Ze\psi_0 \tag{5.3}$$

Here m is the mass of the particle, $V_{\parallel}$ and $V_{\perp}$ are the particle's parallel and perpendicular velocities, respectively, Z is the atomic number of the ion, e is the charge of the electron, B is the total magnetic field, R is the major radius of the particle, $f_{\phi} = |B_{\phi}/B|$, B_{ϕ} is the strength of the toroidal magnetic field, and ψ is the enclosed magnetic flux of the flux surface the particle is on. In these equations, a 0-subscript indicates the value at the particle's starting position.

Equations 5.1 through 5.3 can be combined to obtain a quadratic equation, shown in Equation 5.4, for the initial velocity of the particle whose path would include another point with specified values of B, f_{ϕ}, ψ, R, and ϕ.

$$V_0^2 \left[\left(\left| \frac{B_s}{B_0} \right| \frac{f_{\phi,0}}{f_{\phi,s}} \zeta_0 \right)^2 - 1 + \left(1 - \zeta_0^2\right) \left| \frac{B_s}{B_0} \right| \right] + V_0 \left[\frac{2e\left(\psi_0 - \psi_s\right)}{Rmf_{\phi,s}} \left(\left| \frac{B_s}{B_0} \right| \frac{f_{\phi,0}}{f_{\phi,s}} \zeta_0 \right) \right] + \left[\left(\frac{e\left(\psi_0 - \psi_s\right)}{Rmf_{\phi,s}} \right)^2 - \frac{2e\left(\phi_0 - \phi_s\right)}{m} \right] = 0 \tag{5.4}$$

Here, an s-subscript denotes the value at the particle loss surface (the seperatrix) for which V_0 is to be found, and $\zeta_0 = V_{\parallel,0}/V_0$ is the cosine of the initial guiding center velocity relative to the toroidal magnetic field direction.

Equation 5.4 can be solved for v_0 using the quadratic equation shown in Equation 5.5, where a, b, and c are as shown below. Of the two mathematical solutions to Equation 5.5, the lowest positive solution is taken as the physical solution, since v_0 is a speed and directionality is represented by ζ_0. If there are no positive solutions, it is assumed that there are no physical solutions.

$$v_0 = \frac{-b \pm \sqrt{b^2 - 4ac}}{2a} \tag{5.5}$$

$$a = \left(\left| \frac{B_s}{B_0} \right| \frac{f_{\phi,0}}{f_{\phi,s}} \zeta_0 \right)^2 - 1 + \left(1 - \zeta_0^2\right) \left| \frac{B_s}{B_0} \right| \tag{5.6}$$

$$b = \frac{2e\left(\psi_0 - \psi_s\right)}{Rmf_{\phi,s}} \left(\left| \frac{B_s}{B_0} \right| \frac{f_{\phi,0}}{f_{\phi,s}} \zeta_0 \right) \tag{5.7}$$

$$c = \left(\frac{e\left(\psi_0 - \psi_s\right)}{Rmf_{\psi,s}} \right)^2 - \frac{2e\left(\phi_0 - \phi_s\right)}{m} \tag{5.8}$$

5.1.2 Particle, Momentum, and Energy Losses

For IOL, (as opposed to ion orbit transport that does not result an immediate loss) we are specifically concerned with particle destinations along the seperatrix. Particles with an initial velocity V_0 and an initial angle cosine ζ_0 that can reach a point on the seperatrix are assumed to be lost from the confined plasma at that location.

By making a few reasonable simplifying assumptions, it is possible to estimate the cumulative fraction of particles that are lost via direct ion orbit loss. Those assumptions are listed below.

1. Collisions are ignored. One effect of this is to decouple initial directions from each other. Each launch angle in the calculation is treated independently from the others.

2. Ions will sample every poloidal location on the flux surface many times before being transported a small radial distance. Those that can reach the seperatrix from a particular poloidal location do so. Those that can't escape from any poloidal location, are assumed to stay on the flux surface and move radially outward through normal transport processes.

3. Thermal particles exist in a Maxwellian distribution with an average value related to the local average ion temperature. The velocity distribution is truncated above the minimum speed needed for escape, which is a function of ζ_0. Particles above that value are assumed to have been lost either on that surface or on a more interior surface.

The cumulative fraction of particles lost for a radial location ρ, $F_{orb}\left(\rho\right)$, can be obtained by calculating the fraction of the local velocity distribution $f\left(V_0\right)$ that has been lost via IOL by the time the particles originating at the center of the plasma reach the flux surface $\psi_s\left(r\right)$, and then integrating over all launch angle cosines.

$$F_{orb} \equiv \frac{N_{loss}}{N_{tot}} = \frac{\int_{-1}^{1} d\zeta_0 g\left(\zeta_0\right) \int_{V_{0,\min(\zeta_0)}}^{\infty} dV_0 V_0^2 f\left(V_0\right)}{\int_{-1}^{1} d\zeta_0 g\left(\zeta_0\right) \int_{0}^{\infty} dV_0 V_0^2 f\left(V_0\right)} \tag{5.9}$$

Similar equations can be written for the cumulative momentum (M_{orb}) and energy (E_{orb}) loss fractions.

$$M_{orb} = \frac{\int_{-1}^{1} d\zeta_0 g\left(\zeta_0\right) \int_{V_{0,\min(\zeta_0)}}^{\infty} dV_0 \left(mV_0\zeta_0\right) V_0^2 f\left(V_0\right)}{\int_{-1}^{1} d\zeta_0 g\left(\zeta_0\right) \int_{0}^{\infty} dV_0 \left(mV_0\right) V_0^2 f\left(V_0\right)} \tag{5.10}$$

$$E_{orb} = \frac{\int_{-1}^{1} d\zeta_0 g\left(\zeta_0\right) \int_{V_{0,\min(\zeta_0)}}^{\infty} dV_0 \left(\frac{1}{2}mV_0^2\right) V_0^2 f\left(V_0\right)}{\int_{-1}^{1} d\zeta_0 g\left(\zeta_0\right) \int_{0}^{\infty} dV_0 \left(\frac{1}{2}mV_0^2\right) V_0^2 f\left(V_0\right)} \tag{5.11}$$

For species with isotropic launch trajectories ($g\left(\zeta_0\right) = 1/2$) these equations can be rewritten using the Gamma function $\Gamma\left(x\right)$ and incomplete Gamma function $\Gamma\left(x,s\right)$.

$$F_{orb} = \frac{\int_{-1}^{1} d\zeta_0 \Gamma\left(3/2, \epsilon_{\min(\zeta_0)}\right)}{2\Gamma\left(3/2\right)} \tag{5.12}$$

$$M_{orb} = \frac{\int_{-1}^{1} d\zeta_0 \zeta_0 \Gamma\left(2, \epsilon_{\min(\zeta_0)}\right)}{2\Gamma\left(2\right)} \tag{5.13}$$

$$E_{orb} = \frac{\int_{-1}^{1} d\zeta_0 \Gamma\left(5/2, \epsilon_{\min(\zeta_0)}\right)}{2\Gamma\left(5/2\right)} \tag{5.14}$$

In a Maxwellian distribution, such as the background thermal ion species, $\epsilon_{\min(\zeta_0)}$ is given by

$$\epsilon_{\min(\zeta_0)} = \frac{mV_{0\min}^2\left(\zeta_0\right)}{2kT_{\text{ion}}} \tag{5.15}$$

For a monoenergetic, isotropic species with energy V_α, such as uncollided fusion α-

particles, Equations 5.9 through 5.11 reduce to the forms shown in Equations 5.16 through 5.18

$$F_{orb}\left(\rho_0\right) = \frac{\int_{-1}^{1} d\zeta_0 \int_{V_{0,\min(\zeta_0,\rho_0)}}^{\infty} dV_0 V_0^2 \delta\left(V_0 - V_\alpha\right)}{\int_{-1}^{1} d\zeta_0 \int_{0}^{\infty} dV_0 V_0^2 \delta\left(V_0 - V_\alpha\right)}$$

$$= \frac{1}{2}\int_{-1}^{-1} d\zeta_0 H\left(V_\alpha - V_{0,\min(\zeta_0,\rho_0)}\right) \quad (5.16)$$

$$M_{orb}\left(\rho_0\right) = \frac{\int_{-1}^{1} d\zeta_0 \zeta_0 \int_{V_{0,\min(\zeta_0,\rho_0)}}^{\infty} dV_0 \left(mV_0\right) V_0^2 \delta\left(V_0 - V_\alpha\right)}{\int_{-1}^{1} d\zeta_0 \int_{0}^{\infty} dV_0 \left(mV_0\right) V_0^2 \delta\left(V_0 - V_\alpha\right)}$$

$$= \frac{1}{2}\int_{-1}^{-1} d\zeta_0 \zeta_0 H\left(V_\alpha - V_{0,\min(\zeta_0,\rho_0)}\right) \quad (5.17)$$

$$E_{orb}\left(\rho_0\right) = \frac{\int_{-1}^{1} d\zeta_0 \int_{V_{0,\min(\zeta_0,\rho_0)}}^{\infty} dV_0 \left(\frac{1}{2}mV_0^2\right) V_0^2 \delta\left(V_0 - V_\alpha\right)}{\int_{-1}^{1} d\zeta_0 \int_{0}^{\infty} dV_0 \left(\frac{1}{2}mV_0^2\right) V_0^2 \delta\left(V_0 - V_\alpha\right)}$$

$$= \frac{1}{2}\int_{-1}^{-1} d\zeta_0 H\left(V_\alpha - V_{0,\min(\zeta_0,\rho_0)}\right) \quad (5.18)$$

where

$$H\left(x\right) = \int_{-\infty}^{x} \delta\left(s\right) ds \quad (5.19)$$

is the Heaviside function.

For a monoenergetic, monodirectional species with energy V_B and direction cosine ζ_B, such as many of the beam ions, Equations 5.9 through 5.11 reduce to the forms shown below.

$$F_{orb}\left(\rho_0\right) = \frac{\int_{-1}^{1} d\zeta_0 \delta\left(\zeta_0 - \zeta_B\right) \int_{V_{0,\min(\zeta_0,\rho_0)}}^{\infty} dV_0 V_0^2 \delta\left(V_0 - V_B\right)}{\int_{-1}^{1} d\zeta_0 \delta\left(\zeta_0 - \zeta_B\right) \int_{0}^{\infty} dV_0 V_0^2 \delta\left(V_0 - V_B\right)}$$

$$= \frac{H\left(V_B - V_{0,\min(\zeta_B,\rho_0)}\right)}{H\left(1-\zeta_B\right) H\left(1+\zeta_B\right)}$$

$$= H\left(V_B - V_{0,\min(\zeta_B,\rho_0)}\right) \quad (5.20)$$

$$M_{orb}\left(\rho_0\right) = \frac{\int_{-1}^{1} d\zeta_0 \zeta_0 \delta\left(\zeta_0 - \zeta_B\right) \int_{V_{0,\min(\zeta_0,\rho_0)}}^{\infty} dV_0 \left(mV_0\right) V_0^2 \delta\left(V_0 - V_B\right)}{\int_{-1}^{1} d\zeta_0 \delta\left(\zeta_0 - \zeta_B\right) \int_{0}^{\infty} dV_0 \left(mV_0\right) V_0^2 \delta\left(V_0 - V_B\right)}$$

$$= \zeta_B \frac{H\left(V_B - V_{0,\min(\zeta_B,\rho_0)}\right)}{H\left(1-\zeta_B\right) H\left(1+\zeta_B\right)}$$

$$= \zeta_B H\left(V_B - V_{0,\min(\zeta_B,\rho_0)}\right) \quad (5.21)$$

$$E_{orb}\left(\rho_0\right) = \frac{\int_{-1}^{1} d\zeta_0 \delta\left(\zeta_0 - \zeta_B\right) \int_{V_{0,\min(\zeta_0,\rho_0)}}^{\infty} dV_0 \left(\frac{1}{2}mV_0^2\right) V_0^2 \delta\left(V_0 - V_B\right)}{\int_{-1}^{1} d\zeta_0 \delta\left(\zeta_0 - \zeta_B\right) \int_{0}^{\infty} dV_0 \left(\frac{1}{2}mV_0^2\right) V_0^2 \delta\left(V_0 - V_B\right)}$$

$$= \frac{H\left(V_B - V_{0,\min(\zeta_B,\rho_0)}\right)}{H\left(1-\zeta_B\right) H\left(1+\zeta_B\right)}$$

$$= H\left(V_B - V_{0,\min(\zeta_B,\rho_0)}\right) \quad (5.22)$$

5.2 Temperature Dependence of IOL

The derivation of the equation for the minimum escape velocity (Equation 5.4) is independent of the density or temperature of the background plasma, as IOL is a kinetic phenomenon and n and T are fluid quantities. As a result, an increase in the average kinetic energy of a species would increase the number of particles meeting the criteria to be lost

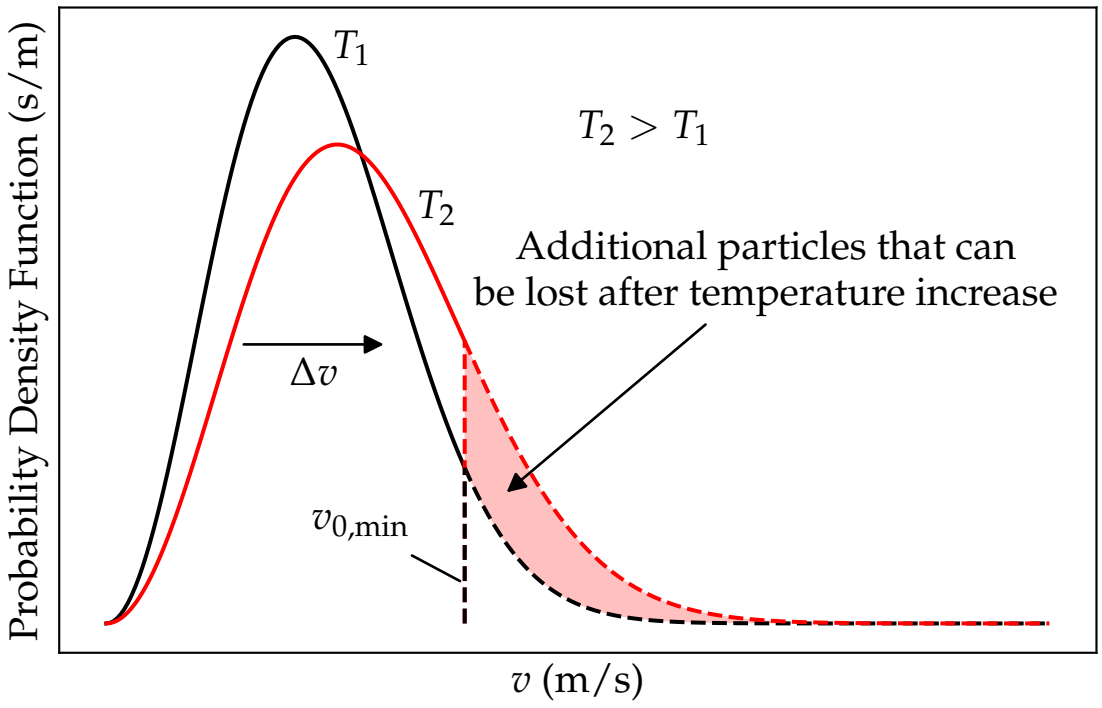

Figure 5.1: An illustration of how an increase in temperature results in increased particle losses. As the average temperature increases, more particles with a given launch angle cosine will have velocities exceeding $v_{0,\min}$ and will be lost across the seperatrix.

via IOL and remove their energy from the system. This is illustrated in Figure 5.1.

It is clear that a temperature increase resulting from a thermal power excursion would increase the amount of particle and energy loss through IOL, all else being equal. What is not yet clear is the magnitude of this loss of energy and fuel. It may also be the case that indirect effects of an increase in IOL (such as increased rotation, increased power exhaust into the divertor, etc.) may enhance or counteract any positive effects of IOL.

For mono-energetic species, including fusion α-particles and uncollided beam ions, neither F_{orb}, M_{orb}, nor E_{orb} change in response to an increase in the background plasma temperature (although the NBI and α-particle deposition profiles may change, which could effect IOL). These species are less interesting from a burn control perspective.

Ion species that have largely come into thermal equilibrium with the background plasma do become more likely to be lost as a result of a general temperature increase. These species

Table 5.1: Categorization of plasma ion species based on direction and energy distributions.

	Mono-Directional	Partially Isotropized	Isotropic
Mono-Energetic	• Uncollided beam ions ionized via electron ionization		• Uncollided fusion α-particles • Uncollided beam ions ionized via charge exchange
Partially Thermalized		• Uncollided beam ions ionized via ion ionization • Once-collided beam ions that were ionized via electron ionization	• Once-collided fusion α-particles
Fully Thermalized			• Hydrogenic background plasma ions • Impurity ions • Several-times-collided fusion α-particles

Table 5.2: Parameters for ITER model for IOL calculations

a	$2.0\,\mathrm{m}$	n_0	$3.629 \times 10^{19}\,\mathrm{m}^{-3}$
$R_{0,a}$	$6.2\,\mathrm{m}$	n_{ped}	$1.523 \times 10^{19}\,\mathrm{m}^{-3}$
Z_0	$0.6\,\mathrm{m}$	n_{sep}	$0.3 \times 10^{19}\,\mathrm{m}^{-3}$
κ_{sep}	1.7	ν_n	3.0
s_κ	0.1	T_0	$35\,\mathrm{keV}$
δ_{sep}	0.35	T_{ped}	$6\,\mathrm{keV}$
j_0	$0.8\,\mathrm{MA\,m}^{-2}$	T_{sep}	$0.6\,\mathrm{keV}$
j_{sep}	$0.1\,\mathrm{MA\,m}^{-2}$	ν_T	3.5
ν_j	0.7	ρ_{ped}	0.9
$I_P{}^*$	$9.731\,\mathrm{MA}$	$B_{\phi,0}$	$5.3\,\mathrm{T}$

* I_P is calculated from $j\,(\rho)$ and Miller geometry.

will be the primary focus of our investigation of energy loss through direct IOL. A later section will comment on the potential indirect consequences of IOL for power exhaust, as well as the potential implications of including collisions in the model.

5.3 IOL Calculations in ITER

Calculations of IOL in DIII-D have consistently shown that the effects of IOL are mostly confined to the edge region of the plasma ($\rho \gtrsim 0.9$). Given the importance of physics phenomena in this region (as well as our incomplete understanding of them), it is natural to hypothesize that IOL may have an important role to play. This possibility has been the subject of intense research in the last few years, led primarily by researchers at Georgia Tech [55, 56, 57]. This section will apply the IOL model described earlier in this chapter to ITER to evaluate the role that IOL may play in burn control.

For this calculation, the ITER geometry, ψ, and B_θ were calculated using a version of the Miller model [58] that has been modified to include the x-point, and which is described in greater detail in Appendix D. The resulting ITER geometry is shown in Figure 5.2. Radial density and temperature distributions were modeled using the same model as described in Chapter 3. The geometry and radial profile parameters used for the reference ITER background plasma are listed in Table 5.2.

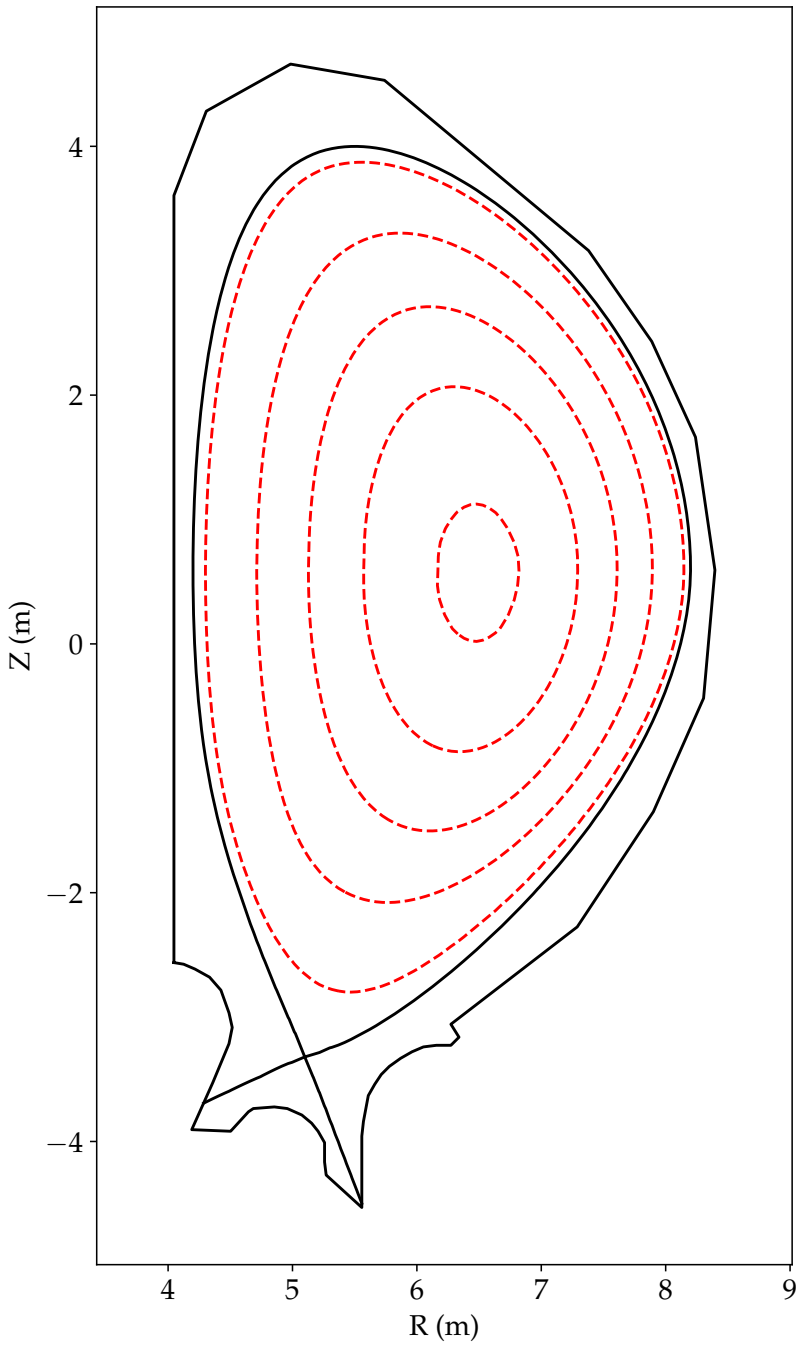

Figure 5.2: ITER geometry used for IOL and other ITER related calculations. This geometry was generated using the modified Miller model described in Appendix D

.

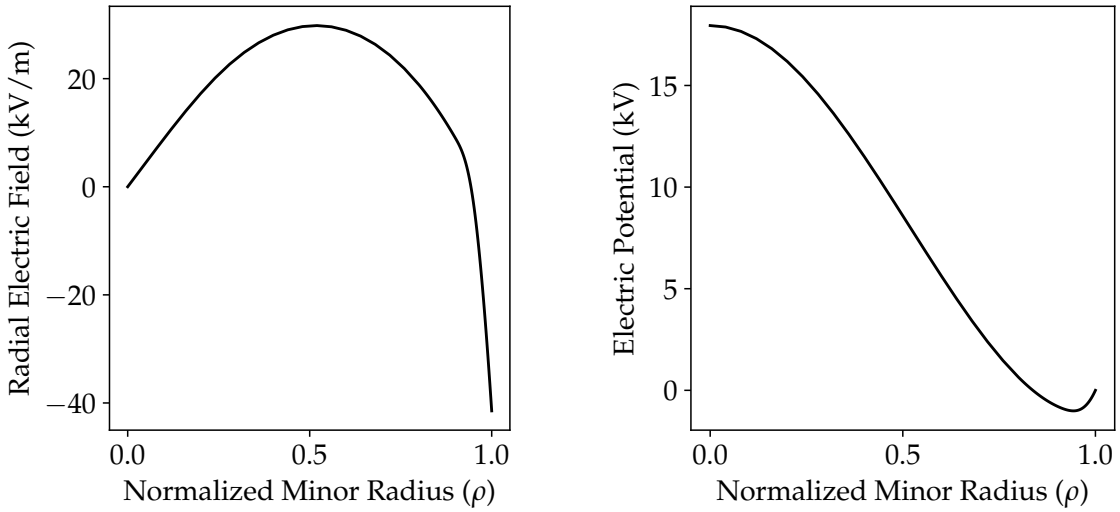

(a) Radial electric field taken from a predictive analysis of H-mode in ITER [48]

(b) Electric potential based on the radial electric field in (a)

Figure 5.3: E_r and the resulting ϕ as functions of ρ for the reference ITER background plasma used in this analysis.

The only parameter in Equation 5.5 that cannot be obtained from the parameters in Table 5.2 is the radial electrostatic potential ϕ, which is obtained by integrating the radial electric field E_r, as shown below.

$$\phi\left(r\right) = \int_{r}^{a} E_r\left(r'\right) dr' \tag{5.23}$$

In practice, E_r is calculated from the radial momentum balance equation

$$E_r^{\exp} = \frac{1}{n_k e_k}\frac{\partial p_k}{\partial r} - \left(V_{\theta,k}B_\phi - V_{\phi,k}B_\theta\right) \tag{5.24}$$

for one of the ion species (usually carbon) denoted by k using experimentally measured toroidal and poloidal rotation velocities, $V_{\phi,k}$ and $V_{\theta,k}$. For this analysis, the E_r profile was taken from a predictive analysis of H-mode performance in ITER [48]. The $E_r\left(\rho\right)$ profile and the resulting $\phi\left(\rho\right)$ profile are shown in Figure 5.3.

The cumulative energy loss fraction, E_{orb}, was calculated for fast, mono-energetic α-particles, as well as for thermalized α-particles and deuterium. Additionally, the sensitivity

of E_{orb} to changes in several parameters was investigated to assess the effectiveness of IOL as a passive mechanism and to suggest possible active IOL-related control mechanisms. Specifically,

1. The core temperature was varied from 10-60 keV. The edge temperature was fixed to better represent a core power excursion.

2. The strength of the toroidal magnetic field at the magnetic axis, $B_{\phi,0}$ was varied from 2.6 to 10.6 T to explore the sensitivity of IOL to changes in B over a wide range of $B_{\phi,0}$ that might be encountered in ITER and subsequent devices.

3. The radial electric field strength, E_r, was varied from 0.5 to 2.0 times the values used in the reference scenario. Profiles are shown in Figure 5.4. This can be thought of as a proxy for varying the degree of rotation.

4. Finally, the current density profile, $j_r\left(\rho\right)$, was varied as shown in Figure 5.5. This can be thought of as a proxy for changing the plasma current or current profile.

Of the four parameter scans, only changes in the current profile had a significant effect on the E_{orb} profiles, with decreased current corresponding to greater energy losses from IOL. The sensitivity of E_{orb} to changes in current is illustrated for fast α-particles in Figure 5.6 and for thermalized deuterium in Figure 5.7.

An estimate of power losses from thermal IOL can be obtained by estimating an effective loss fraction, volume, ion density and temperature, and approximate transport time for the far-edge plasma region ($0.98 \lesssim \rho \lesssim 1.0$) in which thermal IOL is significant. For the ITER thermal IOL calculations described above, this results in an estimated 1.45 MW power loss in steady state. This 1.45 MW does not measurably change in response to changes in the core or edge temperature distributions.

The fact that thermal IOL was essentially non-existent in the core region for the reference ITER scenario and did not vary significantly with changes in core temperature leads

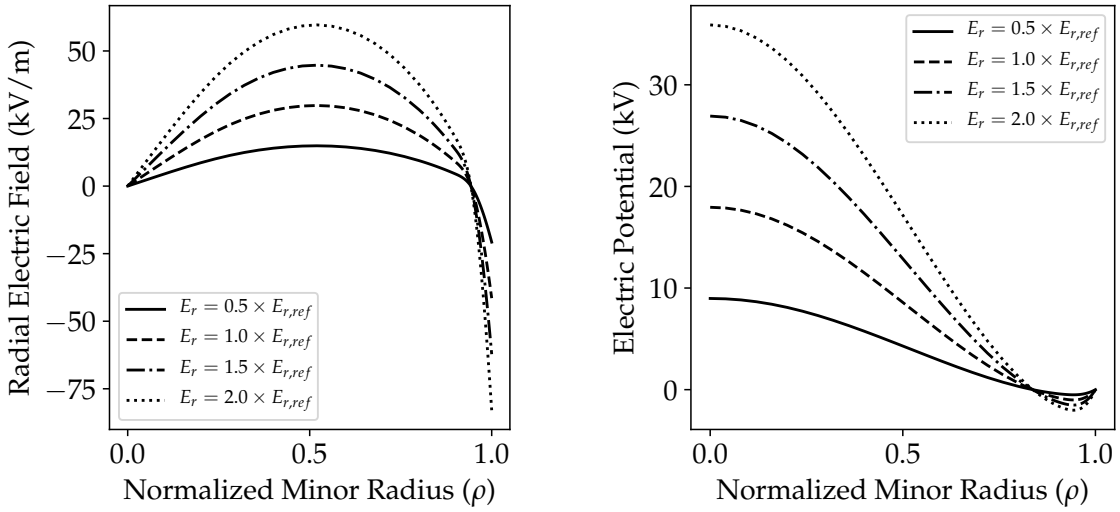

(a) Variations in E_r used to evaluate the sensitivity of IOL quantities to changes in ϕ

(b) ϕ calculated from the radial electric fields in (a)

Figure 5.4: E_r and the resulting ϕ as functions of ρ for the reference ITER background plasma used in this analysis.

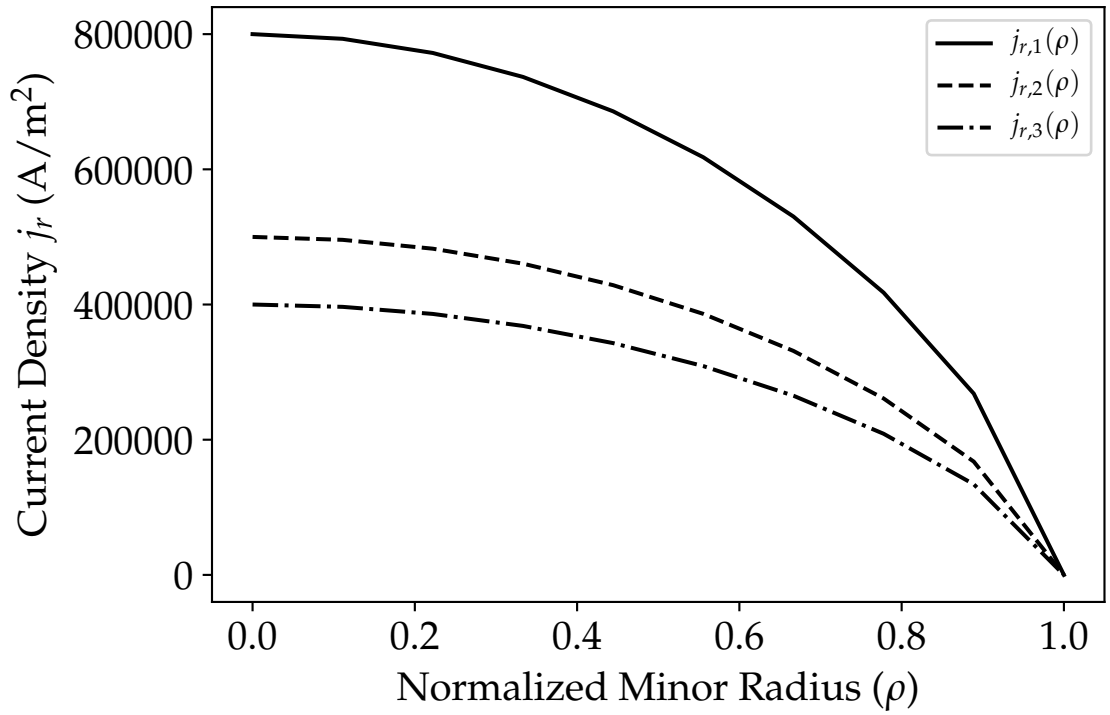

Figure 5.5: Current profile scan used for evaluating the effect of changes in current on IOL.

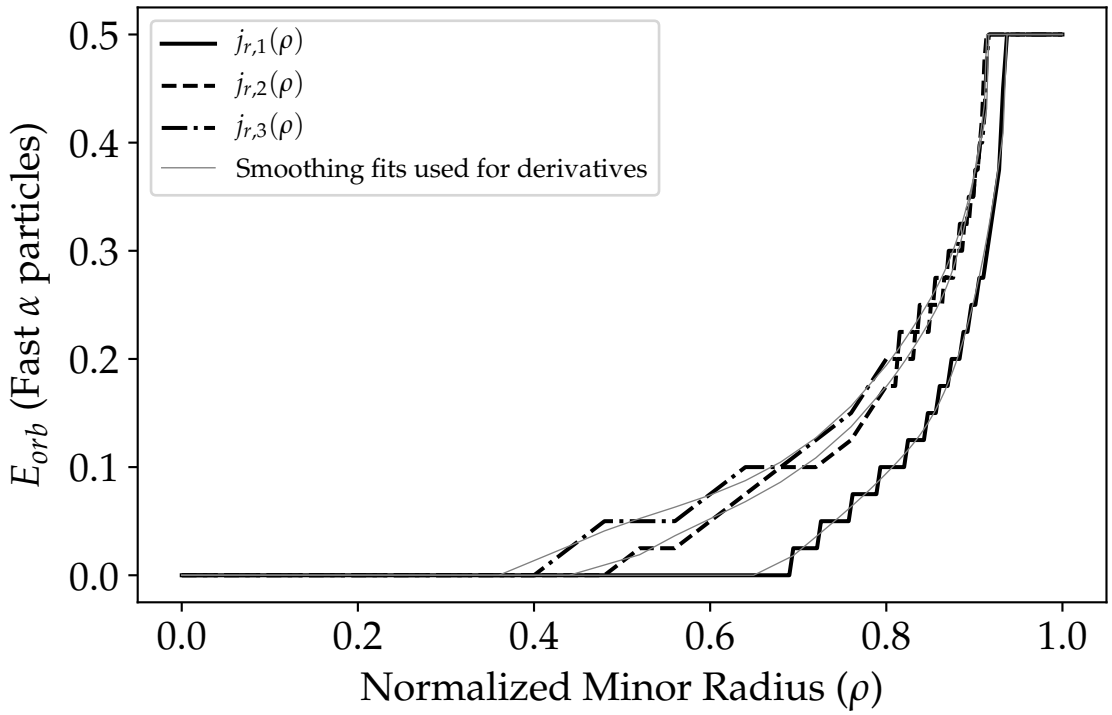

Figure 5.6: E_{orb} for fast α particles for each of the current profiles shown in Figure 5.5. Although E_{orb} becomes significant at a smaller ρ for fast α particles than for thermalized species, it only becomes significant in the inner core for reduced current scenarios.

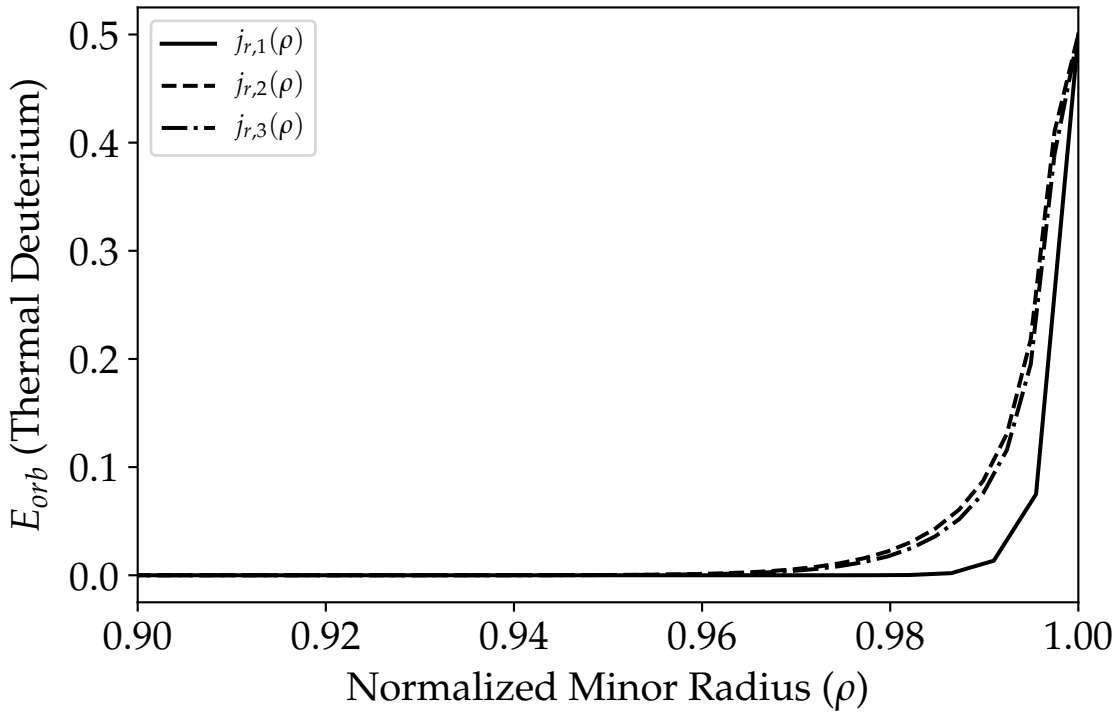

Figure 5.7: E_{orb} for thermalized deuterium for each of the current profiles shown in Figure 5.5. Note that the scale on the x-axis goes from 0.9 to 1.0. Thermal IOL in ITER will likely occur only in the very far edge plasma ($\rho \gtrsim 0.98$).

us to conclude that IOL is not a significant passive feedback mechanism against core power excursions.

Figure 5.6 suggests that Fast-α IOL is unlikely to be successful as an active feedback mechanism, since even halving the total current is barely enough to have IOL of fast α-particles in the inner core. Such a drastic reduction in current would be impossible on the timescale of power excursion. As a result, it seems unlikely that increased IOL of fast α-particles through a reduction in plasma current will offer an effective active feedback mechanism.

As an aside, the increased IOL of 3.5 MeV α-particles resulting from a change in current could have important implications for current rampdown and disruptions in burning plasmas. More research is needed on the effect of high-energy α-particles impinging on plasma facing components. These problems could conceivably be mitigated by a period of deuterium-only fueling prior to rampdown to maintain the core ion density while reducing the fast α-particle generation rate.

5.4 IOL and Edge Power Exhaust

The temperature dependence of IOL illustrated in Figure 5.1 raises the possibility that power deposited in the edge from the core either quickly via EC or slowly through collisional transport could be removed via IOL. Figure 5.7 shows the $E_{\rm orb}$ profile of thermalized deuterium in ITER for the current density profiles discussed in the previous section. The most important observation is that loss fraction does not become significant until just barely inside the seperatrix (note the ρ range in the x-axis). The implication is that increased thermal IOL will likely be ineffective at removing power deposited in all plasma regions except for the very far edge, as shown in Figure 5.7. However, before IOL could assist in power exhaust in the edge, any power deposited at $\rho \lesssim 0.98$ would have to be transported through other mechanisms almost all of the way to the seperatrix anyway.

5.5 Ion Orbit Loss Conclusions

This chapter analyzed ion orbit loss in ITER using GT3 to evaluate its potential as a negative feedback mechanism against positive power excursions. IOL of thermalized particles increases with increasing temperature, however loss fractions in ITER are significant only in the very far edge ($\rho \gtrsim 0.98$) and will not help to offset a power excursion in the central core. Energy deposited in the outer core (i.e. from EC radiation transport) will have to be transported through other mechanisms to very far edge plasma before it can be exhausted via IOL.

IOL of fast α particles, although not dependent on the background plasma temperature, could have effects on the power balance in the core, especially in the outer core where there is both a significant fast α loss fraction and the possibility of a significant amount of fusion power. Fast α loss fractions were found to be most sensitive to changes in plasma current. Although rapid changes in plasma current are unlikely to be useful as an active negative feedback mechanism for burn control, this raises the possibility of fast α IOL effecting the dynamics of the plasma during current rampdown.

Additionally, this analysis has focused only on those particles that can reach the seperatrix. Ion orbit transport is a separate subject and is the subject of ongoing investigation. It is conceivable that fast α particles could be transported to other internal flux surfaces and deposit their energy there. Collisions would need to be included in the model to evaluate those effects.

CHAPTER 6

MARFE-INITIATED H-L TRANSITION AS A CONTROL MECHANISM

A regime of tokamak operation that exhibited significantly improved confinement characteristics was first reported in 1982 and has since become known as "H-mode" [59]. The low-confinement regime that was the standard operating regime prior to that time is now known as "L-mode." In H-mode, steep density and temperature gradients form in the edge region of the plasma. The increased edge densities and temperatures result in increased densities and temperatures throughout the plasma, as if the entire radial profiles were lifted up on a pedestal. The edge region in H-mode plasmas is often referred to as the edge pedestal for this reason.

While the exact physical mechanisms involved in transitions from L- to H-mode and vice-versa are still areas of active research, it has been observed that a certain amount of power must be transported (conducted or convected) radially outward across the seperatrix for a plasma to stay in H-mode. An empirical relationship [8] that predicts the onset of H-mode in tokamaks is

$$P_{\mathrm{LH}}^{(\mathrm{MW})} = \frac{2.84}{M} B_{\phi 0}^{0.82} n_{e20}^{-0.58} R a^{0.81} \tag{6.1}$$

where, M is the plasma ion mass in AMU, n_{e20} is the line-averaged electron density, $B_{\phi,0}$ is the toroidal magnetic field strength at the magnetic axis, and a is the minor radius of the plasma.

Multi-faceted Asymmetric Radiation From the Edge (MARFE) is the name given [60] to a phenomenon in which a toroidally uniform, poloidally localized region in the edge plasma experiences a radiative condensation type of thermal instability. These highly radiating regions typically begin in the divertor (divertor MARFE) and move into the confined

plasma near the x-point region (core MARFE). As the energy is radiated away in the vicinity of a core MARFE, the plasma cools and the local density increases as particles move along flux surfaces to maintain a uniform pressure on the flux surface.

One nearly universal consequence of core MARFE formation is a back-transition from H- to L-mode confinement. This seems to result from the fact that the increased power that MARFE's radiate is no longer available to be transported across the seperatrix, and transported energy drops below the threshold of Equation 6.1.

MARFEs could be important phenomena in burning plasmas for at least five reasons:

1. H-L transitions caused by deliberately initiated MARFEs could be useful as a part of an active burn control strategy.

2. It is conceivable that MARFEs could also be useful in a passive control strategy (e.g. if the MARFE onset criteria were found to have a positive temperature dependence).

3. Core MARFEs are a potential way to radiate energy deposited in the edge region by EC radiation generated in the core during a thermal power excursion.

4. Even if not used for limiting thermal power excursions, MARFEs and their effects on plasma confinement are important for the overall power balance. Active control algorithms should take into account the likelihood of triggering a core MARFE and its likely effects.

5. In some situations, core MARFEs have been observed to be followed by a thermal collapse of the core temperature profile, resulting in a disruption.

If disruptions can be avoided, a core MARFE and the likely back-transition to L-mode could conceivably be part of a strategy for limiting thermal power excursions. The purpose of this chapter is to explore the role of MARFEs in burning plasma physics and the extent to which MARFEs could be useful as part of a burn-control strategy.

6.1 H-L Transition Timescales

Transitions from H-mode to L-mode are typically identified by a collapse in the steep density and temperature gradients of the H-mode pedestal and by enhanced D_α radiation. This collapse occurs on a fairly fast timescale ($\sim$ tens of ms), although the effects of the transition on confinement may manifest over a longer time period.

Of particular interest to burn control applications are the timescales on which a core MARFE and the resulting H-L transition could effect conditions in the core. A proper treatment of the transport considerations involved in an H-L transition in ITER is beyond our current capabilities and certainly beyond the scope of this thesis; however a substantial amount of insight can be obtained by examining the evolution of a MARFE in the DIII-D tokamak.

For this analysis, we will use DIII-D shot 92976, which was previously included in a study of MARFEs at Georgia Tech [61, 62]. This shot experienced a MARFE and subsequently dropped from H-mode into L-mode. Time traces of the bolometer readings from the chord passing near the x-point, the electron density, and the electron temperature for this shot are shown in Figure 6.1.

The bolometer array on DIII-D [63] is an array of heat sensors around the plasma chamber that are useful for detecting radiation levels in various parts of the plasma. Here, we use the fourth chord in the lower bolometer array, which is marked with red 'x's in Figure 6.2, which passes through the region just above the x-point where the MARFE will radiate after it crosses the seperatrix into the confined plasma. The significant spike in the the bolometer readings in the top chart of Figure 6.1 is indicative of the MARFE.

The density and temperature measurements in Figure 6.1 are taken from the Thomson scattering system [64] and are measured at the point indicated by the red circle in Figure 6.3.

The story told by the data in Figure 6.1 is as follows:

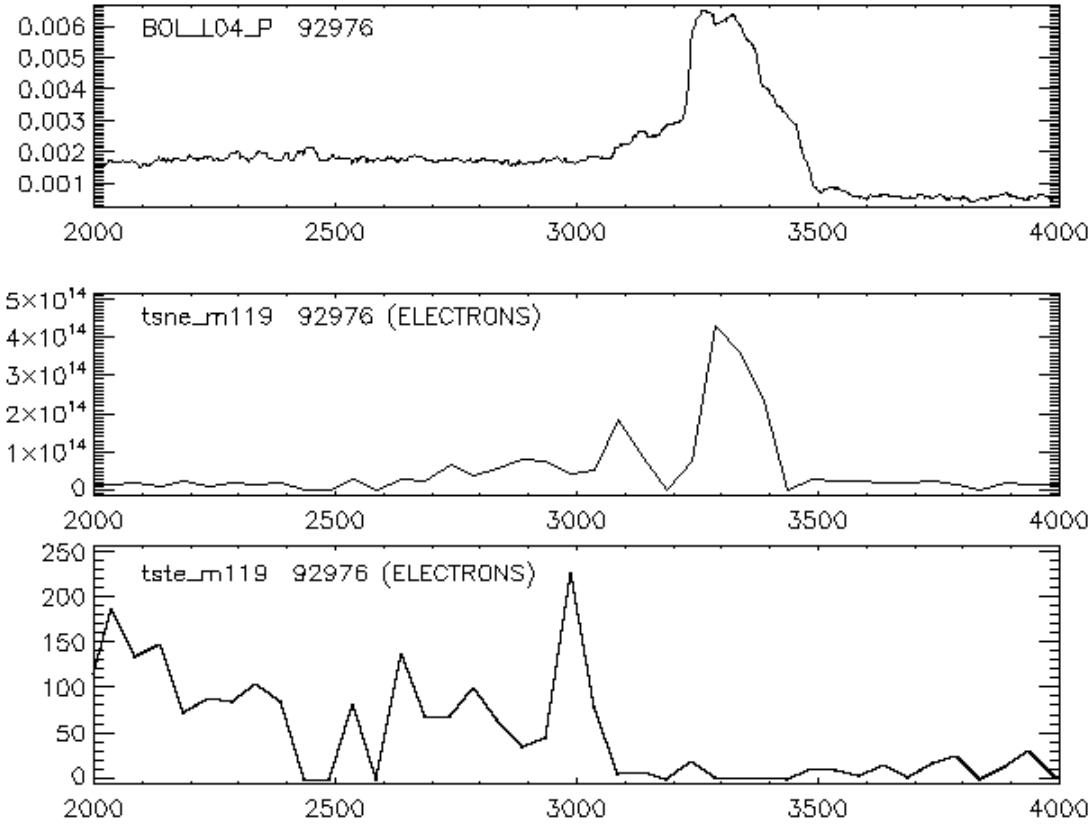

Figure 6.1: Time histories of bolometer and Thomson scattering data that tell the story of the MARFE in DIII-D shot 92976. The density near the x-point drops at about 3000 ms, and the density at that location increases shortly thereafter. Radiation near the x-point, as measured by the bolometer spikes soon thereafter, indicating the formation of a core MARFE. By 3500 ms, the MARFE has subsided and left the plasma in L-mode. These data were obtained from the REVIEWPLUS tool on DIII-D's servers.

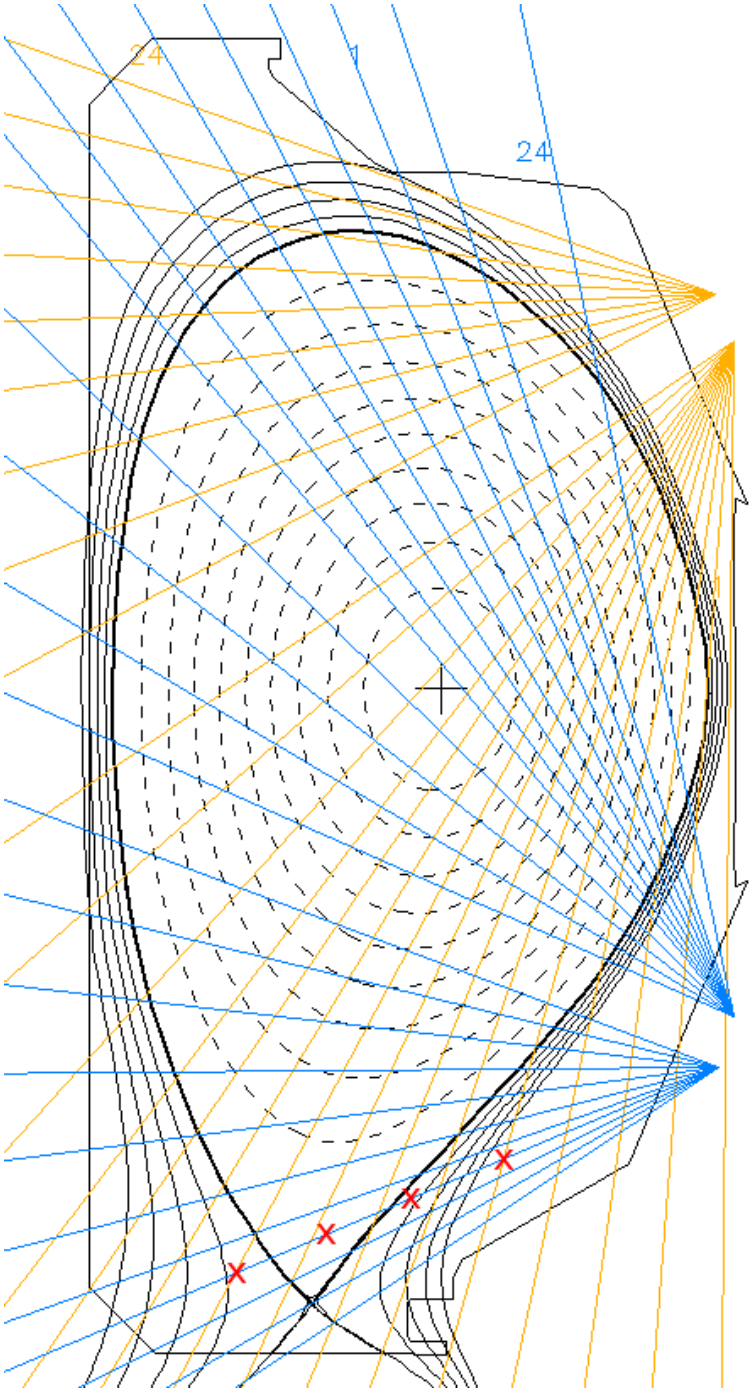

Figure 6.2: A schematic of the bolometer system in DIII-D. The chord used to obtain the data used in the top plot in Figure 6.1 is marked with red 'x's. This figure was generated using DIII-D's EFITVIEWER tool.

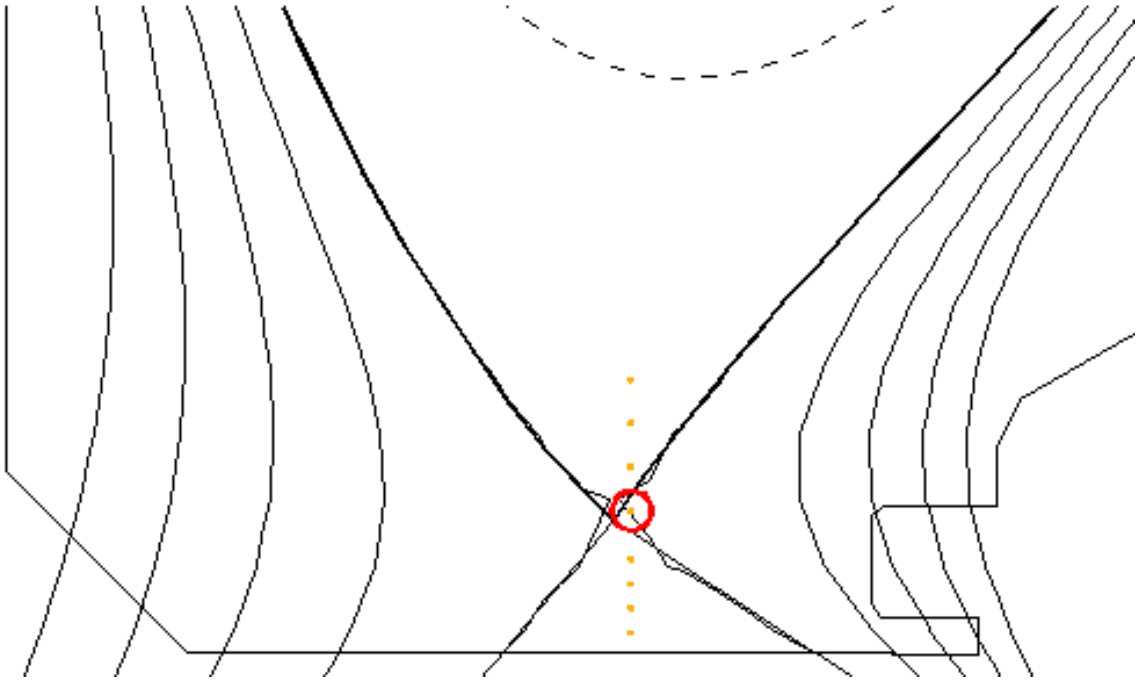

Figure 6.3: The point at which the density and temperature measurements in Figure 6.1 were obtained using DIII-D's Thomson scattering system. This figure was generated using DIII-D's EFITVIEWER tool.

1. The temperature in the vicinity of the x-point begins dropping at 3000 ms, which coincides with an increase in the density beginning at approximately the same time. This is a result of the fact that pressure must remain constant along a flux surface [8], which means that a local decrease in temperature will coincide with a local increase in density.

2. The density in the vicinity of the x-point peaks at about 3100 ms.

3. The MARFE crosses the seperatrix at approximately 3100 ms and is within the confined plasma by around 3250 ms, when the radiation in the path of the bolometer chord spikes.

4. The MARFE radiates strongly for about 200 ms and then dissipates, leaving the plasma in L-mode.

To investigate the timescales on which the core plasma was effected by these events,

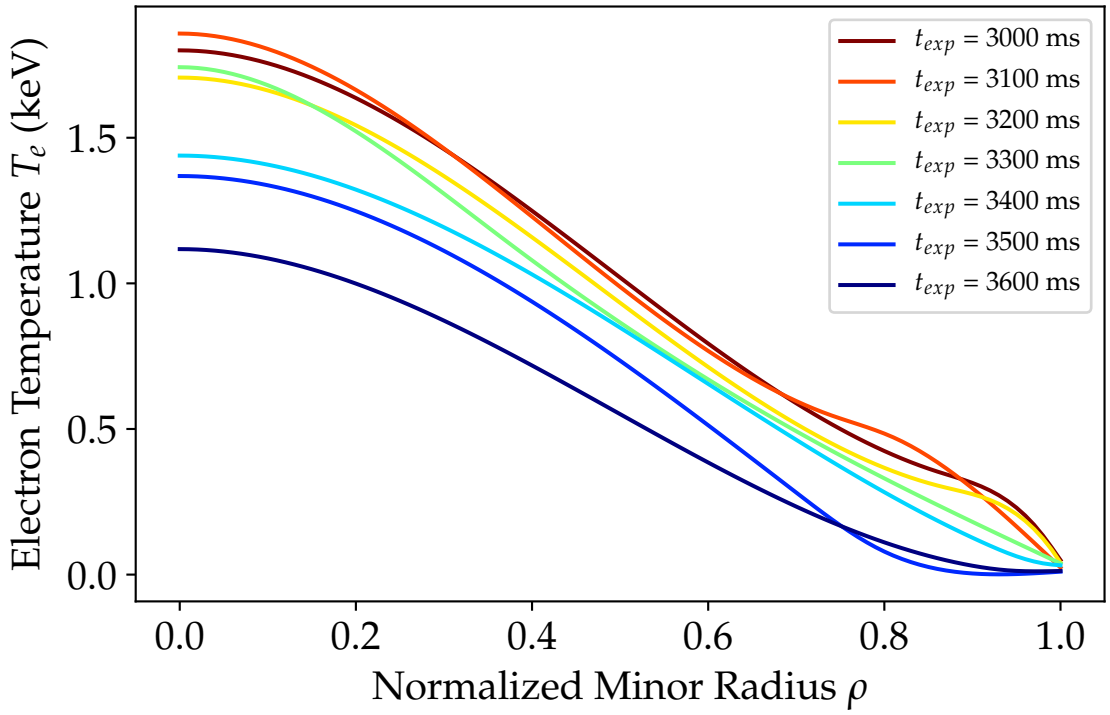

Figure 6.4: The time evolution of the radial electron temperature profile $T_e\,(\rho)$ for DIII-D shot 92976. The MARFE-initiating sequence of events began at ∼3000 ms, the MARFE radiated strongly from about 3200-3400 ms, and the core temperature began significantly dropping about an H-mode confinement time ($\sim$ 0.1 s) after the collapse of the edge pedestal between 3200 and 3300 ms. These data were obtained using the GAPROFILES tool on DIII-D's servers.

full radial temperature profiles were obtained for this shot for several times between 3000 and 3600 ms.

From the perspective of the radial temperature profile, the sequence of events are as follows:

1. The temperature profile remains relatively unchanged from 3000 ms through 3200 ms. The MARFE is still mostly outside the seperatrix during this time.

2. Between 3200 (yellow line) and 3300 ms (green line), we can see that the edge temperature pedestal has collapsed while the temperature in the core has remained unchanged.

3. At 3400 ms (approximately a confinement time after the collapse of the temperature profile in the edge), we see a significant decrease in the core temperature.

4. The edge temperature profile has further collapsed by 3500, however the core temperature is at approximately the same level as it was at 3400 ms.

5. The core temperature experiences another pronounced decrease between 3500 ms and 3600 ms, again, about a confinement time after the second significant reduction in the edge temperature.

From this, we can conclude that significant reductions in core temperature occur after an H-L transition, however those effects are delayed by approximately an H-mode energy confinement time from when the edge temperature profile collapses and the plasma transitions to the L-mode confinement regime.

6.2 MARFE Onset Criteria

Several analyses [65, 66, 67, 68, 69, 70, 71, 72] have attempted to model the criteria for MARFE onset. Most result in a local density limit n_{MARFE} that is a function of impurity and neutral densities, plasma conditions, heating, and other parameters. This analysis uses the model developed by Stacey [8, 73, 74, 75], which has been successful in predicting MARFE onset in at least two tokamak experiments. [76, 77]

The derivation of the MARFE onset criteria [73, 74] begins by obtaining a dispersion relation for the growth of a perturbation in the reduced 3-D (r, $\perp$, $\|$) fluid energy, momentum, and particle balance equations in the edge region of the plasma. The resulting dispersion relation for the growth rate and the requirement that it be negative result in the

the requirement for stability shown in Equation 6.2.

$$n_z\left[\left(\nu+K_1\right)\frac{L_z}{T}-\frac{\partial L_z}{\partial T}\right]-\frac{3}{2}\nu_s\left(\frac{T}{\nu_s}\frac{\partial \nu_s}{\partial T}+1-\nu\right)$$
$$-\frac{E_{ion}}{T}\nu_{ion}\left(\frac{T_{ion}}{\nu_{ion}}\frac{\partial \nu_{ion}}{\partial T}+1-\nu\right)-5T\frac{\partial \nu_n}{\partial T}$$
$$\leq\left[k_r^2+L_T^{-1}\left(\tfrac{-1}{T}-K_1L_n^{-1}\right)\right]\chi_\perp+k_\parallel^2\chi_\parallel \quad (6.2)$$

Here, ν represents the temperature dependence of the radial thermal conductivity, $\chi_\perp \sim T^\nu$, K_1 accounts for the condensation effect and is calculated [72] as

$$K_1=1-\left[\frac{4}{3}\tau_{ii}+\left(\nu_{cx}+\nu_{el}\right)\left(\frac{1}{k_\parallel c_s}\right)^2\right]T\frac{\partial\left(\nu_{ion}-\nu_{rec}\right)}{\partial T} \quad (6.3)$$

Equation 6.2 can be rewritten as a local ion density limit for a given parallel mode number $k_\parallel$. Taking the conservative case of $k_\parallel = 0$, we arrive at the equation for the MARFE density limit shown in Equation 6.4. This equation includes the effects of both cold, uncollided neutrals and thermal, collided neutrals.

$$n_{\mathrm{MARFE}}=\chi_\perp\left[\nu L_T^{-2}+\left(C^{(2)}-1\right)L_T^{-1}L_n^{-1}\right]/$$
$$\left\{f_z\left[\left(\nu+1-C^{(2)}\right)\frac{L_z}{T}-\frac{\partial L_z}{\partial T}\right]+\right.$$
$$f_0\frac{E_{ion}}{T}\left\langle\sigma v\right\rangle_{ion}\left(\nu-\frac{T}{\left\langle\sigma v\right\rangle_{ion}}\frac{\partial\left\langle\sigma v\right\rangle_{ion}}{\partial T}\right)$$
$$\left.+f_0^c\frac{3}{2}\left(\left\langle\sigma v\right\rangle_{cx}+\left\langle\sigma v\right\rangle_{el}\right)\left(\nu-1-T\frac{\partial\left(\left\langle\sigma v\right\rangle_{cx}+\left\langle\sigma v\right\rangle_{el}\right)/\partial T}{\left\langle\sigma v\right\rangle_{cx}+\left\langle\sigma v\right\rangle_{el}}\right)\right\} \quad (6.4)$$

In Equation 6.4, $\chi_\perp$ is the radial heat conduction coefficient. L_n and L_T are the local ion density and temperature gradient scale lengths, respectively, and are calculated as $L_{\mathrm{X}} =$

$\mathrm{X}/\left(-d\mathrm{X}/dr\right)$, where X is the quantity of interest, such as density or temperature. Spatial gradients in the edge of the plasma can be challenging to obtain due to uncertainty in measured data, as well as the fact that neither densities and temperatures, nor their gradients are poloidally uniform on a flux surface. In GT3, spatial gradients of the quantity X in two-dimensional R, Z geometry are obtained by first calculating $d\mathrm{X}/d\psi$ (where X is assumed constant on a flux surface) at several points along a line going from the magnetic axis to the seperatrix at the outboard mid-plane based on fits of experimental data. That ψ-derivative is then multiplied by $d\psi/dr\,(R,Z)$, as shown below.

$$\frac{d\mathrm{X}}{dr} = -\frac{d\mathrm{X}\left(\psi\right)}{d\psi}\left|\frac{d\psi\left(R,Z\right)}{dr}\right| = -\frac{d\mathrm{X}}{d\psi}\left(\left|\frac{\partial\psi}{\partial R}\right| + \left|\frac{\partial\psi}{\partial Z}\right|\right) \tag{6.5}$$

$C^{(2)}$ is a fitted parameter that arises from the thermal friction along the field lines.

$$C^{(2)} = C_e^{(2)} - z_0 C_i^{(2)} \tag{6.6}$$

where

$$C_e^{(2)} = 1.5\left(1 - \frac{0.6934}{1.3167^{z_{\mathrm{eff}}}}\right) \tag{6.7}$$

and

$$C_i^{(2)} = \frac{\left(1+0.24z_0\right)\left(1+0.93z_0\right)}{\left(1+2.65z_0\right)\left(1+0.285z_0\right)} \tag{6.8}$$

are fitted parameters, and z_{eff} and z_0 have their usual definitions, i.e.

$$z_{\mathrm{eff}} \equiv \sum_j^{\mathrm{ions}} \frac{n_j z_j^2}{n_e} \tag{6.9}$$

$$z_0 \equiv \sum_z^{\mathrm{imp}} \frac{n_z z_z^2}{n_i} \tag{6.10}$$

In Equation 6.4, ν represents the temperature dependence of $\chi_\perp \precsim T^\nu$. Various transport theories give values for ν ranging from $3/2$ to $7/2$. This analysis uses $\nu = 5/2$ unless

otherwise stated. L_z and $\partial L_z/\partial T$ are calculated using ADPAK data, as described in Chapter 4. Ionization, electron scattering, and charge exchange cross sections ($\langle\sigma v\rangle_{ion}$, $\langle\sigma v\rangle_{el}$, and $\langle\sigma v\rangle_{cx}$, respectively) can be obtained from any of a number of different cross section libraries. Unless otherwise stated, values reported in this thesis were obtained using the Thomas-Stacey cross section libraries [78], which have been implemented in GT3.

In addition to the density limit of Equation 6.4, it is also useful to define a "MARFE Index," as the local ion density n_i divided by n_{MARFE}. MARFE onset is predicted for $\mathrm{MI} > 1$.

$$\mathrm{MI} \equiv \frac{n_i}{n_{\mathrm{MARFE}}} \tag{6.11}$$

6.3 Evaluation of MARFE Onset Criteria in ITER

Equations 6.4 and 6.11 were evaluated for a realistic model of an ITER shot, with density and temperature profiles shown in Figure 6.5 and with ν = 5/2. These profiles are scaled versions of DIII-D profiles, which were used to provide a more realistic edge profile than the radial profiles used in other chapters.

For these calculations, χ was modeled using the Bohm diffusion approximation, which is frequently used to model radial transport in the SOL [8]. It was also found to work well when validating the MARFE onset model against previous MARFE calculations as a part of this analysis. Impurity radiation emissivity data and other quantities were calculated as previously described.

Neutrals data were obtained from the NEUTPY neutrals transport code described in Appendix C and the GT3 tokamak analytics code described in Appendix B. The resulting neutral densities are shown in Figure 6.6. The neutrals model depends on densities and temperatures in the scrape-off layer (SOL), including those directly in front of the divertor strike points, which are responsible for most of the neutral source into the plasma chamber. Densities and temperatures in the SOL and HALO regions were obtained using experimental flux surface geometry, a relatively simple strip model of the SOL, the assumption of

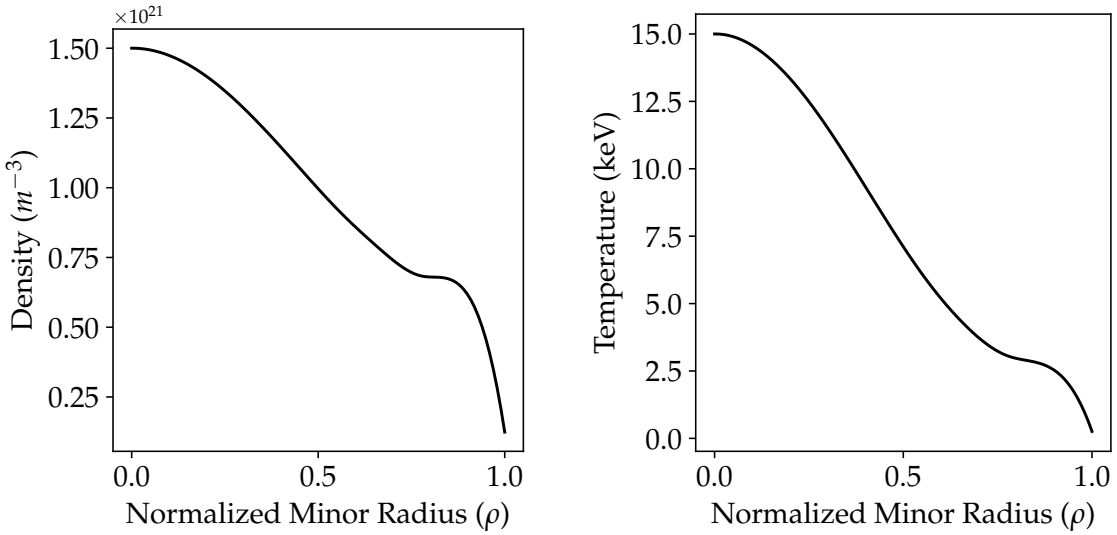

(a) Radial density profile for ions and electrons

(b) Radial temperature profile for ions and electrons

Figure 6.5: Density and Temperature profiles used in the ITER neutrals calculation.

Table 6.1: Selected MARFE model parameters.

$n_{i,e,sep}$	1.24×10^{20} m^{-3}	$T_{i,e,sep}$	0.26 keV
$n_{n,xpt}$	1.27×10^{14} m^{-3}	$L_{n,xpt}^{-1}$	0.94
$n_{n,obmp}$	5.46×10^{15} m^{-3}	$L_{T,xpt}^{-1}$	2.09
nf_{xpt}	1.02×10^{-6}	$L_{n,obmp}^{-1}$	41.5
nf_{obmp}	4.40×10^{-5}	$L_{T,obmp}^{-1}$	91.7

Bohm diffusion in the SOL, and a two-point divertor model. Reasonable minimum densities and temperatures were imposed on the SOL and Halo regions. The SOL model used for these calculations is discussed in greater detail in Appendix B.4. Some of the relevant parameters for the MARFE onset calculation are shown in Table 6.1.

To get a sense of the dependence of the MARFE onset criteria on neutral density and impurity concentration, the MI was calculated for ITER using the GT3 code for a range of x-point neutral densities and tungsten impurity fractions. The results of these calculations are shown in Table 6.2.

The data suggest that the MARFE onset criteria is more sensitive to impurity concentration than to neutral concentration. They also suggest that there is an impurity concentration

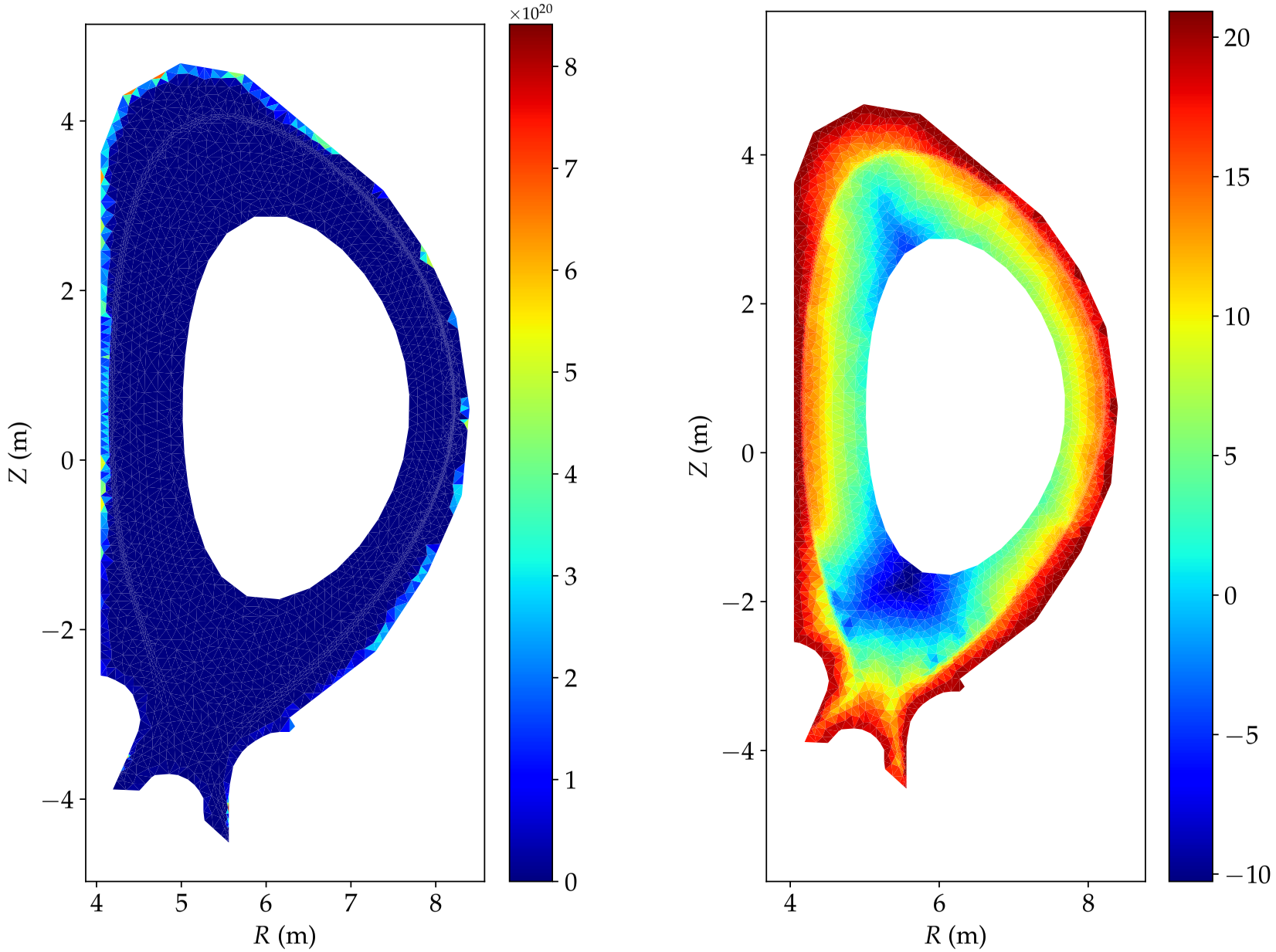

(a) Linear color scale. The values in the color scale are the exponent, i.e. 10^{15} m^{-3}, etc.

(b) Logarithmic color scale

Figure 6.6: Neutral densities in ITER calculated using the GT3 and NEUTPY codes. Units are m^{-3}.

Table 6.2: Sensitivity Study of MARFE Onset in ITER. MARFE indices Calculated for Range of Neutral Density and Tungsten Impurity Fraction. Values in the table are calculated MARFE indices.

	$f_{W,\mathrm{xpt}}$			
n_n	1×10^{-6}	1×10^{-5}	1×10^{-4}	1×10^{-3}
$1.0 \times n_{n,\mathrm{neutpy}}$	0.014	0.086	0.806	8.008
$2.0 \times n_{n,\mathrm{neutpy}}$	0.019	0.091	0.811	8.013
$3.0 \times n_{n,\mathrm{neutpy}}$	0.024	0.097	0.817	8.018

* n_n in the table refers to the x-point neutral density used to calculate MI. $n_{n,\mathrm{neutpy}}$ is the x-point neutral density calculated by Neutpy. $f_{W,\mathrm{xpt}}$ is the tungsten impurity fraction.

threshold, above which MARFEs become more likely. This threshold was calculated for each of several impurity species of interest for ITER.

The results, which are shown in Figure 6.7, suggest that a neon concentration of around 5% would be needed for MARFE onset, whereas about 1/100th that amount of argon would be necessary. Moving to higher-z elements like Krypton doesn't require significantly lower impurity fractions for MARFE onset, so neon and argon are the most attractive candidates for any attempts to deliberately trigger a MARFE. The selection of the best mix of these impurity species would likely depend on the capabilities of the MGI system, SPI system, the impurity transport characteristics of the plasma, and the concentration of tungsten in that region of the plasma. An analysis similar to this one would undoubtedly need to be conducted once we have MARFE and impurity data from the early stages of ITER's operation.

6.4 The Temperature Dependence of the MARFE Onset Criteria

The temperature dependence of the MARFE onset criteria given in Equation 6.4 is hardly obvious, and the complex temperature dependences of L_z and the various cross sections

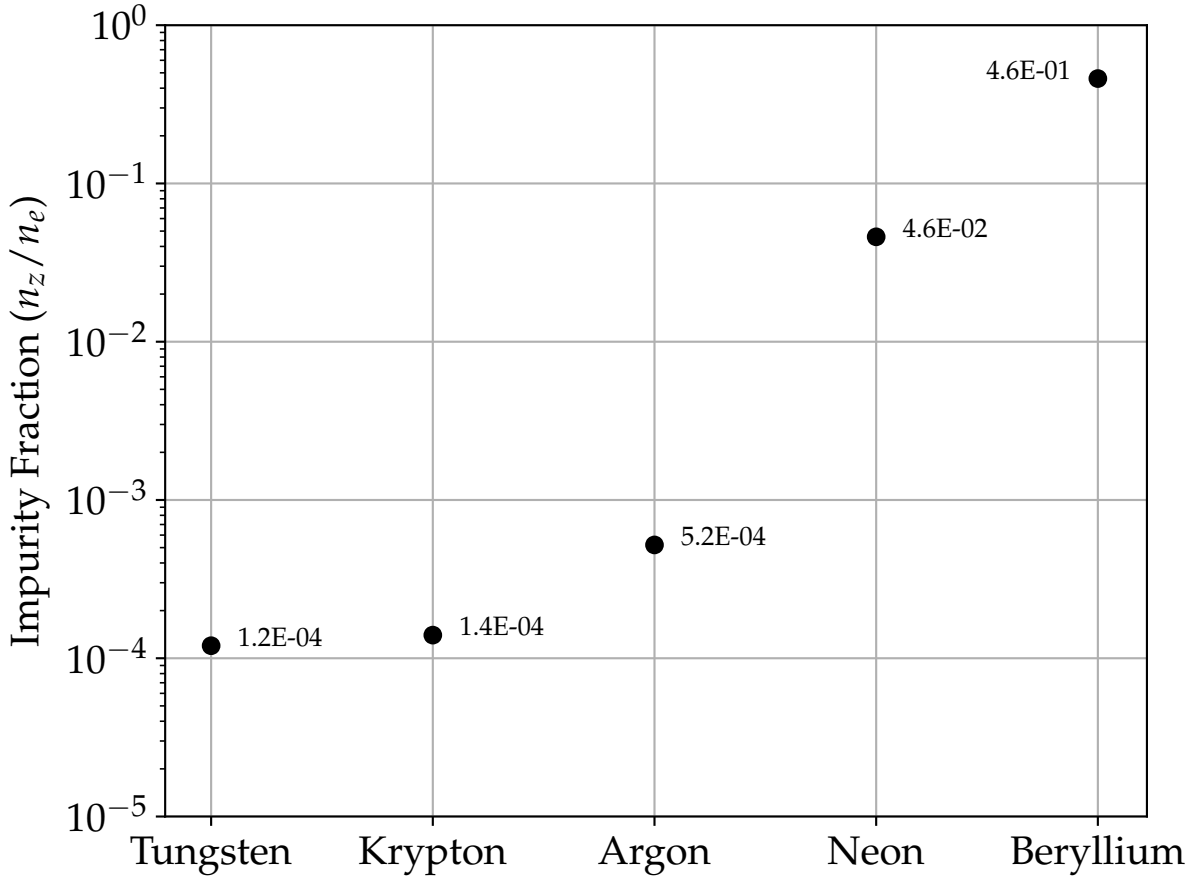

Figure 6.7: The impurity fractions for several ITER-relevant impurity species that result in a prediction of MARFE onset in ITER using the GT3 code. The Neutpy-calculated x-point neutral density was used.

only obscure it further. If it were the case that the MI increased with increasing temperature in a certain temperature range, then it is possible that a temperature increase could directly result in increased likelihood of a MARFE occurring.

The equation for the MARFE index was evaluated over the relevant temperature range in DIII-D for several values of the neutral fraction f_0 (the fraction of uncollided neutrals, f_0^c, was set to zero for this part of the analysis) and a carbon impurity fraction $f_z = 1.5\,\%$ was used. $\chi_\perp$ was modeled using the Bohm diffusion approximation [8]

$$\chi_\perp \approx \frac{5}{32}\frac{T}{eB} \tag{6.12}$$

The results are shown in Figure 6.8. It should be noted that the calculated magnitude of MI is less important in this analysis than the way in which it changes with temperature. There are many other terms in the equation that can influence the MI up or down, such as changes in density or temperature gradients, radial transport parameters, etc.

This interesting result suggests that it is possible for the MARFE index to have a positive temperature dependence, which would be necessary for a MARFE to be useful as a passive, albeit delayed (by the confinement time), negative feedback mechanism. This region of positive temperature dependence, however, occurs only within a narrow temperature range, and only for very low neutral fractions in DIII-D.

This analysis was repeated for ITER over a range of neutral fractions, as well as over a range of tungsten impurity fractions to evaluate the sensitivity of MARFE onset in ITER to both. The results are shown in Figure 6.9.

As can be seen in Figure 6.9d, especially subfigures (c) and (d), it is possible to have a positive temperature dependence of the MARFE onset criteria at around 100 eV in ITER at low neutral fraction and high impurity fraction. Although this temperature dependence is interesting and may warrant further exploration, it seems unlikely that neutral fractions would be low enough and impurity fractions high enough (without causing plenty of other

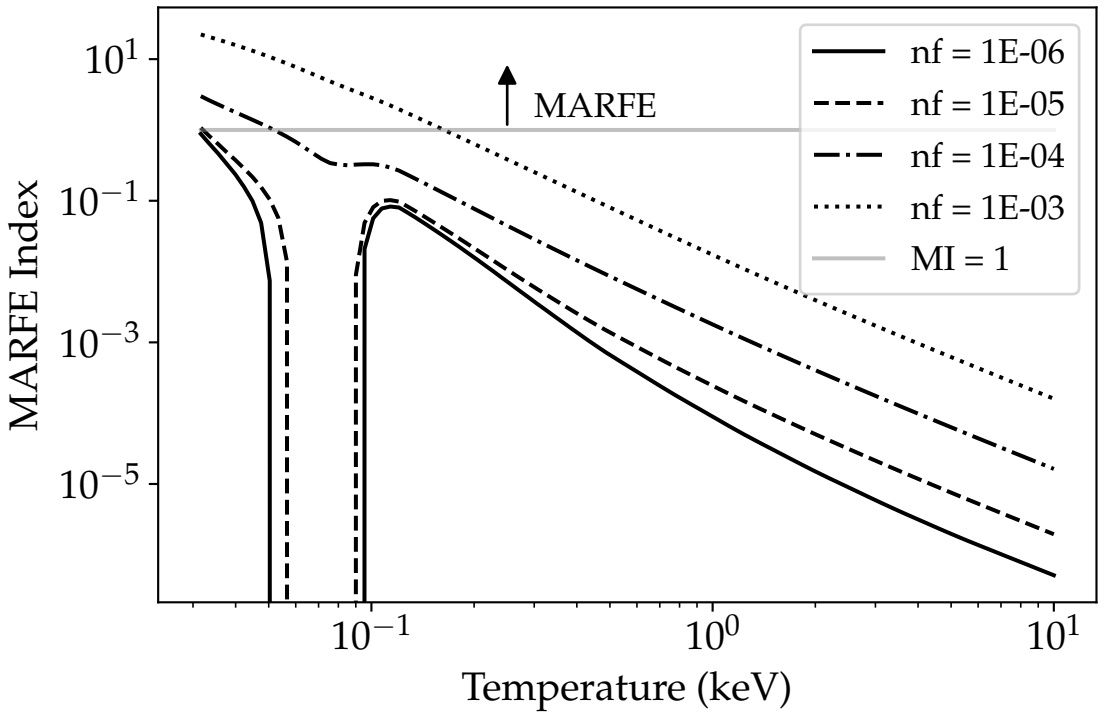

Figure 6.8: A plot of the temperature dependence of the MARFE Index for several neutral fractions (nf) in DIII-D. The MARFE onset criteria may have a positive temperature dependence within a fairly narrow temperature range, but only for very low neutral fractions.

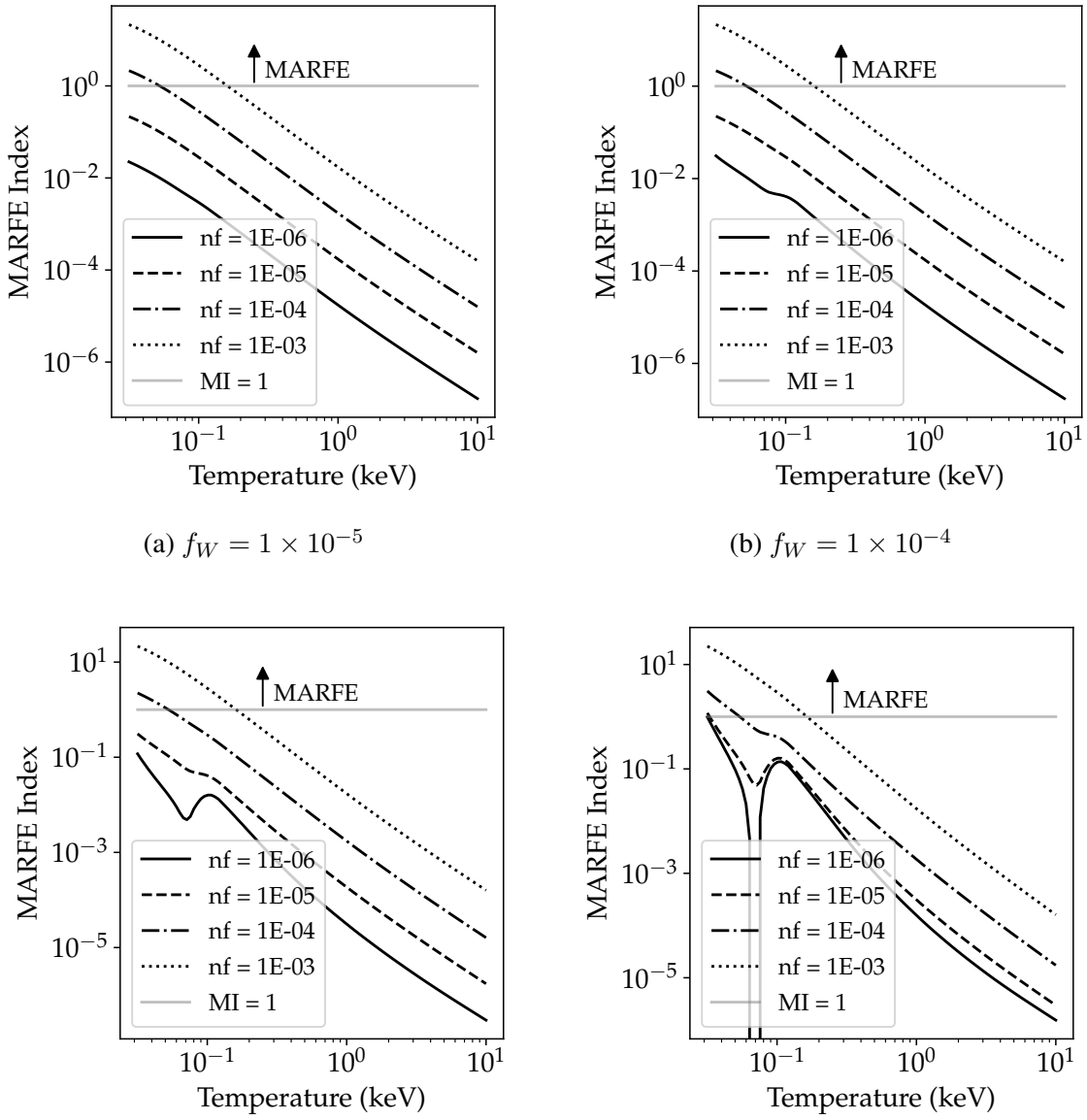

(a) $f_W = 1 \times 10^{-5}$

(b) $f_W = 1 \times 10^{-4}$

(c) $f_W = 1 \times 10^{-3}$

(d) $f_W = 1 \times 10^{-2}$

Figure 6.9: Sensitivity study of the MARFE onset criteria in ITER to temperature, neutral fraction, and impurity fraction. A positive temperature dependence is possible when neutral fractions are very low and tungsten fractions are very high. Otherwise, MARFE onset becomes less likely with increasing temperature.

problems) for this to be likely to occur in ITER. For more realistic situations, MARFEs will probably become less likely with increasing edge temperature in ITER.

6.5 MARFE Conclusions

This analysis should not be viewed as a comprehensive investigation of MARFEs in ITER, since the MARFE onset criteria is sensitive to many quantities that are beyond the scope of GT3 and most other codes to reliably predict for ITER. These include density and temperature gradients, density and temperature poloidal asymmetries, radial and parallel ion transport in the SOL, and heat and particle flux to the divertor. Rather, this analysis seeks to demonstrate the calculation of MARFE onset in ITER and evaluate the likelihood that MARFE's could be passively or actively triggered for burn control purposes.

The analysis suggests that impurity gas puffing in the ITER divertor is the most promising way of triggering a MARFE, as the MARFE onset criteria appears to be more sensitive to changes in impurity concentration than neutral hydrogen fraction. Depending on the tungsten concentration in the vicinity of the x-point, it is likely that injecting neon or argon could create the conditions that would result in a MARFE. The slow timescales on which a MARFE could effect core conditions, however, leads to the conclusion that MARFEs are unlikely to feature prominently in either a passive or active burn control strategy in ITER.

CHAPTER 7
TOWARD A MULTI-NODAL TOKAMAK DYNAMICS MODEL FOR BURN CONTROL

This thesis has shown that although fusion α-heating in a tokamak occurs primarily in the inner core region, it cannot be modeled in isolation. EC radiation from the core during a power excursion cools the core and heats the edge, which has implications for radiative power losses in the edge. The power increase in a power excursion could obviously have severe implications for heat and particle flux in the divertor, although on a much longer timescale than other aspects of a thermal power excursion. MARFEs, whether unintentional or used as part of a burn control strategy, are created by conditions in the divertor and edge plasmas and affect the core on different timescales still.

A model that accounts for these and other phenomena is vital to properly understanding the thermal stability of a burning plasma and to the design of effective control mechanisms. It is difficult to account for these phenomena in a 0-D model, such as the one described in Chapter 2. The purpose of this chapter is to provide the framework for a multi-nodal dynamics model that accounts for these effects and that could be used in future active control algorithms and burning plasma simulations. We will first develop the model without considering delays in responding to core conditions, and then show how to include those delays in the model. To demonstrate the model using experimental data is reserved for future work, however opportunities to tune the model using future ITER data are discussed throughout this chapter.

7.1 Model Overview and Node Selection

The relationship between various phenomena in a tokamak can be explored through a variety of 1-D and 2-D plasma fluid codes and other analytical techniques. Such approaches,

however, are likely not fast enough for active control decisions that must be made in near real-time by control algorithms. Furthermore, such models may provide more information than is needed to make control decisions.

Instead, the conditions in a few key regions can be modeled as a series of coupled, 0-D dynamics equations. This kind of nodal dynamics model has been used recently to model the neutronically coupled fission reactor cores of a fusion-fission hybrid reactor [79]. This analysis proposes the following nodes, which are illustrated in Figure 7.1:

1. **Inner core**: The inner core is where most fusion power will be generated and will, therefore, be the primary focus of burn control strategies

2. **Outer core / edge**: Many active control strategies will be limited to effecting conditions in this region. Furthermore, temperature and density increases in this region could have important consequences for disruptions and MHD stability.

3. **Scrape-off layer (SOL)**: Although a thermal power excursion is unlikely to occur in the low-density scrape-off layer, it is this region that couples the core and edge region to the divertor, which is a region of significant interest.

4. **Divertor**: Conditions in the divertor could effect the power balance in the core plasma through a variety of mechanisms. Changes in fusion power in the core and edge regions will obviously have significant consequences in the divertor.

The ion densities and temperatures in the private flux region (PFR) are not treated using a node, however they could be in the future if it was found necessary to do so.

In addition to modeling each region of the plasma separately, it will also be important to model each ion species separately, rather than assuming that $n_D = n_T$, as is often done. The local fusion rate will be determined by the smaller of the two main ion densities. Each species has a different set of sources and, in the case of IOL in the edge region, somewhat different sinks as well, due to differences in the charge-to-mass ratios of the ions.

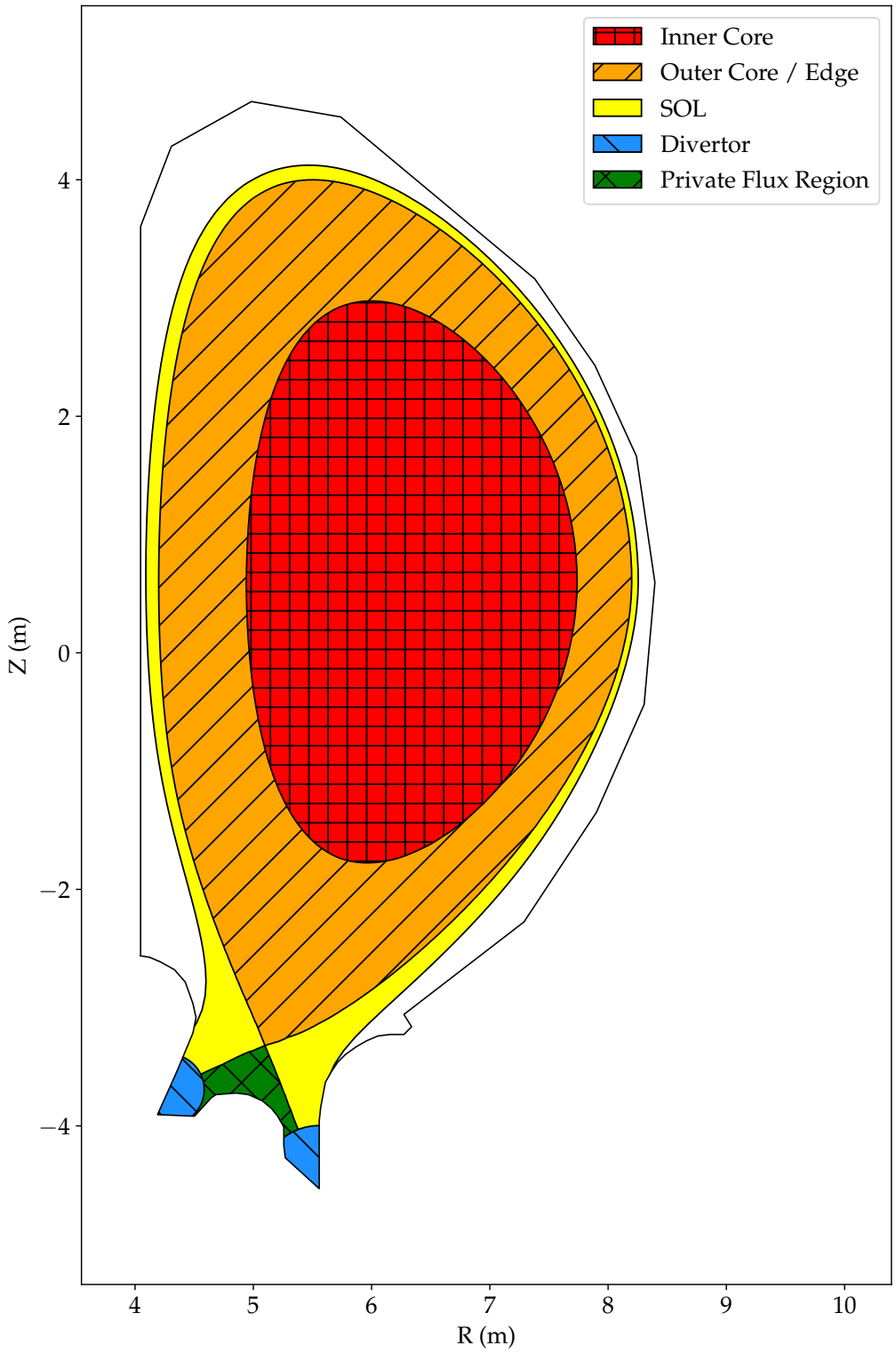

Figure 7.1: ITER diagram showing the regions proposed for the multi-nodal dynamics model.

7.2 Node 1: Inner Core

The inner core ($\rho \leq \rho_{\mathrm{IC}} \sim 0.5$) is where most fusion heating will take place, as it will typically have the highest ion densities and temperatures. Modeling the dynamics and timescales of this region will be especially important in the event of a thermal power excursion.

7.2.1 Particle Sources in the Inner Core

Deuterium is deposited in the inner core from two sources: neutral beam injection (NBI) and shattered pellet injection (SPI). The particle source density from NBI can be written as

$$S_{\mathrm{D,NBI}} = \frac{1}{V_{\mathrm{IC}}} \sum_{k} \frac{F_{k,\mathrm{D}}}{E_k} \int_{\mathrm{IC}} \frac{dP_k}{d\rho} d\rho \tag{7.1}$$

where V_{IC} is the volume of the inner core, k indicates the beam component, E_k is the energy of that beam component ($\sim$1 MeV for atomic deuterium in ITER, $\sim$500 keV for atoms accelerated as molecular D_2, etc), $F_{k,\mathrm{D}}$ is the fraction of beam power from deuterium (a small amount of molecular protium will be delivered by ITER's beams) [80], and $dP_k/d\rho$ is the total radial power deposition profile, where it is assumed that any beam IOL has already been accounted for.

$$S_{\mathrm{D,NBI}}\left(t\right) = \frac{1}{V_{\mathrm{IC}}} \sum_{k} \frac{F_{k,\mathrm{D}}}{E_k} \int_{\mathrm{IC}} \frac{\partial P_k\left(\rho\right)}{\partial \rho} d\rho \tag{7.2}$$

The SPI particle source for any particle species x can be modeled in a similar way. The radial deposition profile is determined by the pellet ablation rate, which is ultimately a complex function of pellet composition, shard size, plasma density and temperature profiles, and the trajectory through the plasma. The effects of those parameters on the pellet's

radial deposition profile is an area of active research [81, 82, 42].

$$S_{\mathrm{x,SPI}}(t) = \frac{1}{V_{\mathrm{IC}}} F_{\mathrm{p},x} \int_{\mathrm{IC}} \frac{\partial S_{\mathrm{p}}(\rho)}{\partial \rho} d\rho \tag{7.3}$$

Here, x is the ion species, $F_{\mathrm{p},x}$ is the relative fraction of species x in the pellet, and $dS_{\mathrm{p}}/d\rho$ is the total radial SPI particle deposition profile.

7.2.2 Particle Sinks in the Inner Core

Particles are lost from the inner core through three primary mechanisms: being consumed in fusion, "diffusive" radial transport, and direct ion orbit loss/transport to other flux surfaces or out of the plasma. Ion orbit loss of thermalized ions will be insignificant in the inner core, however in some situations, fast α particles could be lost. The volumetric loss rate of particles of species x from the inner core can be estimated as

$$S_{x,\mathrm{IOL}}(t) \approx \frac{-F_{x,\mathrm{orb}}(\rho_{\mathrm{IC}})}{V_{\mathrm{IC}} \tau_{P,x}^{\mathrm{IC}}} \int_{\mathrm{IC}} n(\rho) \frac{dV}{d\rho} d\rho \tag{7.4}$$

Here, $\tau_{P,x}^{\mathrm{IC}}$ is the time it takes a particle to go from the somewhere near the magnetic axis to the ρ value we select as the boundary between the inner and outer cores. A reasonable estimate of this value is $\tau_{P,x}^{\mathrm{IC}} \approx \rho_{\mathrm{IC}} \tau_E^{98}$, which will be ~ 2 seconds in ITER. Future improvements in IOL theory may result in a different form for the rate of particle loss from IOL from a region of plasma.

The volumetric particle loss from diffusive radial particle transport can be modeled as

$$S_{x,\mathrm{dif}}^{\mathrm{IC}}(t) = \frac{-n_x^{\mathrm{IC}}(t)}{\tau_{P,x}^{\mathrm{IC}}} - S_{x,\mathrm{IOL}} \tag{7.5}$$

where x is the species of interest and we have accounted for the fact that particles lost to IOL are not available to diffuse into the next region. As mentioned previously, $S_{x,\mathrm{IOL}}$ will be negligible in the inner core for thermalized species and, depending on the plasma current

and the location of ρ_{IC}, may be negligible for fast α particles as well.

Because of the possibility of conditions in the outer core and edge effective transport characteristics in the inner core (as is the case in an H-L transition), it may also be useful to include a term $G_{P,\mathrm{IC}}$ that depends on edge characteristics.

$$S_{x,\mathrm{dif}}^{\mathrm{IC}}\left(t\right)=\frac{-n_{x}^{\mathrm{IC}}\left(t\right)}{\tau_{P,x}^{\mathrm{IC}}}-S_{x,\mathrm{IOL}}+G_{P,\mathrm{IC}}\left(t\right) \tag{7.6}$$

A simple form of G could be a "switch" that modifies transport losses when a condition is met in the edge. A reasonable form for G (still neglecting delayed effects) for accounting for the effects of an H–L transition on the inner core might look like

$$G_{P,\mathrm{IC}}\left(t\right)\propto H\left(1-\frac{3n_{i}^{\mathrm{OC}}\left(t\right)T_{i}^{\mathrm{OC}}\left(t\right)V_{\mathrm{OC}}}{2\tau_{E,i}^{\mathrm{OC}}A_{\mathrm{sep}}P_{LH}\left(t\right)}\right) \tag{7.7}$$

where H is the Heaviside function, A_{sep} is the surface area of the last closed flux surface, and P_{LH} is the H-mode threshold power requirement discussed in Chapter 6. G could also be constructed as a more robust tuning parameter based on regressions of timeseries data or the results of machine learning algorithms. As discussed in Chapter 4, on-axis ECCD may play a significant role in determining impurity transport characteristics in and near the inner core. Another G-like term could be included in the future to account for the potentially significant dependence of impurity particle transport on ECCD.

The rate that deuterium and tritium are consumed in fusion is a function of the smallest of the two species' densities and the local ion temperature (assumed to be the same for deuterium and tritium). This volumetric sink of particles can be written as

$$S_{\mathrm{D,fus}}^{\mathrm{IC}}\left(t\right)=S_{\mathrm{T,fus}}^{\mathrm{IC}}\left(t\right)=-\frac{1}{4}d\left[\min\left\{n_{D}^{\mathrm{IC}}\left(t\right),n_{T}^{\mathrm{IC}}\left(t\right)\right\}\right]^{2}\left\langle\sigma v\right\rangle_{f}\left(T_{\mathrm{IC}}\left(t\right)\right) \tag{7.8}$$

where $d=n_{T}n_{D}/n_{e}^{2}$ accounts for the effects of fuel dilution by impurities. Similarly, the

source of α particles is

$$S^{\mathrm{IC}}_{\alpha,\mathrm{fus}}(t) = \frac{1}{4} d \left[\min\left\{n^{\mathrm{IC}}_{D}(t), n^{\mathrm{IC}}_{T}(t)\right\}\right]^{2} \langle\sigma v\rangle_{f}\left(T_{\mathrm{IC}}(t)\right) + S_{\alpha,\mathrm{IOL}} \tag{7.9}$$

The foregoing analysis allows us to write the differential equation for the time dependence of the deuterium, tritium, and α particle densities in the inner core as

$$\frac{dn^{\mathrm{IC}}_{D}(t)}{dt} = S^{\mathrm{IC}}_{\mathrm{D,NBI}}(t) + S^{\mathrm{IC}}_{\mathrm{D,SPI}}(t) + S^{\mathrm{IC}}_{\mathrm{D,fus}}(t) + S^{\mathrm{IC}}_{D,\mathrm{dif}}(t) \tag{7.10}$$

$$\frac{dn^{\mathrm{IC}}_{T}(t)}{dt} = S^{\mathrm{IC}}_{\mathrm{T,SPI}}(t) + S^{\mathrm{IC}}_{\mathrm{T,fus}}(t) + S^{\mathrm{IC}}_{T,\mathrm{dif}}(t) \tag{7.11}$$

$$\frac{dn^{\mathrm{IC}}_{\alpha}(t)}{dt} = S^{\mathrm{IC}}_{\alpha,\mathrm{SPI}}(t) + S^{\mathrm{IC}}_{\alpha,\mathrm{fus}}(t) + S^{\mathrm{IC}}_{\alpha,\mathrm{dif}}(t) + S^{\mathrm{IC}}_{\alpha,\mathrm{IOL}}(t) \tag{7.12}$$

For other impurity species, the equation is simply

$$\frac{dn^{\mathrm{IC}}_{x}(t)}{dt} = S^{\mathrm{IC}}_{\mathrm{x,SPI}}(t) + S^{\mathrm{IC}}_{x,\mathrm{dif}}(t) \tag{7.13}$$

The radially inward transport of high-z impurities could be modeled using a negative confinement time and an appropriate selection of G in the calculation of $S^{\mathrm{IC}}_{x,\mathrm{dif}}(t)$.

7.2.3 Power Sources in the Inner Core

The four most significant power sources in the inner core are fusion heating power, neutral beam heating power, auxiliary RF heating power, and intrinsic RF heating power (reabsorbed EC power generated within the plasma). The fusion heating power density for a non-α species x in the inner core is calculated as

$$P^{\mathrm{IC}}_{\mathrm{x,fus}}(t) = -\frac{1}{4} d \left[\min\left\{n^{\mathrm{IC}}_{D}(t), n^{\mathrm{IC}}_{T}(t)\right\}\right]^{2} \langle\sigma v\rangle_{f}\left(T_{\mathrm{IC}}(t)\right) U_{\alpha x} F^{\mathrm{IC}}_{\mathrm{IOL}} \tag{7.14}$$

where $U_{\alpha x}$ is the amount of the 3.5 MeV α particle's energy that is given directly to that species. In practice, $U_{\alpha e}/U_{\alpha}$ will be very close to 1 and $U_{\alpha\{D,T\}}/U_{\alpha}$ will be close to zero. It should be noted that the energy retained by the thermalized α particle will be less than 1% of its original energy (20 keV / 3.5 MeV $\sim$ 0.5%). $F_{\mathrm{IOL}}^{\mathrm{IC}}$ (not to be confused with F_{orb}) is the fraction of fast α particles that are not lost to IOL within the inner core, and can be estimated as

$$F_{\mathrm{IOL}}^{\mathrm{IC}} \approx 1 - \int_{\mathrm{IC}} \left[\min\left\{n_D^{\mathrm{IC}}\left(\rho,t\right), n_T^{\mathrm{IC}}\left(\rho,t\right)\right\}\right]^2 \left\langle\sigma v\right\rangle_f \left(T_i\left(\rho,t\right)\right) \frac{dV\left(\rho\right)}{d\rho} \frac{dE_{\mathrm{orb}}\left(\rho\right)}{d\rho} d\rho \quad (7.15)$$

By analogy with Equation 7.54, we can write the power density source from the neutral beams for a species x as

$$P_{\mathrm{x,NBI}}^{\mathrm{IC}}\left(t\right) = \frac{1}{V_{\mathrm{IC}}} \sum_k \frac{U_{k,x}}{E_k} \int_{\mathrm{IC}} \frac{\partial P_k\left(\rho\right)}{\partial \rho} d\rho \quad (7.16)$$

where $U_{k,x}$ is the amount of the energy of a beam particle of species k that will be given to species x as it thermalizes. Here, it is assumed that any IOL of beam ions has already been accounted for in the radial deposition profile.

The calculation of the power absorbed in the inner core from auxiliary RF heating sources is complex and requires specialized transport calculations. Here, we will assume that the power deposited to each species and the radial deposition profile are already known from other codes and represent it as

$$P_{\mathrm{x,RF}}^{\mathrm{IC}}\left(t\right) = \frac{F_{x,\mathrm{RF}}^{\mathrm{IC}}}{V_{\mathrm{IC}}} \int_{\mathrm{IC}} \frac{\partial P_{\mathrm{RF}}\left(\rho\right)}{\partial \rho} d\rho \quad (7.17)$$

where $F_{x,\mathrm{RF}}^{\mathrm{IC}}$ is the fraction of the deposited auxiliary heating power given to species x and $dP_{\mathrm{RF}}/d\rho$ is the total radial power deposition profile from auxiliary RF heating.

The intrinsic radiative heating source is a result of EC radiation that is generated within the plasma and reabsorbed in the inner core. Since it will likely be the case that the net

emission and absorption will already be accounted for by EC radiation transport codes and that this will be a net sink in the inner core, we will model it as a sink in the next section.

7.2.4 Power Sinks in the Inner Core

The primary power sinks from the inner core are EC radiation, impurity and bremsstrahlung radiation, and radial diffusive transport. EC radiative power losses were discussed in great detail in Chapter 3. The power density sink from EC radiation in the inner core can be written as

$$P_{\mathrm{EC}}^{\mathrm{IC}}(t) = \frac{1}{V_{\mathrm{IC}}} \int_{\mathrm{IC}} \frac{\partial P_{\mathrm{EC}}(\rho)}{\partial V} \frac{dV}{d\rho} d\rho \tag{7.18}$$

where $\partial P_{\mathrm{EC}}/\partial V$ is the volumetric power deposition density profile. Based on the calculations cited in Chapter 3, this quantity will likely be negative for $\rho \lesssim 0.6$ and positive elsewhere. $dV/d\rho$ can be obtained numerically from flux surface reconstructions or approximated for an elliptical plasma by

$$\frac{dV}{d\rho} = 4\pi^2 \kappa R_0 a^2 \rho \tag{7.19}$$

The power density sink from impurity and bremsstrahlung radiation in the inner core can be calculated from ADPAK data, as described in Chapter 4. Alternatively, it can be estimated using Equation 4.4, as shown below.

$$P_{\mathrm{imp}}^{\mathrm{IC}}(t) \left(\frac{MW}{m^3} \right) \approx \sum_k \left(1 + 0.3 T_e^{\mathrm{IC}}(t)\right) \times 10^{-43} n_e^{\mathrm{IC}}(t)\, n_k(t)\, z_k^{\left(3.7 - 0.33 \ln\left[T_e^{\mathrm{IC}}(t)\right]\right)} \tag{7.20}$$

where k is the impurity species.

The radial diffusive energy transport can be modeled using a time constant $\tau_{e,x}^{\mathrm{IC}}$ as

$$P_{x,\mathrm{dif}}^{\mathrm{IC}}(t) = \frac{-3}{2} \frac{n_x^{\mathrm{IC}}(t)\, T_x^{\mathrm{IC}}(t)}{\tau_{E,x}^{\mathrm{IC}}} - P_{x,\mathrm{IOL}}^{\mathrm{IC}}(t) + G_{E,\mathrm{IC}}(t) \tag{7.21}$$

where

$$P_{x,\mathrm{IOL}}^{\mathrm{IC}}(t) \approx \frac{-E_{x,\mathrm{orb}}(\rho_{\mathrm{IC}})}{V_{\mathrm{IC}}\tau_{E,x}^{\mathrm{IC}}} \int_{\mathrm{IC}} n(\rho) T(\rho) \frac{dV(\rho)}{d\rho} d\rho \tag{7.22}$$

and $G_{E,\mathrm{IC}}$ is a term to account for the changes in the inner core as a result of changes in the edge, as described previously. As with the diffusive particle loss term, we can estimate that $\tau_{E,x}^{\mathrm{IC}} \approx \rho_{\mathrm{IC}}\tau_E^{98}$ will be a couple of seconds. A better model for this parameter can be constructed when ITER data becomes available.

7.3 Node 2: Outer Core and Edge

7.3.1 Particle Sources and Sinks in the Outer Core

The primary particle sources in the outer core and edge are radial diffusive transport (both from the inner core and into the SOL), particle deposition from NBI, and particle deposition from SPI. Particles are lost from this region through IOL, through being consumed in fusion, and through radial diffusive transport. These sources and sinks, by analogy with the sources in Section 7.2, can be written as

$$S_{x,\mathrm{dif}}^{\mathrm{OC}}(t) = \frac{V_{\mathrm{IC}}}{V_P - V_{\mathrm{IC}}} \frac{n_x^{\mathrm{IC}}}{\tau_{P,x}^{\mathrm{IC}}} - \frac{n_x^{\mathrm{OC}}}{\tau_{P,x}^{\mathrm{OC}}} \tag{7.23}$$

$$S_{x,\mathrm{IOL}}^{\mathrm{OC}}(t) = \frac{-1}{\tau_{P,x}^{\mathrm{OC}}} \int_{\mathrm{OC}} n_x(\rho) \frac{dF_{x,\mathrm{orb}}(\rho)}{d\rho} d\rho \tag{7.24}$$

$$S_{\mathrm{D,NBI}}^{\mathrm{OC}}(t) = \frac{1}{V_{\mathrm{IC}}} \sum_k \frac{F_{k,\mathrm{D}}}{E_k} \int_{\mathrm{OC}} \frac{\partial P_k(\rho)}{\partial \rho} d\rho \tag{7.25}$$

$$S_{\mathrm{x,SPI}}^{\mathrm{OC}}(t) = \frac{1}{V_{\mathrm{IC}}} F_{\mathrm{p},x} \int_{\mathrm{OC}} \frac{\partial S_{\mathrm{p}}(\rho)}{\partial \rho} d\rho \tag{7.26}$$

$$S_{\mathrm{D,fus}}^{\mathrm{OC}}(t) = S_{\mathrm{T,fus}}^{\mathrm{OC}}(t) = -\frac{1}{4} d \min\left\{n_D^{\mathrm{OC}}(t), n_T^{\mathrm{OC}}(t)\right\}^2 \langle \sigma v \rangle_f (T_{\mathrm{OC}}(t)) \tag{7.27}$$

Based on the results of Chapter 5, in which it was found that the amount of ion orbit loss was most strongly dependent on plasma current I_P, it may be possible to approximate the IOL loss term as a somewhat simpler function of current.

7.3.2 Power Sources and Sinks in the Outer Core

The primary power sources and sinks in the outer core are those resulting from fusion, beam heating, auxiliary RF heating, EC radiation (both emitted and reabsorbed), impurity radiation, ion orbit loss, and radial diffusive transport. The terms for those sources and sinks can be written as

$$P_{\mathrm{x,fus}}^{\mathrm{OC}}(t) = \frac{1}{4} d \min\left\{n_D^{\mathrm{OC}}(t), n_T^{\mathrm{OC}}(t)\right\}^2 \langle \sigma v \rangle_f \left(T_{\mathrm{OC}}(t)\right) U_{\alpha x} F_{\mathrm{IOL}}^{\mathrm{OC}} \tag{7.28}$$

$$P_{\mathrm{x,NBI}}^{\mathrm{OC}}(t) = \frac{1}{V_{\mathrm{OC}}} \sum_k \frac{U_{k,x}}{E_k} \int_{\mathrm{OC}} \frac{\partial P_k(\rho)}{\partial \rho} d\rho \tag{7.29}$$

$$P_{\mathrm{x,RF}}^{\mathrm{OC}}(t) = \frac{F_{x,\mathrm{RF}}^{\mathrm{OC}}}{V_{\mathrm{OC}}} \int_{\mathrm{OC}} \frac{\partial P_{\mathrm{RF}}(\rho)}{\partial \rho} d\rho \tag{7.30}$$

$$P_{\mathrm{EC}}^{\mathrm{OC}}(t) = \frac{1}{V_{\mathrm{OC}}} \int_{\mathrm{OC}} \frac{\partial P_{\mathrm{EC}}(\rho)}{\partial V} \frac{dV}{d\rho} d\rho \tag{7.31}$$

$$P_{\mathrm{imp}}^{\mathrm{OC}}(t)\left(MW/m^3\right) \approx \sum_k \left(1 + 0.3 T_e^{\mathrm{OC}}(t)\right) \times 10^{-43} n_e^{\mathrm{OC}}(t) n_k(t) z_k^{\left(3.7 - 0.33 \ln\left[T_e^{\mathrm{OC}}(t)\right]\right)} \tag{7.32}$$

$$P_{x,\mathrm{dif}}^{\mathrm{OC}}(t) = \frac{3V_{\mathrm{IC}}}{2\left(V_P - V_{\mathrm{IC}}\right)} \frac{n_x^{\mathrm{IC}}(t) T_x^{\mathrm{IC}}(t)}{\tau_{e,x}^{\mathrm{IC}}} - \frac{3}{2} \frac{n_x^{\mathrm{OC}}(t) T_x^{\mathrm{OC}}(t)}{\tau_{e,x}^{\mathrm{OC}}} \tag{7.33}$$

Although these equations are similar to those written for the inner core, it should be noted that IOL of fast α particles is much more probable in the outer core. This could

have several important consequences, including a reduced likelihood of a thermal power excursion in the outer core. Non-uniform momentum loss from fast α particles in the outer core may also provide a source of intrinsic rotation in a D-T plasma that would be absent in a D-D plasma.

7.4 Node 3: Scrape-off Layer

7.4.1 Particle Sources and Sinks in the SOL

The neutrals calculations reported in Chapter 6 suggest that the ITER plasma will be quite opaque to neutrals, which would render massive gas injection (MGI) largely ineffective for core fueling and impurity injection. This is not the case in the SOL, so a term must be added for an external MGI particle source. The relatively small fraction of MGI particles that penetrate beyond the SOL and are ionized in the edge may be important for edge physics, however, they will contribute very little to the overall power balance in the outer core region and are best accounted for in the SOL and divertor. The particle source in the SOL from MGI can be represented as

$$S^{\mathrm{SOL}}_{x,\mathrm{MGI}}(t) = \frac{S^{\mathrm{tot}}_{x,\mathrm{MGI}}(t)\, F^{\mathrm{SOL}}_{\mathrm{MGI}}}{V_{\mathrm{SOL}}} \tag{7.34}$$

Here, $S^{\mathrm{tot}}_{x,\mathrm{MGI}}$ is the total MGI source of species x, and $F^{\mathrm{SOL}}_{\mathrm{MGI}}$ is the fraction of $S^{\mathrm{tot}}_{x,\mathrm{MGI}}$ that is ionized in the SOL. This quantity can be calculated from neutral particle transport codes such as Neutpy, and then related to SOL densities and temperatures using regression analysis to obtain a more computationally efficient estimate of the MGI source term.

The particle balance in the SOL also differs somewhat from those of regions inside the seperatrix because of the presence of volumetric sources and sinks resulting from the ionization of neutrals, and the recombination of low-temperature ions with electrons to

form neutral particles, which are removed from the ion particle balance.

$$S_{x,\mathrm{ion}}^{\mathrm{SOL}}(t) = n_E^{\mathrm{SOL}} n_{x,0}(t) \langle \sigma v \rangle_{x,\mathrm{ion}} \left(T_e^{\mathrm{SOL}}(t) \right) \tag{7.35}$$

$$S_{x,\mathrm{rec}}^{\mathrm{SOL}}(t) = -\left[n_e^{\mathrm{SOL}}(t) \right]^2 \langle \sigma v \rangle_{x,\mathrm{rec}} \left[T_e^{\mathrm{SOL}}(t) \right] \tag{7.36}$$

Lastly, it should also be noted that although there is a strong particle source in the SOL from radial diffusion across the seperatrix, the analogous sink in the SOL is actually parallel transport into the divertor region. Despite this distinction, we will use the "dif" notation for both the radial source and the parallel sink for the sake of simplicity.

$$S_{x,\mathrm{dif}}^{\mathrm{SOL}}(t) = \frac{V_{\mathrm{P}} - V_{\mathrm{IC}}}{V_{\mathrm{SOL}}} \frac{n_x^{\mathrm{OC}}}{\tau_{P,x}^{\mathrm{OC}}} - \frac{n_x^{\mathrm{SOL}} T_x^{\mathrm{SOL}}}{\tau_{P,x}^{SOL}} \tag{7.37}$$

Because the regular transport losses in this region are primarily along the field lines rather than across them, $\tau_{P,x}^{SOL}$ and $\tau_{E,x}^{SOL}$ are much shorter than in regions inside the seperatrix, on the order of a few ms.

7.4.2 Power Sources and Sinks in the SOL

As in the previous section, the radial power source into the divertor and parallel sink are combined into a single term, which is written as

$$P_{x,\mathrm{dif}}^{\mathrm{SOL}}(t) = \frac{3\left(V_{\mathrm{P}} - V_{\mathrm{IC}}\right)}{2V_{\mathrm{SOL}}} \frac{n_x^{\mathrm{OC}}(t)\, T_x^{\mathrm{OC}}(t)}{\tau_{e,x}^{\mathrm{OC}}} - \frac{3}{2} \frac{n_x^{\mathrm{SOL}}(t)\, T_x^{\mathrm{SOL}}(t)}{\tau_{e,x}^{\mathrm{SOL}}} \tag{7.38}$$

Radiative losses in the SOL could conceivably be treated using a fit as was done in the regions inside the seperatrix, however due to the complex atomic physics considerations in the SOL and the implications of the SOL power balance for conditions in the divertor, it may be beneficial to use atomic physics data and the resulting L_z function more directly. The radiative losses from the SOL will depend not only on intrinsic impurities already in

the plasma, but any impurities injected using MGI. The power sink from impurity radiation can be written as

$$P_{x,\mathrm{rad}}^{\mathrm{SOL}}(t) = \sum_{k} n_{k}^{\mathrm{SOL}}(t)\, n_{e}^{\mathrm{SOL}}(t)\, L_{z,k}\left(T_{e}^{\mathrm{SOL}}(t)\right) \tag{7.39}$$

where n_k is the density of impurity species k.

In the SOL it is also important to account for cooling of ions via collisions with cold, uncollided neutral particles, the loss of the electronic "binding energy" corresponding to ionization of neutrals (see Chapter 1), and the analogous increase in the energy of the system corresponding to recombination of ions and electrons

$$\begin{aligned} P_{x,\mathrm{at}}^{\mathrm{SOL}}(t) = &-\frac{3}{2}\left(T_{x}^{\mathrm{SOL}}(t) - T_{0}^{c}\right) n_{x}^{\mathrm{SOL}}(t)\, n_{0,c}^{\mathrm{SOL}}(t)\, \langle\sigma v\rangle_{\mathrm{at}}^{\mathrm{SOL}}\left(T_{e}^{\mathrm{SOL}}(t)\right) \\ &- E_{\mathrm{ion}} n_{e}^{\mathrm{SOL}}(t)\, n_{0}^{\mathrm{SOL}}(t)\, \langle\sigma v\rangle_{\mathrm{ion}}^{\mathrm{SOL}}\left(T_{e}^{\mathrm{SOL}}(t)\right) \\ &+ f I_{\mathrm{ion}} n_{e}^{\mathrm{SOL}}(t)\, n_{x}^{\mathrm{SOL}}(t)\, \langle\sigma v\rangle_{\mathrm{rec}}^{\mathrm{SOL}}\left(T_{e}^{\mathrm{SOL}}(t)\right) \end{aligned} \tag{7.40}$$

f is the fraction of the ionization potential released upon recombination that is absorbed in the plasma [8]. The energy required for ionization can be estimated [8] as

$$E_{\mathrm{ion}}(eV) = 17.5 + \left[5.0 + \frac{35.5}{T(eV)}\right] \log_{10}\left(\frac{10^{21}}{n}\right) \tag{7.41}$$

A recombination event releases the ionization potential energy for hydrogen of I_{ion} = 13.6 eV into the plasma.

7.5 Node 4: Divertor

7.5.1 Particle Sources and Sinks in the Divertor

The particle balance in the divertor region is similar to that of the SOL region. The most notable difference is that the transport sink is into a wall rather than into another region. The resulting transport source and sink term can be written as

$$S_{x,\mathrm{dif}}^{\mathrm{DIV}}(t) = \frac{V_{\mathrm{SOL}}}{V_{\mathrm{DIV}}} \frac{n_x^{\mathrm{SOL}}}{\tau_{P,x}^{\mathrm{SOL}}} - \frac{A_{\mathrm{DIV}}}{V_{\mathrm{DIV}}} n_x^{\mathrm{DIV}} c_{x,s} (1 - R_w) \tag{7.42}$$

Here A_{DIV} is the combined effective surface area of the inboard and outboard divertor targets. V_{DIV} is the total volume of the inboard and outboard divertor regions. $c_{x,s}$ is the sound speed of species x in the divertor, and is calculated [8] as

$$c_{x,s} = \sqrt{\frac{2T_x^{\mathrm{DIV}}}{m_x}} \tag{7.43}$$

where m_x is the mass in kg of species x. R_w is the fraction of ions impinging on the wall that are reflected as ions. The other particle sources and sinks in the divertor region can be written as

$$S_{x,\mathrm{MGI}}^{\mathrm{DIV}} = \frac{S_{x,\mathrm{MGI}}^{\mathrm{tot}} F_{\mathrm{MGI}}^{\mathrm{DIV}}}{V_{\mathrm{DIV}}} \tag{7.44}$$

$$S_{x,\mathrm{ion}}^{\mathrm{DIV}}(t) = n_E^{\mathrm{DIV}} n_{x,0}(t) \langle \sigma v \rangle_{x,\mathrm{ion}} \left(T_e^{\mathrm{DIV}}(t) \right) \tag{7.45}$$

$$S_{x,\mathrm{rec}}^{\mathrm{DIV}}(t) = -\left[n_e^{\mathrm{DIV}}(t) \right]^2 \langle \sigma v \rangle_{x,\mathrm{rec}} \left(T_e^{\mathrm{DIV}}(t) \right) \tag{7.46}$$

7.5.2 Power Sources and Sinks in the Divertor

The volumetric power loss to the wall in the divertor is of a similar form to the volumetric particle loss.

$$P_{x,\mathrm{dif}}^{\mathrm{DIV}}(t) = \frac{3V_{\mathrm{SOL}}}{2V_{\mathrm{DIV}}} \frac{n_x^{\mathrm{SOL}}(t)\, T_x^{\mathrm{SOL}}(t)}{\tau_{e,x}^{\mathrm{SOL}}} - \frac{A_{\mathrm{DIV}}}{V_{\mathrm{DIV}}} n_x^{\mathrm{DIV}} c_{x,s} T_x^{\mathrm{DIV}} \gamma_{\mathrm{sh}} \tag{7.47}$$

The sheath energy transmission coefficient γ_{sh} can be represented [8] by

$$\gamma_{\mathrm{sh}} = \frac{2T_i^{\mathrm{DIV}}}{T_e^{\mathrm{DIV}}} + \frac{2}{1-\delta_{\mathrm{sh}}} + \frac{1}{2}\ln\left[\frac{(1-\delta_{\mathrm{sh}})\, m_i/m_e}{2\pi\,(1+T_i^{\mathrm{DIV}}/T_e^{\mathrm{DIV}})}\right] \tag{7.48}$$

where δ_{sh} is a secondary sheath transmission coefficient. The radiative and atomic physics terms in the divertor power balance are very similar to those in the SOL power balance.

$$P_{x,\mathrm{rad}}^{\mathrm{DIV}}(t) = \sum_k n_k^{\mathrm{DIV}}(t)\, n_e^{\mathrm{DIV}}(t)\, L_{z,k}\left(T_e^{\mathrm{DIV}}(t)\right) + \sum_j n_j^{\mathrm{DIV}} n_e^{\mathrm{DIV}}(t)\, L_{z,j}\left(T_e^{\mathrm{DIV}}(t)\right) \tag{7.49}$$

$$P_{x,\mathrm{at}}^{\mathrm{DIV}}(t) = -\frac{3}{2}\left(T_x^{\mathrm{DIV}}(t) - T_0^c\right) n_x^{\mathrm{DIV}}(t)\, n_{0,c}^{\mathrm{DIV}}(t)\, \langle\sigma v\rangle_{\mathrm{at}}^{\mathrm{DIV}}\left(T_e^{\mathrm{DIV}}(t)\right) - E_{\mathrm{ion}} n_e^{\mathrm{DIV}}(t)\, n_0^{\mathrm{DIV}}(t)\, \langle\sigma v\rangle_{\mathrm{ion}}^{\mathrm{DIV}}\left(T_e^{\mathrm{SOL}}(t)\right) + f I_{\mathrm{ion}} n_e^{\mathrm{DIV}}(t)\, n_x^{\mathrm{DIV}}(t)\, \langle\sigma v\rangle_{\mathrm{rec}}^{\mathrm{DIV}}\left(T_e^{\mathrm{DIV}}(t)\right) \tag{7.50}$$

7.6 Delay Differential Equations and Burning Plasma Dynamics

To account for the delayed effects of several burn control mechanisms, we must use delay differential equations, which express a quantity as a function, not only of time, but also of

another time in the past. Delay differential equations have the form

$$\frac{d}{dt}y\left(t\right) = f\left(t, y\left(t\right), y_t\right) \tag{7.51}$$

where $y_t = \{y\left(\tau\right) : \tau \leq t\}$. The relationship between a quantity y at time t and the values of that quantity at several previous times with delays $0 \leq \tau_m \leq t$ can be written as

$$\frac{d}{dt}y\left(t\right) = f\left(t, y\left(t\right), y\left(t-\tau_1\right), \cdots, y\left(t-\tau_M\right)\right), \quad \text{for} \quad \tau_1 \leq \cdots \leq \tau_M \tag{7.52}$$

In the context of tokamak burn control, we are interested in relating the local density, temperature, power output, or some other quantity in a region at time t to the conditions in that region or another region at some time $t - \tau$. For example, we may be interested in the temperature in the inner core at time t following an increase in edge radiative cooling at time $t - \tau_a$. We might also be interested in the knowing the increased temperature in the divertor at time t following a thermal power excursion in the inner core at time $t - \tau_b$.

Because we are primarily concerned with changes in temperature, the equation for ion density, for example, may be related to temperatures at previous times rather than densities at previous times. Such an equation could be represented by

$$\frac{dn\left(t\right)}{dt} = f\left(t, n(t), \{T\left(t-\tau_m\right)\}\right), \quad 0 \leq \tau_1 \leq \tau_2 \leq \cdots \leq \tau_m \leq t \tag{7.53}$$

where $\{T\left(t-\tau_m\right)\}$ is the set of all temperatures at times $t - \tau_m$ that are important for the calculation of the density at time t.

In some cases, order of magnitude estimates can be made for some of the delay constants and other coefficients in the model, however better values for all of these coefficients would necessarily require data from the early stages of ITER operation. The delay constants could be tuned using regression analyses [17] or more advanced machine learning approaches.

7.6.1 Implementation of Delay Constants

The delay constants are mostly important for actuator control. This is not only to account for the delay with which some actuators (e.g. MGI) effect plasma conditions, but also because data over a range of time may be needed to positively identify trends in the data that would indicate the need for corrective burn control actions.

Terms in the equations in this chapter that involve an source or sink that can be controlled in real time should be written not only as a function of t, ρ, etc. but also of core temperature conditions at a time in the past. For example, the particle source to the inner core from neutral beams could be written as

$$S_{\mathrm{D,NBI}}\left(t\right) = \frac{1}{V_{\mathrm{IC}}} \sum_{k} \frac{F_{k,\mathrm{D}}}{E_k\left(T_{\mathrm{IC}}\left(t-\tau_{\mathrm{NBI}}\right)\right)} \int_{\mathrm{IC}} \frac{\partial P_k\left(\rho, T_{\mathrm{IC}}\left(t-\tau_{\mathrm{NBI}}\right)\right)}{\partial \rho} d\rho \tag{7.54}$$

where the beam energy and power are adjusted based on conditions in the inner core at time $t - \tau_{\mathrm{NBI}}$. Other sources and sinks could be written in a similar way.

7.7 Multi-Nodal Dynamics Model Conclusions

This chapter has described the species-specific particle and power balance equations that would comprise a multi-nodal plasma dynamics model. 0-D fusion reactor dynamics models, while useful for a wide variety calculations, are limited in their ability to adequately model physics phenomena in different regions of the plasma on a variety of timescales. Data gained during the early stages of ITER operation could be used to tune the time constants and other model coefficients described in this chapter. An interesting next step for this model would be to incorporate it into an optimal control theory-based actuator control algorithm.

CHAPTER 8
CONCLUSION

Over the last several decades, myriad analyses have been performed of the global stability of burning and ignited plasmas. Some have drawn attention to the possibility of thermal runaways [15] while others have predicted access to globally stable operating points [14], or predicted difficulty in achieving significant fusion power in the first place [83]. Others [84] have explored the active control strategies that will undoubtedly be necessary to manage the significant power source from fusion in burning plasmas.

Many past analyses have predicted thermal stability based on POPCON plots and other relatively simple tools. Although these analyses provide grounds for optimism, they implicitly include power loss mechanisms that would be different in ITER, and unavailable in the inner core where thermal power excursions are most likely. They are also incapable of adequately representing core dynamics that happen on timescales significantly shorter than a global confinement time.

This analysis has taken a different approach by looking at specific passive and active mechanisms by which a thermal power excursion could be limited, while taking into account the timescales on which those mechanisms operate.

8.1 Research Conclusions

Several potential passive negative reactivity feedback mechanisms were investigated, including electron cyclotron radiation from the core, ion orbit loss, positive temperature dependences in the impurity emissivity functions of various elements, and MARFEs. Of these, only electron cyclotron radiation was found to passively affect fusion rates on a rapid timescale in response to temperature increases. Electron cyclotron has the greatest effect at temperatures $\gtrsim$ 30 keV, however even at somewhat elevated temperatures, it was

insufficient to guarantee thermal stability. The total power loss from electron cyclotron is sensitive to the wall reflectivity at those frequencies. It may be possible to achieve core thermal stability against power excursions by reducing wall reflectivity at EC frequencies. In any case, because of the role that EC will play in the power balance, especially at higher temperatures, the EC reflectivity of wall materials warrants further research.

Impurity radiation results in significant power losses in tokamaks. The impurity radiation emissivity function was calculated as a function of both electron temperature and the local fraction of neutral hydrogen for several ITER-relevant impurity species. Unfortunately for the goal of passive burn control, significantly positive dependences of the emissivity functions on temperature was not found in realistic ranges of the temperature and neutral concentration for any of the species investigated. Active impurity seeding through pellet injection, gas injection, and by controlling impurity transport characteristics, however, could still be important elements of a burn control strategy. Noble gases have long been investigated for radiative power exhaust because of their non-reactive properties, and of the noble gases, neon and argon are the most promising. Krypton and higher-z noble gases would likely radiate too strongly. Radiative power exhaust of between 10 and 100 MW can be achieved using reasonable neon and argon concentrations. Argon's radial power loss profile is peaked in the edge, which could make it particularly useful for removing power deposited in the edge via EC.

Additionally, recent results at DIII-D suggest that by varying the on-axis ECCD, plasma controllers could modify impurity concentrations in the inner core. This could prove to be an important active burn control mechanism as it is one of relatively few actuators that can quickly effect conditions in the inner core.

Ion orbit loss (IOL) theory was presented and loss fractions were calculated for several species, including fast α particles and thermalized deuterium and hydrogen. IOL of thermalized particles was found to be insignificant, with loss fractions becoming meaningful only in the very far edge. Fast α losses, however, can extend further into the core. Al-

though the fast α losses do not increase with increases in the temperature of the background plasma, they could reduce or redistribute the effective $\langle \sigma v \rangle_{\rm fus}$ in the plasma, effectively reducing the likelihood and severity of a power excursion. This phenomena would also, of course, reduce the effective fusion power of a reactor operating at a given density and temperature relative to what it would have been without fast α IOL. Lastly, it was noted that fast α IOL in the outer core of a D-T plasma may result in a source of intrinsic momentum that would be absent in a D-D plasma due to the lack of fusion α particles.

Transitions from high confinement mode (H-mode) to low confinement mode (L-mode) significantly reduce confinement, which could be useful in the event of a thermal power excursion. MARFE-initiated H-L transitions were investigated to determine the extent to which they could be useful in either a passive or active approach to burn control. Although some interesting positive temperature dependences of the MARFE onset criteria were found, they are unlikely to be realized in ITER.

It was found that MARFEs effect core conditions on a timescale of approximately a global H-mode confinement time, which is not surprising. Unfortunately, ITER's ~ 4 second confinement time is significantly longer than the timescales on which power excursion may need to be mitigated.

If it becomes useful to deliberately trigger a MARFE, the analyses in Chapter 6 suggest that impurity gas puffing in the ITER divertor is more likely to be successful than deuterium gas puffing. Depending on the tungsten concentration in the vicinity of the x-point, it is likely that injecting argon or another impurity species could create the conditions that would result in a MARFE. The slow timescales on which a MARFE could effect core conditions, however, suggests that deliberate MARFE initiation will have limited utility in mitigating a power excursion in the inner core.

Recognizing that conditions in the inner core are likely to evolve differently than in other regions of the plasma, a multi-nodal model for burning plasma dynamics was constructed in Chapter 7 that could be used in lieu of the rather simplistic 0-D model described

in Chapter 2. The delay differential equations include a variety of time constants and delay factors for which models could be constructed from ITER data during the first several years of operation.

8.2 Suggestions for Future Work

8.2.1 Refinement and Extension of Multi-Nodal Dynamics Model Using Optimal Control Theory

This analysis has made the case for a multi-nodal approach to burn control and proposed a set of equations that could capture the relevant physics and time constants involved. A logical next step would be to use this system as the basis for actuator control using optimal control theory. The need for delay differential equations complicates the solution somewhat, however this could be an interesting research topic for someone with an interest in optimal control theory and a reasonably strong mathematical background.

8.2.2 Extension of Neutpy to EC Transport

This analysis used EC deposition profile results from the literature that were generated for ITER using the RAYTEC code, which appears to be the state of the art in EC transport codes. It is not clear how computationally efficient the code is, but even if it runs quickly, confirmation using another code could be very useful, especially given our evolving understanding of the role of EC radiation in ITER's power balance. The transmission and escape probability (TEP) methodology used in Neutpy is a powerful approach to modeling transport that could, in theory, be readily adapted to EC transport. This new code would also make it possible to explore the heat removal implications of potential non-uniformities of EC heating of the first wall, which were discussed briefly in Chapter 3.

8.2.3 Modifying EC Reflectivity in ITER

It was found in Chapter 3 that even modest changes in the reflectivity of the ITER wall for EC frequencies could have significant effects on the global power balance. Given that the reflectivity is not currently well known (values in the literature range from 0.6 to 0.9), this seems like a question that warrants further investigation prior to ITER's operation. It is conceivable that wall conditioning or modification could play a role in a burn control strategy by controlling the amount of EC power generated in the core that is reflected back into the plasma, where at least some of it will reheat the plasma.

8.2.4 Using Neutpy to Study Effects of Wall Conditioning on Particle Balance

Although not explored in this thesis, wall conditioning is the process of treating the walls of the reactor to alter particle absorption, reemission, and other wall characteristics. Because Neutpy is reasonably computationally efficient, a large number of neutral particle transport calculations could be done to evaluate a variety of plasma-wall interaction models with a variety of delay constants. These calculations could be compared with experiment to refine plasma-wall interaction models and better understand the effects that changes to the wall, deliberate or otherwise, subsequently have on plasma conditions.

8.2.5 Fast α Internal Ion Orbit Loss

It is a major assumption of the IOL calculations in this thesis that fast α particles born in fusion are either immediately lost from the plasma or they deposit their energy on the flux surface on which they were born. In fact, there are other possibilities. Energetic particles that are not quite energetic enough to reach the seperatrix still execute unusual orbits that could result in the particles experiencing their first major collision in a very different region of the plasma. In a burning plasma, direct fast α transport from one region to another could have significant effects on the shape of the temperature distribution and on the global power balance. To estimate these effects, the IOL model described in this thesis would need to

be used over a range of "exit" flux surfaces and an approximate model for the probability of collisions along the trajectory would need to be developed. Early calculations [85, 86] suggested that fusion α particles will deposit their energy primarily on the flux surface on which they are born, however it would be interesting to revisit these calculations using the latest developments in IOL theory.

8.2.6 Tungsten Transport in ITER and On-Axis ECCD

Results from DIII-D indicate that the location of ECCD injection can have significant implications for carbon and neon build up in the core. This thesis proposes that this phenomenon be further investigated as an active control mechanism for controlling the power balance in ITER. We need more insight into the exactly physical mechanisms by which ECCD effects impurity transport and an assessment of the extent to which it would act on tungsten, beryllium, and any other impurities that will be found in ITER.

8.2.7 Analysis of MARFE-Onset Criteria in the Presence of Tungsten

The analyses in Chapter 6 led to the conclusion that the tungsten impurity fraction in the vicinity of the x-point may have a significant role to play in determining the likelihood of MARFE instabilities in ITER. JET's recent upgrade to an ITER-like wall and tungsten divertor [87] may provide an opportunity to test our expectation of MARFEs in ITER by applying the model described in this thesis to JET.

Appendices

APPENDIX A

ITER REFERENCE SCENARIO PARAMETERS

A.1 ITER Reference Scenario

The following parameters and radial profiles for ITER are taken from the ITER Technical Basis [27] for several non-inductive scenarios. Here, WNS refers to "Weak Negative Shear," SNS refers to "Strong Negative Shear," and WPS refers to "Weak Positive Shear." Additional information can be found in the ITER Technical Basis.

		Scenario 4		Scenario 6	Scenario 7
		WNS	WNS	SNS	WPS
R/a	(m)	6.35/1.85	6.35/1.85	6.35/1.85	6.35/1.85
B_T	(T)	5.18	5.18	5.18	5.18
I_P	(MA)	9.0	9.5	9.0	9.0
κ_{95}/δ_{95}		1.85/0.40	1.87/0.44	1.86/0.41	1.86/0.41
$<n_e>$	($10^{19}m^{-3}$)	6.7	7.05	6.5	6.7
n/n_G		0.82	0.81	0.78	0.82
$<T_i>$	(keV)	12.5	11.6	12.1	12.5
$<T_e>$	(keV)	12.3	12.6	13.3	12.1
β_T	(%)	2.77	2.67	2.76	2.75
β_N		2.95	2.69	2.93	2.92
β_p		1.49	1.25	1.48	1.47
P_{fus}	(MW)	356	338	340	352
$P_{LH} + P_{NB}$	(MW)	29 + 30 *1	28 + 35	40 + 20 *2	29 + 28 *3
$Q = P_{fus}/P_{add}$		6.0	5.36	5.7	6.2
W_{th}	(MJ)	287	272	287	285
P_{loss}/P_{LH}		2.59	2.74	2.63	2.6
τ_E	(s)	3.1	2.92	3.13	3.07
f_{He}	(%)	4.1	4.0	4.0	4.0
f_{Be}	(%)	2	2	2	2
f_{Ar}	(%)	0.26	0.16	0.2	0.23
Z_{eff}		2.07	1.87	1.89	1.99
P_{rad}	(MW)	37.6	30.6	36.2	34.6
P_{loss}	(MW)	92.5	93.2	91.6	92.7
l_i (3)		0.72	0.43	0.6	0.69
I_{CD}/I_p	(%)	51.9	49.7	53.7	50.2
I_{bs}/I_p	(%)	48.1	50.3	46.3	49.8
I_{OH}/I_p	(%)	0	0	0	0
$q_{95}/q_o/q_{min}$		5.3/3.5/2.2	5.01/3.8/2.7	5.4/5.9/2.3	5.3/2.7/2.1
$H_{H98(y2)}$		1.57	1.46	1.61	1.56
τ_{He}^*/τ_E		5.0	5.0	5.0	5.0

Figure A.1: Parameters for several non-inductive reference ITER scenarios, as given by the ITER Technical Basis [27].

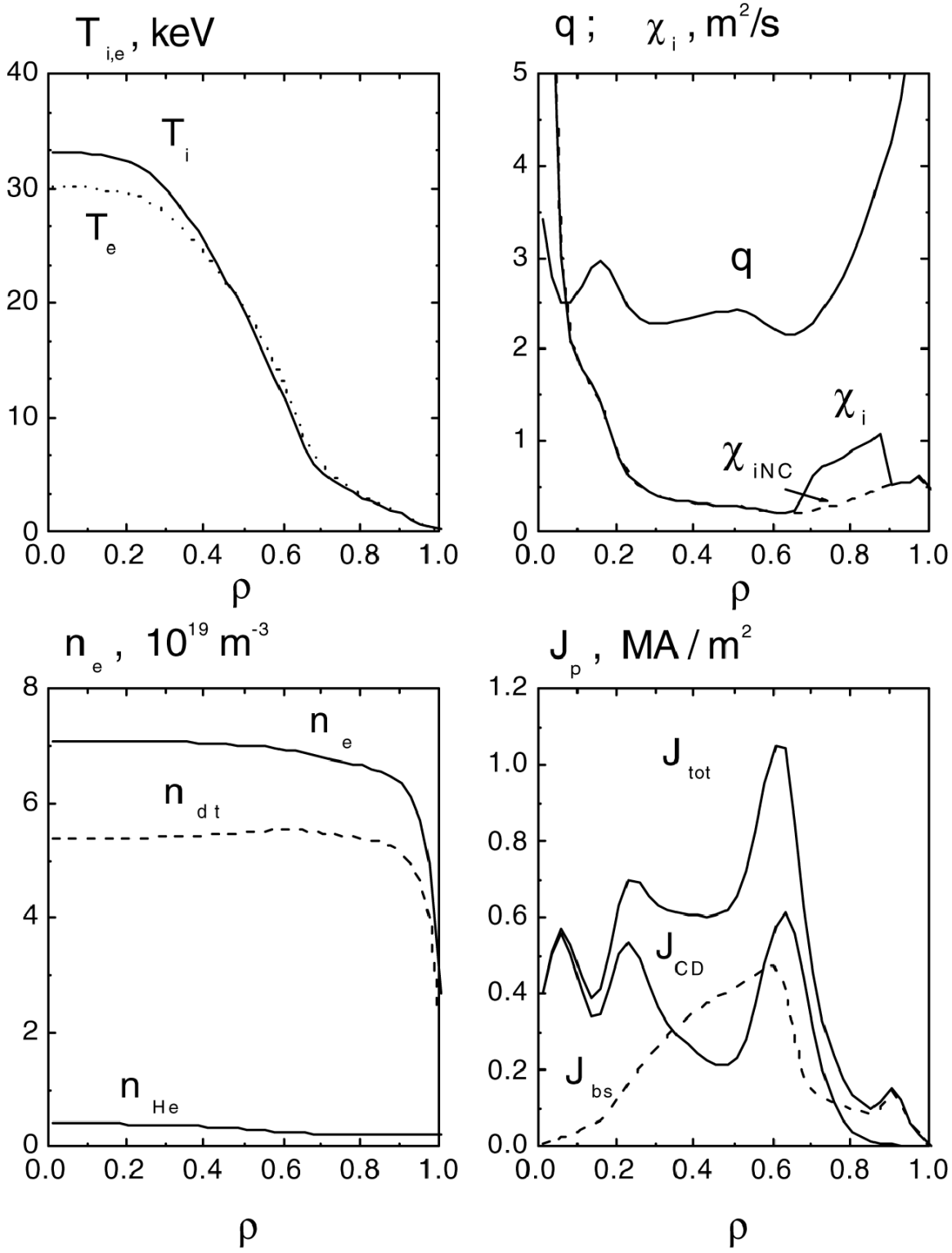

Figure A.2: Several simulated ITER radial profiles from the ITER Technical Basis [27] for non-inductive scenarios.

APPENDIX B

GT3: A NEW CODE FOR TOKAMAK ANALYSIS

GT3, short for Georgia Tech Tokamak Tools, is a new tokamak analytics code that unifies and extends the functionality of most codes developed and used by the Fusion Research Center (FRC) at Georgia Tech. It is written in python and available from the FRC's github page: `https://github.com/gt-frc/gt3`

B.1 Code Organization

GT3 is presently composed of 10 python modules, plus a variety of example input files and pickled L_z iterpolators, which are discussed in a later section. The main modules are:

- **gt3.py**: defines several convenient modes of operation. New users will probably want to instantiate the gt3 class and specify one of the pre-defined modes.

- **read_infile.py**: The ReadInfile class reads in the main input file, as well as radial profile data files specified in the input file, and stores the data in numpy arrays. An instance of the ReadInfile class will have all variables that were successfully read in as attributes.

- **core.py**: The Core class reconstructs the plasma geometry from ψ data, creates an ρ, θ mesh structure, and interpolates radial profiles from the ReadInfile instance onto the ρ, θ mesh. At present, only 1-D profiles are read in, but this could easily be modified to read in 2-d density, temperature, and other profiles. Core also contains quantities related to impurity radiation, neutral densities, ionization rates, etc. however these are initialized as zero and populated by other modules through the various "update" instance methods. Core is instantiated automatically when using the gt3 "wrapper"

module, regardless of the specified mode, since every other module uses the attributes of the Core instance.

- **iol.py**: The IOL class calculates ion orbit loss fractions of particles, momentum and energy for thermalized ions (including impurities), monoenergetic α particles that are uniformly distributed in launch angle, and monoenergetic, monodirectional beam particles.

- **beamdep.py**: The BeamDep class is essentially a wrapper for the nbeams neutral beam particle and energy deposition code. At some point in the future, it is expected that nbeams will be rewritten in python and merged with this module.

- **therm_inst.py**: This module calculates MARFE onset using the model described in Chapter 6, as well as various other thermal instability related quantities, including the global density limit for radial collapse of the temperature profile. [72]

- **sol.py**: The SOL class calculates approximate densities and temperatures in the SOL and halo regions using a kind of strip model [8]. The approach that is currently used is described in more detail in Section B.4. This module is used mostly for creating the neutpy input object, however it could be used for SOL calculations in general.

- **neutpy_prep.py**: The NeutpyPrep first checks for the existence of the user-specified neutralsoutput file, and read it in if it is present. If the file is not present, the class assembles the triangular mesh, populates other data required by neutpy, and runs neutpy. After running neutpy, an output file is created so neutpy doesn't have to be run the next time if nothing else in the model changes.

  The triangular mesh is generatedy using the powerful Triangle code [88], which can be obtained from `https://www.cs.cmu.edu/~quake/triangle.html`. The triangular mesh is constrained to follow flux lines in the core and SOL regions.

Densities and temperatures from all regions are combined and the values at the centers of the triangles are interpolated.

- **imp_rad.py**: The impurity radiation module uses the L_z interpolators if they are found, and generates them if they are not. These interpolator objects can be downloaded from the GT3 repository on github and used directly, even without GT3. These interpolator objects are discussed later in Section B.6.

- **radial_transport.py**: The RadialTransport class infers heat and particle fluxes, transport coefficients, and other related quantities from experimental density and temperature profiles. The class also calculates deuterium rotation velocities from measured carbon rotation velocities using perturbation theory. This module is under active development.

B.2 Basic Usage

Shown below is a simple script for invoking GT3 and plotting some relevant quantities is shown below. The input file being used is for DIII-D shot 164436 at time 3720 ms. Here, the input file is stored in a directory called 164436_3720. The GT3 class takes two arguments: an input file and a mode. The input file is a string variable specifying the relative location of the main input file to be used. The mode refers to one of the predefined modes specifies in gt3.py. These modes currently include options such as "coreonly," "ntrlsandiol," "marfe," and "radialtrans." More will undoubtedly be added in the future.

```
import matplotlib.pyplot as plt
from matplotlib import rc
from gt3 import gt3

# Use latex for generating text in plots.
# Comment this out if it causes problems.
rc('font', **{'family':'serif', 'serif':['Palatino']})
rc('text', usetex=True)

# specify input file and instantiate gt3
input_file = '/164436_3720/togt3_d3d_164436_3720'
shot = gt3(shotlabel=input_file, mode='coreonly')

# plot ion temperature as a function of rho
fig1 = plt.figure(figsize=(4, 4))
ax1 = fig1.add_subplot(1, 1, 1)
ax1.set_xlabel(r'Normalized Minor Radius $\rho$', fontsize=15)
ax1.set_ylabel(r'Ion Temperature (keV)', fontsize=15)
ax1.tick_params(axis='both', which='major', labelsize=15)
ax1.plot(shot.core.rho[:, 0],
         shot.core.T.i.kev[:,0],
         color='black')
plt.tight_layout()

# plot the calculated poloidal magnetic field strength as
# a function of R and Z
fig2 = plt.figure(figsize=(4, 4))
ax1 = fig2.add_subplot(1, 1, 1)
ax1.set_xlabel(r'$R$ (m)', fontsize=15)
ax1.set_ylabel(r'$Z$ (m)', fontsize=15)
ax1.tick_params(axis='both', which='major', labelsize=15)
cax = ax1.contourf(shot.core.R,
                   shot.core.Z,
                   shot.core.B_p,
                   500,
                   cmap='jet')
ax1.axis('equal')
fig2.colorbar(cax)
plt.tight_layout()

fig1.savefig('gt3_Ti.png')
fig2.savefig('gt3_Bp.png')
plt.show()
```

Below is an example input file. Example input files, which are more likely to be current and working, are also provided in the github repository. If variables are not needed for the particular set of calculations being done, they can be excluded from the input file. Lines beginning with # are ignored when reading in the file. Additionally, the input file parameters can be listed in any order. More information on the variables can be found in the official GT3 documentation.

```
#MAIN MESH PARAMETERS
thetapts_approx = 50
#rhopts = 200
edge_rho = 0.7
rhopts_edge = 100
rhopts_core = 10

#MAGNETIC FIELD
BT0 = 2.004

#NEUTRALS PARAMETERS
neut_outfile = gt3_164436_3720_neut.dat
core_thetapts_ntrl = 50
ib_thetapts_ntrl = 10
ob_thetapts_ntrl = 10
#rhopts_ntrl = 100
edge_rho_ntrl = 0.8
rhopts_edge_ntrl = 5
rhopts_core_ntrl = 10
wall_ni_min = 1.0E15
wall_ne_min = 1.0E15
wall_Ti_min = 0.005
wall_Te_min = 0.005
tri_min_angle = 20
tri_min_area = 0.01

#SOL PARAMETERS
sollines_psi_max = 1.07
num_sollines = 3
xi_sep_pts = 30
xi_ib_pts = 10
xi_ob_pts = 10
ib_trim_off = 0.1
ob_trim_off = 0.1
```

```
#PFR PARAMETERS:
pfr_ni_val = 1.0E14
pfr_ne_val = 1.0E14
pfr_Ti_val = 0.002
pfr_Te_val = 0.002

#1D PROFILE INPUT FILES
ne_file = /164436_3720/gt3_164436_3720_ne.dat
nD_file = /164436_3720/gt3_164436_3720_ni.dat
nC_file = /164436_3720/gt3_164436_3720_nc.dat
Te_file = /164436_3720/gt3_164436_3720_Te.dat
Ti_file = /164436_3720/gt3_164436_3720_Ti.dat
TC_file = /164436_3720/gt3_164436_3720_Tc.dat
er_file = /164436_3720/gt3_164436_3720_er.dat
vpolC_file = /164436_3720/gt3_164436_3720_vpolC.dat
vtorC_file = /164436_3720/gt3_164436_3720_vtorC.dat
vpolD_file = /164436_3720/gt3_164436_3720_vpolD.dat
vtorD_file = /164436_3720/gt3_164436_3720_vtorD.dat

2D QUANTITIES INPUT FILES
psirz_file = /164436_3720/gt3_164436_3720_psirz.txt

2D LINE INPUT FILES
wall_file = /machine/gt3_diiid_wall.dat

#NEUTRAL BEAM DEPOSITION
nbeams_loc = /nbeams/nbeams.exe
ebeam = 64.72
abeam = 2
alphain = 0.6475
pbeam = 0.918
rtang = 1.146

#ION ORBIT LOSS CALCULATION
numcos = 20
R_loss = 0.5

#TRIANGLE EXECUTABLE LOCATION
triangle_loc = /triangle/triangle.exe
```

Running the above script with inputs for this particular shot (which are available on github) should produce images like the ones shown in Figure B.1. Most attributes of the

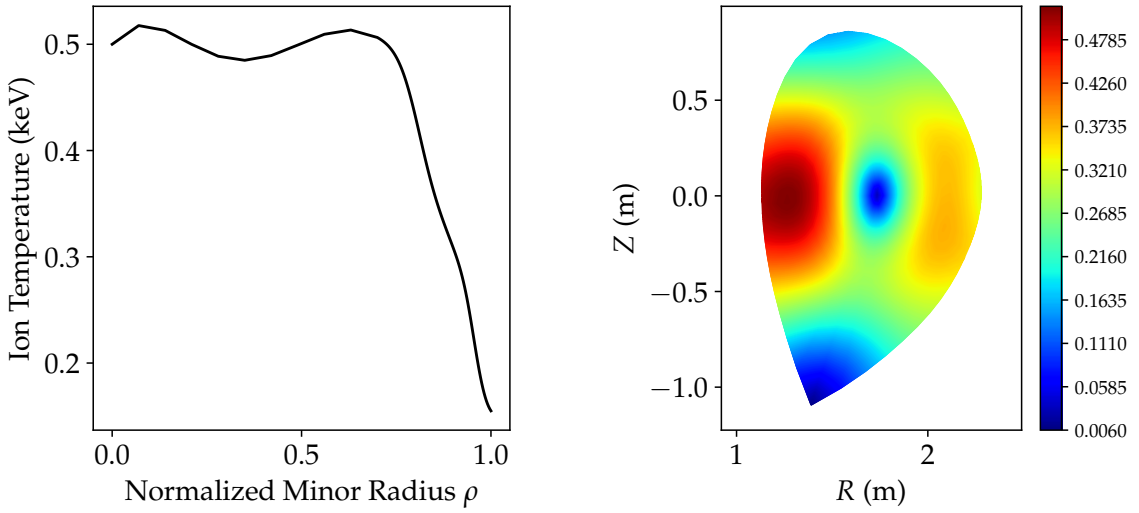

(a) T_i (b) B_p

Figure B.1: Example plots of the 1D ion temperature and the 2D poloidal magnetic field strength from a GT3 analysis of a DIII-D shot.

core instance that vary spatially are stored in 2D arrays, even if they only vary with, for example, ρ.

B.3 Constructing the Background Plasma using ψ Data

Rather than relying on circular or Miller model-based approximations for its background plasma geometry, GT3 is designed to read in experimental ψ data as a function of position (R, Z). This ψ data can be obtained from codes like EFIT, or from a Miller model approach, as discussed in Appendix D. After reading in $\psi\left(R, Z\right)$ GT3 performs the following operations using the raw ψ data:

1. Determine the locations of the x-point and the magnetic axis
2. Compute normalized ψ (usually written as $\widetilde{\psi}$), which goes from 0 at the magnetic axis to 1 at the seperatrix
3. Compute the 2D current density distribution $j\left(R, Z\right)$
4. Compute various geometric quantities (R_0, $R_{0,a}$, a, etc.)

5. Synthesize an r, θ mesh structure based on user-specified numbers of mesh points.

6. Create various useful conversion functions (ρ to $\widetilde{\psi}$, r to $V(r)$, etc.)

B.3.1 Locating Important Points in the Plasma and Normalizing ψ

Before the ψ data can be normalized, the values of ψ at the x-point and at the magnetic axis must be determined. The x-point and magnetic axes both represents saddle points in the ψ data. The magnetic axis is obviously a local minimum, and the x-point is at a saddle point. Local maxima, minima, and saddle points can be found using the first and second derivatives of ψ with respect to R and Z. The process of identifying the magnetic axis and x-point is somewhat complicated by the fact that there can be multiple local minima and saddle points in the psi data, as illustrated in Figure B.2.

Visually, it is clear which intersection is the x-point, which is the magnetic axis, and which correspond to other features or noise, however doing this pragmatically is somewhat more difficult. The logic used in the code at the present time has been shown to work on a large number of DIII-D shots, however if the code seems to be having a hard time processing ψ data correctly, this logic is a potential culprit. For more information on the logic used, consult core.py.

After the code has determined the coordinates of the magnetic axis and the x-point, the ψ data can be normalized to obtain $\widetilde{\psi}(R, Z)$ as

$$\widetilde{\psi}(R, Z) = \frac{\psi(R, Z) + \psi(R_{\text{axis}}, Z_{\text{axis}})}{\psi(R_{\text{xpt}}, Z_{\text{xpt}}) + \psi(R_{\text{axis}}, Z_{\text{axis}})} \tag{B.1}$$

The $\widetilde{\psi}$ data can then be used for drawing flux surfaces in the core and SOL that will ultimately serve as the basis for the r, θ computational mesh.

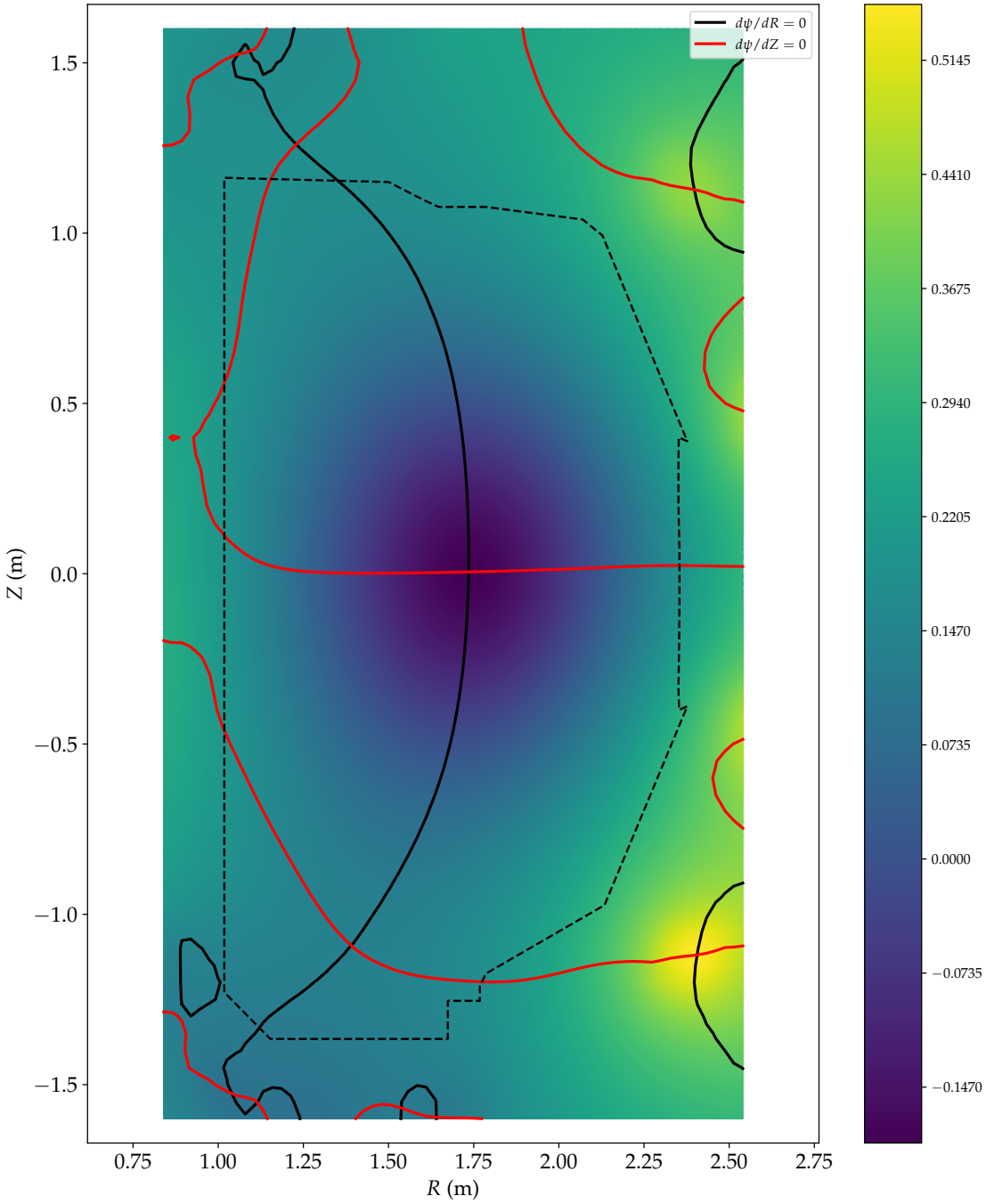

Figure B.2: A filled contour plot of $\psi(R, Z)$ with lines showing contours of $d\psi/dR = 0$ and $d\psi/dZ = 0$. Local maxima, minima, and saddle points occur at the intersections of these lines. The type of point can be determined using the second derivative test.

B.3.2 Computing the Current Density Distribution and the Poloidal Magnetic Field

The current density at a location in the plasma can be calculated from

$$\mu_0 \vec{j} = \frac{1}{R}\frac{dF}{d\psi}\nabla\psi \times \hat{e}_\phi - \frac{1}{R}\Delta^*\psi\hat{e}_\phi \tag{B.2}$$

where the elliptic operator Δ^* is defined as

$$\Delta^*\psi \equiv R^2\vec{\nabla}\cdot\left(\frac{1}{R^2}\vec{\nabla}\psi\right) = R\frac{\partial}{\partial R}\left(\frac{1}{R}\frac{\partial\psi}{\partial R}\right) + \frac{\partial^2\psi}{\partial Z^2} \tag{B.3}$$

and $\hat{e}_\phi$ is a unit vector in the direction of ϕ. Because $F = B_\phi R$ is largely invariant over the plasma, $\vec{j}$ can be estimated as

$$\vec{j}\,(R,Z) \approx -\left[\frac{1}{\mu_0 R}R\frac{\partial}{\partial R}\left(\frac{1}{R}\frac{\partial\psi}{\partial R}\right) + \frac{\partial^2\psi}{\partial Z^2}\right]\hat{e}_\phi \tag{B.4}$$

The strength of the poloidal magnetic field can be calculated from

$$B_\theta\,(R,Z) = \frac{1}{R}\sqrt{\left(\frac{\partial\psi\,(R,Z)}{\partial R}\right)^2 + \left(\frac{\partial\psi\,(R,Z)}{\partial R}\right)^2} \tag{B.5}$$

B.4 Modeling the Scrape-off Layer and Halo Regions

The scrape-off layer is the region of plasma just radially outside of the last closed flux surface (i.e. the seperatrix). Modeling transport in this region of plasma has long been an area of active research, [89, 90, 91, 92, 93, 94] however reasonable approximations of densities and temperatures in this region can be obtained using Bohm diffusion and measurements of the density and temperature gradients in the vicinity of the seperatrix [8].

In GT3 flux surface lines are first obtained from the raw psi data, as described previously. As in the core, some logic based on a knowledge of the problem must be used, for example, to determine if a ψ contour is, in fact, a SOL flux surface and not something

else. Additionally, these ψ contours often intersect the wall and then return into the plasma chamber. For more information on how the SOL flux surface lines are obtained, consult the main GT3 documentation and the sol.py module.

Densities and temperatures are often assumed to decay exponentially in the SOL, i.e.

$$n\left(x\right) = n_{\text{sep}} \exp\left(\frac{-x}{\Delta_n}\right) \tag{B.6}$$

$$T\left(x\right) = T_{\text{sep}} \exp\left(\frac{-x}{\Delta_T}\right) \tag{B.7}$$

where δ_n and δ_T are the characteristic widths of the SOL for density and temperature. These quantities are typically on the order of a centimeter or two. We can obtain approximate values of these quantities from the continuity requirements [8]

$$\Gamma_\perp = -D_\perp \left.\frac{dn}{dr}\right|_{r=a} = \frac{D_\perp n_{\text{sep}}}{\Delta_n} \tag{B.8}$$

$$Q_\perp = -n_{\text{sep}}\chi_\perp \left.\frac{dT}{dr}\right|_{x=0} - 3T_{\text{sep}} D_\perp \left.\frac{dn}{dr}\right|_{r=a} \tag{B.9}$$

which can be solved for

$$\Delta_n = \frac{D_\perp}{\Gamma_\perp / n_{\text{sep}}} \tag{B.10}$$

and

$$\Delta_T = \frac{\chi_\perp}{Q_\perp / \left(n_{\text{sep}} T_{\text{sep}}\right) - 3D_\perp/\Delta_n} \tag{B.11}$$

In GT3, $\Gamma_\perp$ and $Q_\perp$ are calculated for each point along the seperatrix. The value of dn/dx and dT/dx at each point on the seperatrix are calculated by assuming that densities and temperatures are uniform on a flux surface. This allows us to write

$$\left.\frac{d\left\{n,T\right\}}{dr}\left(r,\theta\right)\right|_{r=a} = \left.\frac{d\left\{n,T\right\}}{d\widetilde{\psi}}\left(r\right)\frac{\partial\widetilde{\psi}}{\partial r}\left(r,\theta\right)\right|_{r=a} \tag{B.12}$$

where

$$\frac{\partial\widetilde{\psi}}{\partial r} = \left|\frac{\partial\widetilde{\psi}}{\partial R}\right| + \left|\frac{\partial\widetilde{\psi}}{\partial Z}\right| \tag{B.13}$$

Example plots of dn/dr, $D_\perp$, $\Gamma_\perp$, and Δ_n along the seperatrix in DIII-D shot 164436.3720 are shown in Figure B.3. Similar quantities are shown for the temperature calculation are shown in Figure B.4. Currently, reasonable assumptions are made for these quantities along the divertor legs. Eventually, these assumptions should be replaced with a parallel transport calculation.

Once the Δ's have been calculated, the density and temperature can, in principle, be found throughout the SOL and halo regions as a function of the distance away from the seperatrix. Ion density and temperature are shown in Figures B.5 and B.6, respectively. Densities and temperatures along the SOL flux lines and first wall are estimated finding the closest point on those lines at for point along the seperatrix, and drawing them in the "strip" models. In Figures B.5 and B.6, the dashed lines are the SOL flux lines and the solid line is the first wall.

B.5 IOL Calculations on the GT3 Background Plasma

IOL is calculated in GT3 as described in Chapter 5. To make use of C code underlying vectorized operations in numpy, most quantities used in the iol module to calculate radial loss profiles are stored as 4-D arrays. In the current version of the code, this can become memory intensive if too many launch angle cosines, theta locations, etc. are specified by the user. As long as reasonable values are selected, however, the code can be run on a laptop without any problems.

The arrays are constructed as as follows:

```
array = array[launch theta position,
              launch angle cosine position,
              launch rho position,
              exit theta position]
```

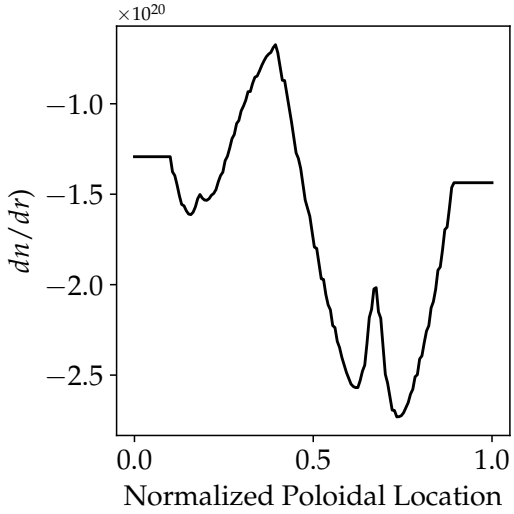

(a) dn_i/dr

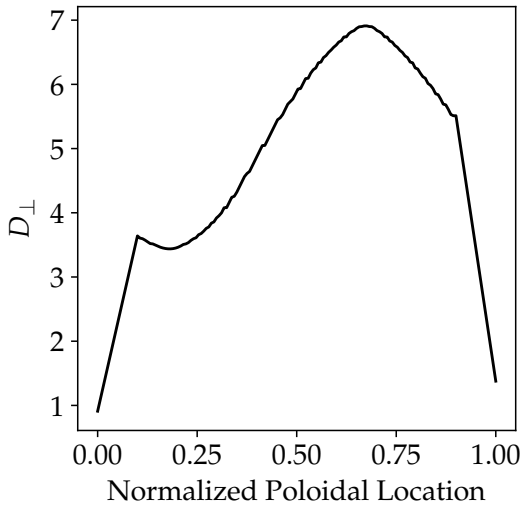

(b) $D_\perp$

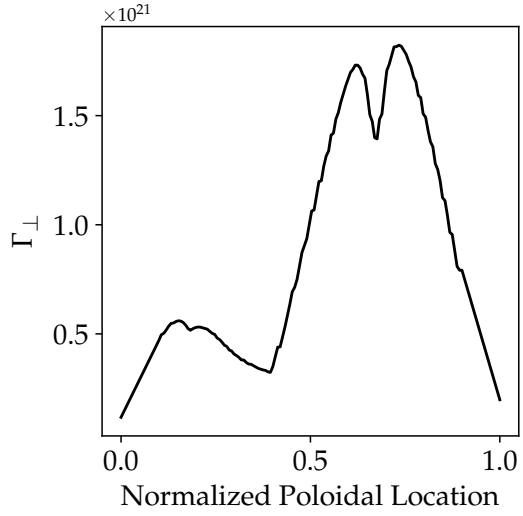

(c) $\Gamma_\perp$

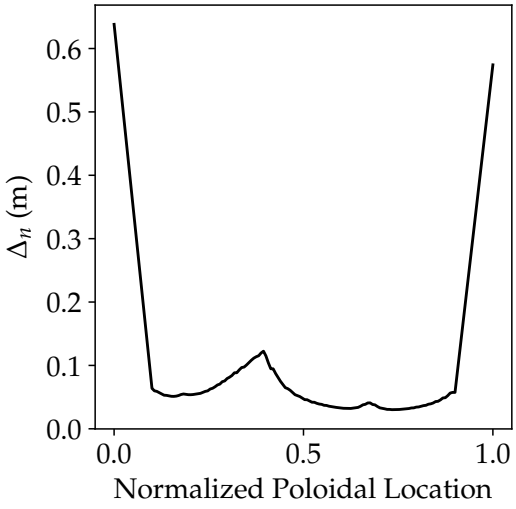

(d) Δ_n

Figure B.3: SOL density related quantities along the seperatrix going from the inboard strike point to the outboard strike point

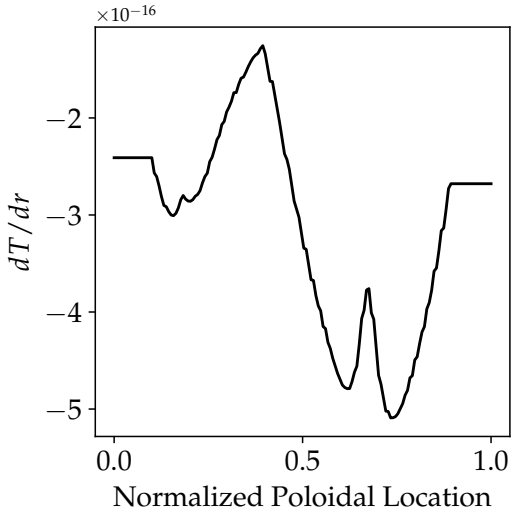

(a) dT_i/dr

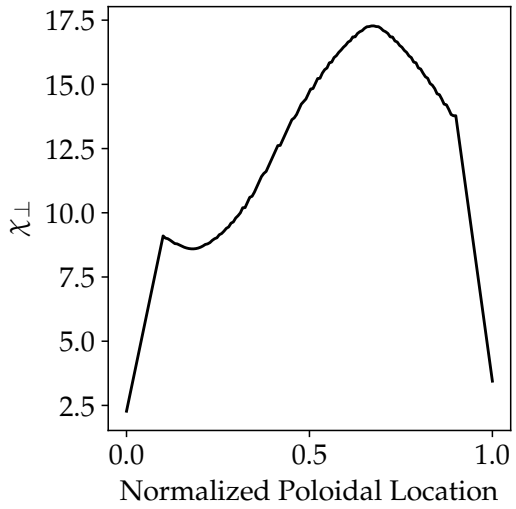

(b) $\chi_\perp$

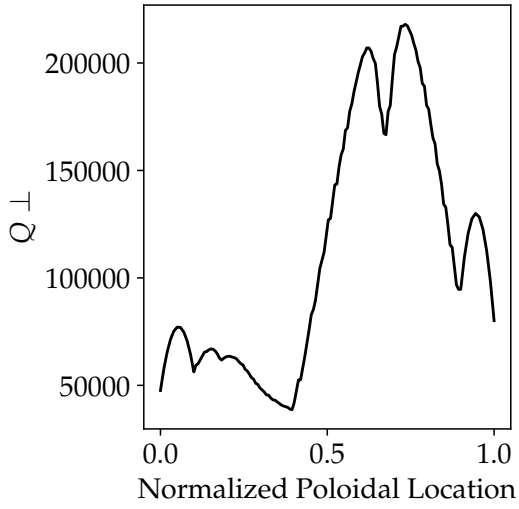

(c) $Q_\perp$

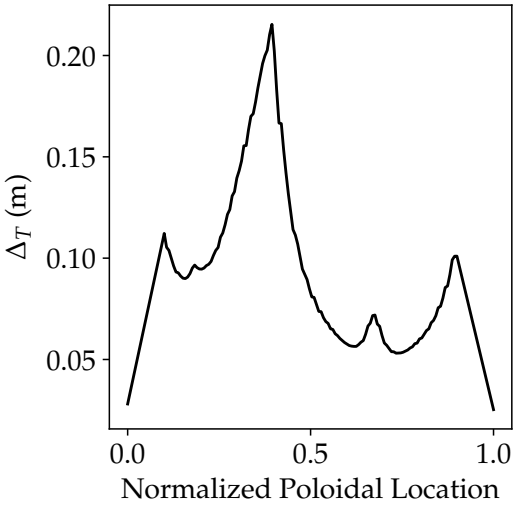

(d) Δ_T

Figure B.4: SOL temperature related quantities along the seperatrix going from the inboard strike point to the outboard strike point

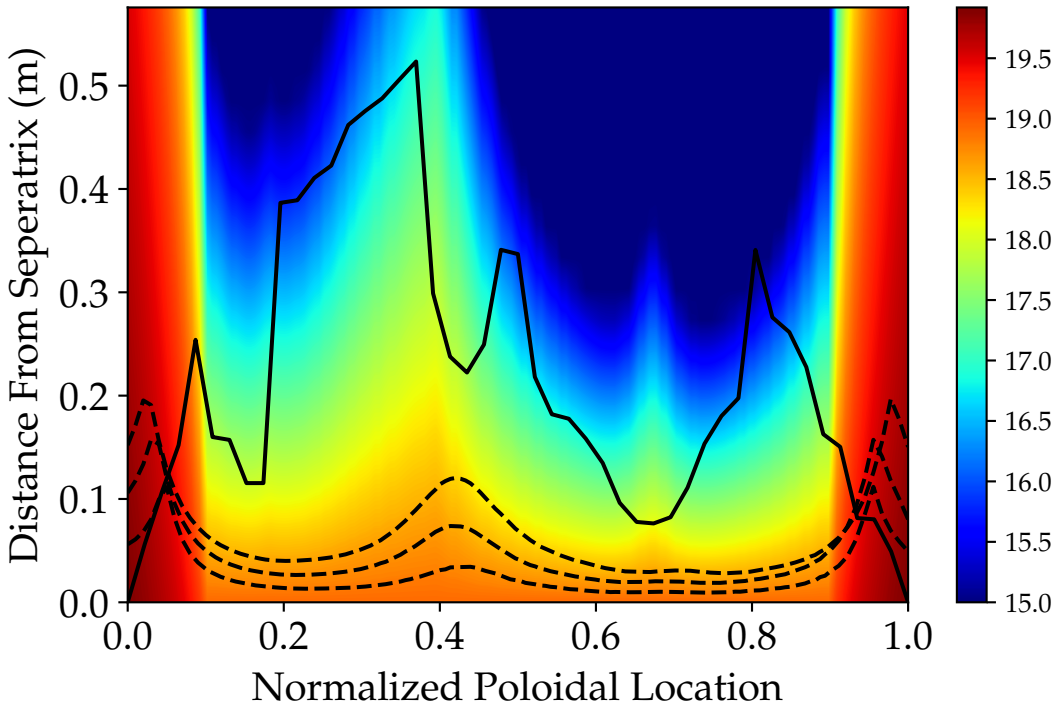

Figure B.5: A logscale color plot of the calculated ion density in the SOL. The solid line is the wall and the three dotted lines are the SOL flux surface lines. The numbers in the colorbar represent the exponent, i.e. 10^{19} m^{-3}.

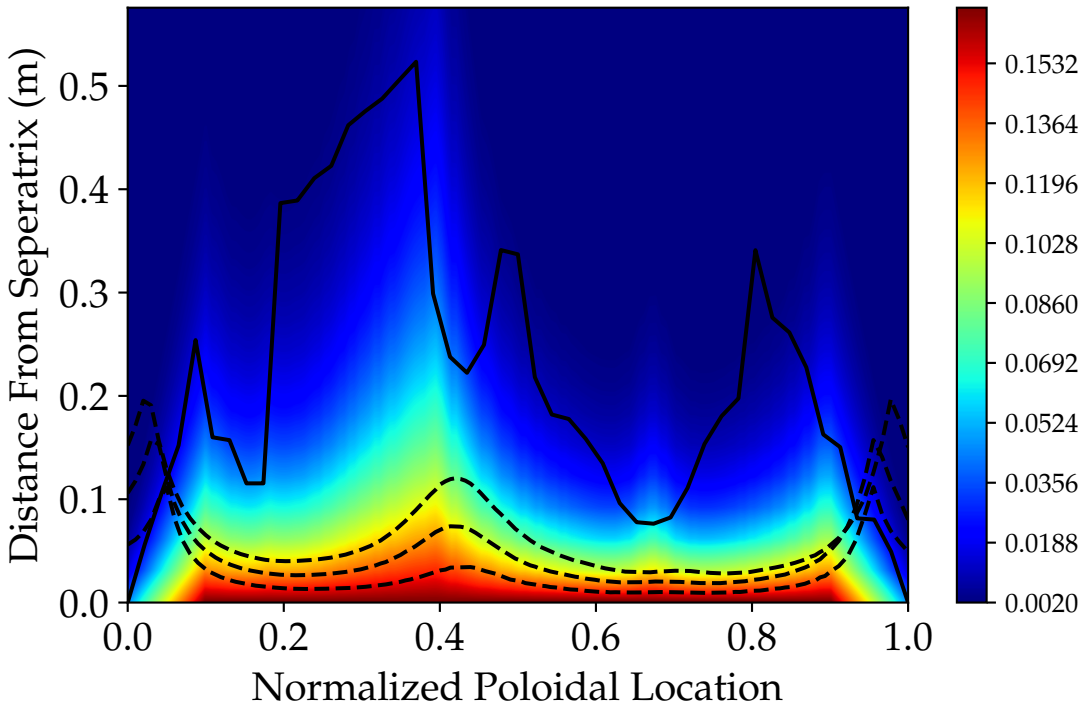

Figure B.6: A linear color plot of the calculated ion temperature (in keV) in the SOL in ITER. The solid line is the wall and the three dotted lines are the SOL flux surface lines.

A typical problem might have 50 θ locations, 20 launch angle cosines (ζ_0), and 100 radial locations. In such a problem, these arrays would contain $50\times20\times100\times50 = 5\times10^6$ elements. There are about 11 such arrays, so the machine would require about 0.4 GB of ram. Although this is quite manageable, memory can become a problem when instantiating GT3 several times or when using substantially more launch angle cosines or mesh points. Future improvements may be able to reduce the memory requirements of this module.

For an example of how to view IOL data stored in these arrays, suppose you wanted to view the minimum escape velocity $v_{\rm esc}$ for a particular launch angle cosine ($\zeta_0 = 0.55$, which is the 5$^{\rm th}$ most counter-current launch angle in the list of 20 that was used in the analysis below) for the parts of the plasma where such a quantity exists without regard to the exit location. You could obtain that data as illustrated in the following script, which includes examples of how to plot several useful lines like the first wall, the seperatrix, and inboard and outboard divertor legs. The resulting data are shown in Figure B.7.

It should be noted that although `calc_vsep(z, m, p)` in iol.py is used when calculating the radial loss profiles, it is also a module-level function that can easily be accessed and used outside of the IOL class. Its "`p`" argument requires the "`param`" attribute of the IOL class instance. "`z`" and "`m`" are the charge and mass (kg) of the species for which the escape velocity is being calculated. For deuterium, these are 1 and $3.343583719\times10^{-27}$ kg, respectively. The function returns a list of two arrays. The first is the full `v_sep` array. The second is the minimum velocity for any initial or final poloidal launch location as a function of ρ and ζ_0, which is useful for constructing radial loss profiles. In the example below, we must use the full `v_sep` array.

```
import numpy
import matplotlib.pyplot as plt
from matplotlib import rc
from gt3 import gt3
from iol import calc_vsep

# Use latex for generating text in plots.
rc('font', **{'family':'serif', 'serif':['Palatino']})
rc('text', usetex=True)

# specify input file and instantiate gt3
input_file = '/164436_3720/togt3_d3d_164436_3720'
shot = gt3(shotlabel=input_file, mode='iol')

# calculate the minimum energy necessary to reach any
# point on the seperatrix for every point in the plasma
z_d = 1
m_d = 3.343583719e-27
v_sep = calc_vsep(z_d, m_d, shot.iol.param)[0]
E_sep_kev = (0.5 * m_d * v_sep**2) / 1.6021E-19 / 1E3
E_sep_kev_min_sep = np.amin(E_sep_kev, axis=3)

fig = plt.figure(figsize=(10, 12))
ax1 = fig.add_subplot(1, 1, 1)
ax1.set_xlabel(r'$R$ (m)', fontsize=15)
ax1.set_ylabel(r'$Z$ (m)', fontsize=15)
ax1.tick_params(axis='both', which='major', labelsize=15)
ax1.axis('equal')
CS = ax1.contourf(shot.core.R,
                  shot.core.Z,
                  np.log10(E_sep_kev_min_sep[:, -5, :]).T,
                  500,
                  cmap='jet')
ax1.plot(np.asarray(shot.inp.wall_line)[:, 0],
         np.asarray(shot.inp.wall_line)[:, 1],
         color='black')
ax1.plot(np.asarray(shot.core.lines.sep_closed)[:, 0],
         np.asarray(shot.core.lines.sep_closed)[:, 1],
         color='black')
ax1.plot(np.asarray(shot.core.lines.div.ib)[:, 0],
         np.asarray(shot.core.lines.div.ib)[:, 1],
         color='black')
ax1.plot(np.asarray(shot.core.lines.div.ob)[:, 0],
         np.asarray(shot.core.lines.div.ob)[:, 1],
         color='black')
ax1.text(2.3, 1,
         r'$\zeta_0 = {}$'.format(shot.iol.coslist[-5]),
         fontsize=15)
fig.colorbar(CS)
```

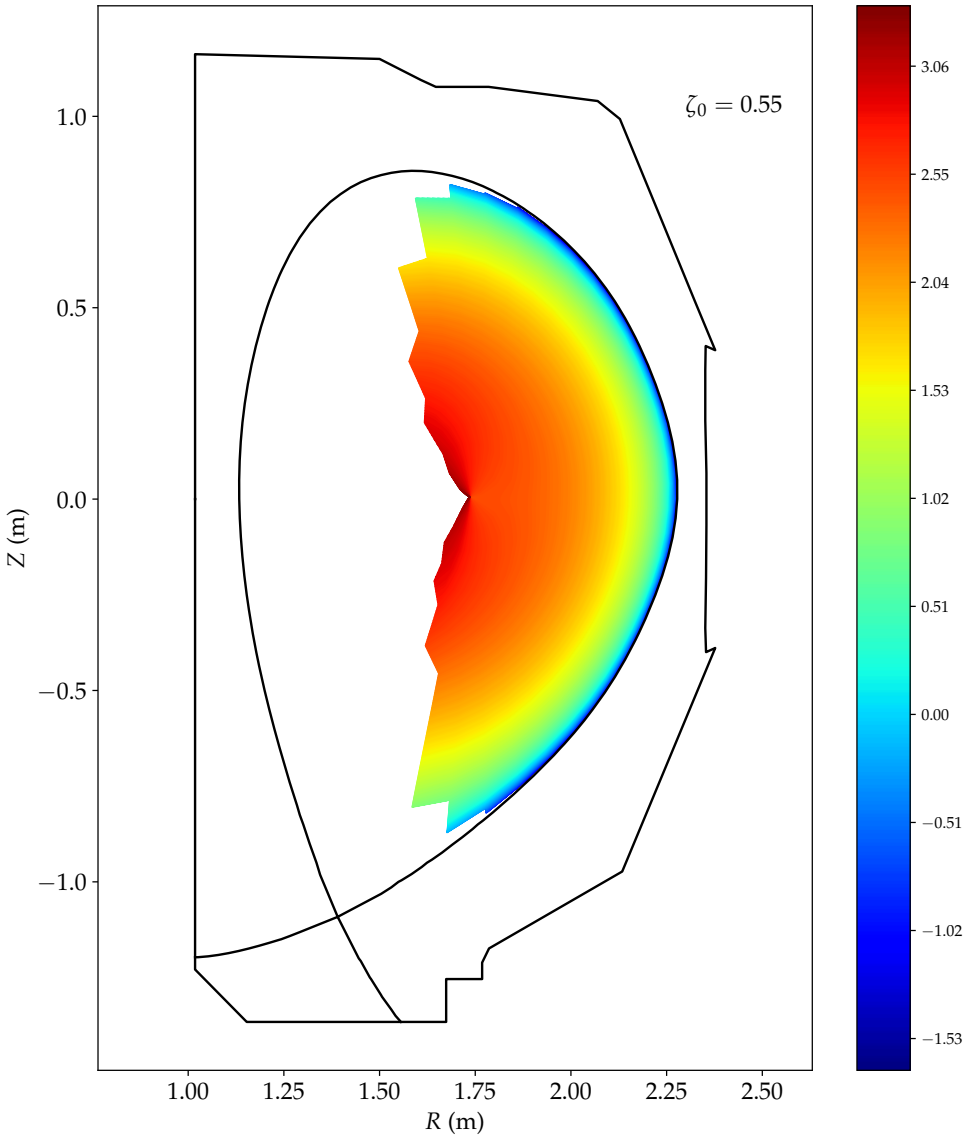

Figure B.7: A logscale plot of the minimum escape energy for deuterium for all launch points through any seperatrix point for the launch angle cosine $\zeta_0 = 0.55$

The colors in Figure B.7 are logscale. Although it shows that there is a mathematical solution for an escape velocity in the core, few particles exist with energies greater than $10^{0.5}$ anywhere in the plasma, and loss energies lower than that only exist in the edge, based on the color distribution. This is consistent with our general understanding of thermal IOL, which is that it only occurs in significant quantities in the edge. This chart gives us additional information, however. It shows that the particles for this particular launch angle cosine are only lost on the outboard side, and only in the edge. One obvious implication of this is that any intrinsic momentum resulting from IOL is likely not uniformly poloidally distributed. Analyses of the the effects of poloidal asymmetries on the toroidal momentum balance, such as have been ongoing at Georgia Tech for several years, may need to take this into account.

B.6 Impurity Calculations Using ADPAK Data

The ImpRad class in the impurity_radiation module serves a dual role in GT3. When the ImpRad class is instantiated, it first searches for a pickled interpolator object from which to get the necessary L_z and dL_z/dT data. Many of these pickled (`https://docs.python.org/3/library/pickle.html`) interpolator objects have already been created and are included in the github repository. Each are about 8.5 MB. In the unlikely event that the necessary interpolator object doesn't already exist, then ImpRad serves a wrapper for John Mandrekas's fortran wrapper for Russell Hulse's ADPAK routines. The class creates the inputs for the ADPAK wrapper, runs ADPAK, reads the results, and then performs the coronal equilibrium and other calculations as described in Chapter 4. The reason the pickled interpolator objects were created is because the amount of time required for ADPAK to run increases significantly with the z of the impurity element. High-z elements like tungsten can take several hours on a laptop. With the pickled interpolators, it takes virtually no time, regardless of the impurity species.

To use the pickled interpolaters manually, you must pass them the base-10 logarithms

of the neutral temperature in keV, the neutral fraction, and the electron temperature in keV in that order, as demonstrated in the script below for carbon. The resulting plot is shown in Figure B.8.

```
import numpy as np
import pickle
import matplotlib.pyplot as plt
from matplotlib import rc

# Use latex for generating text in plots.
rc('font', **{'family':'serif', 'serif':['Palatino']})
rc('text', usetex=True)

# import the pickle object
pkl_file_loc = 'Lz_interpolators/Carbon_Lz.pkl'
pickle_in = open(pkl_file_loc, "rb")
interp = pickle.load(pickle_in)
pickle_in.close()

# populate electron temperature array
Te_kev = np.logspace(-3, 2, 100)

# fix neutral temperature at 2 eV
Tn_kev = np.full(Te_kev.shape, 0.002)

# initialize figure
fig = plt.figure(figsize=(6, 4))
ax1 = fig.add_subplot(1, 1, 1)
ax1.set_xlabel(r'Electron Temperature (keV)',
               fontsize=15)
ax1.set_ylabel(r'$L_z$ (W$\cdot$m\textsuperscript{{3}})',
               fontsize=15)
ax1.tick_params(axis='both', which='major', labelsize=15)
# plot Lz(T) for several neutral fractions with Tn = 2 eV
for i,v in enumerate(np.logspace(-5,-1,5)):
    nf = np.full(Te_kev.shape, v)
    ax1.loglog(Te_kev,
               interp(np.log10(Tn_kev),
                      np.log10(nf),
                      np.log10(Te_kev)),
               label='nf = {}'.format(nf[0]))

# reverse the order of the legend
handles, labels = ax1.get_legend_handles_labels()
ax1.legend(handles[::-1], labels[::-1])
plt.tight_layout()
plt.show()
```

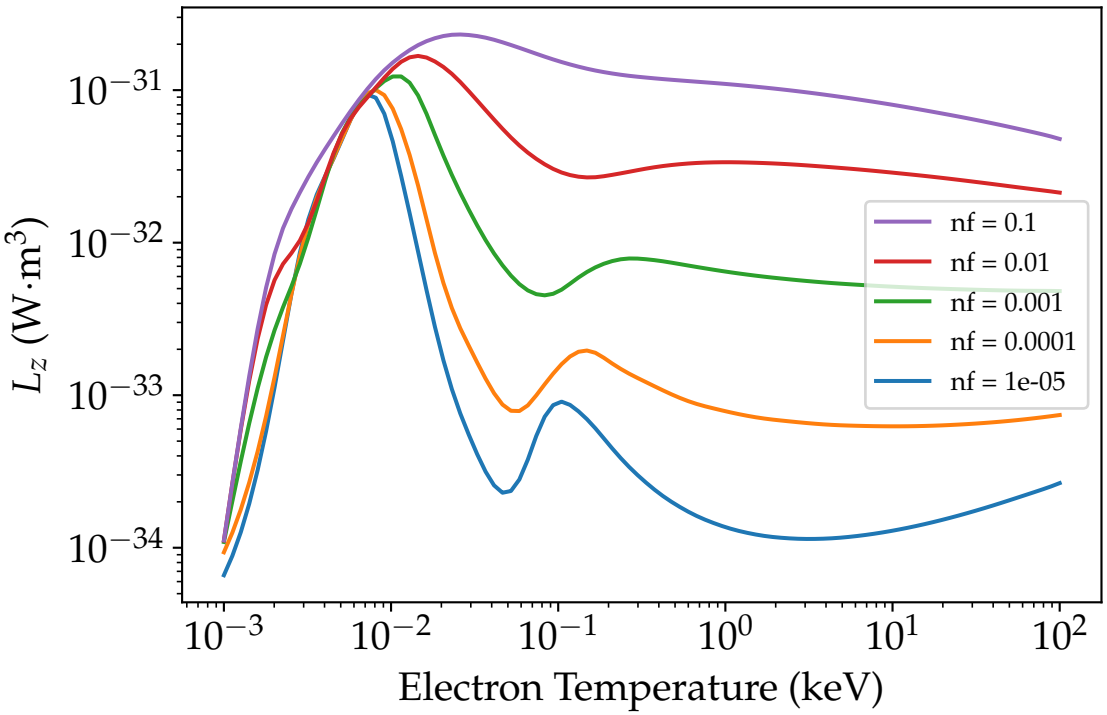

Figure B.8: L_z for Carbon over a range of temperatures and for several neutral fractions. This was calculated using GT3 and ADPAK impurity data, via the pickled carbon L_z interpolator available in the GT3 github repository.

B.7 Interfacing with Neutpy and NeutpyTools

It was decided early on in the development of neutpy that it should be a standalone code, separate from GT3, because it could easily be used for neutral transport calculations in non-tokamak situations. The purpose of the neutpy_prep module is to construct the input data for Triangle [88], generate the computational mesh using triangle, assemble the other data needed by Neutpy, run Neutpy, output the results to an output file, and interpolate the results onto the main GT3 computational grid. If a neutrals data file is specified in the main GT3 input file, then all of those steps are skipped and the data are simply read in and interpolated onto the GT3 grid. An example of the triangulated cell structure generated by Triangle is shown in Figure B.9.

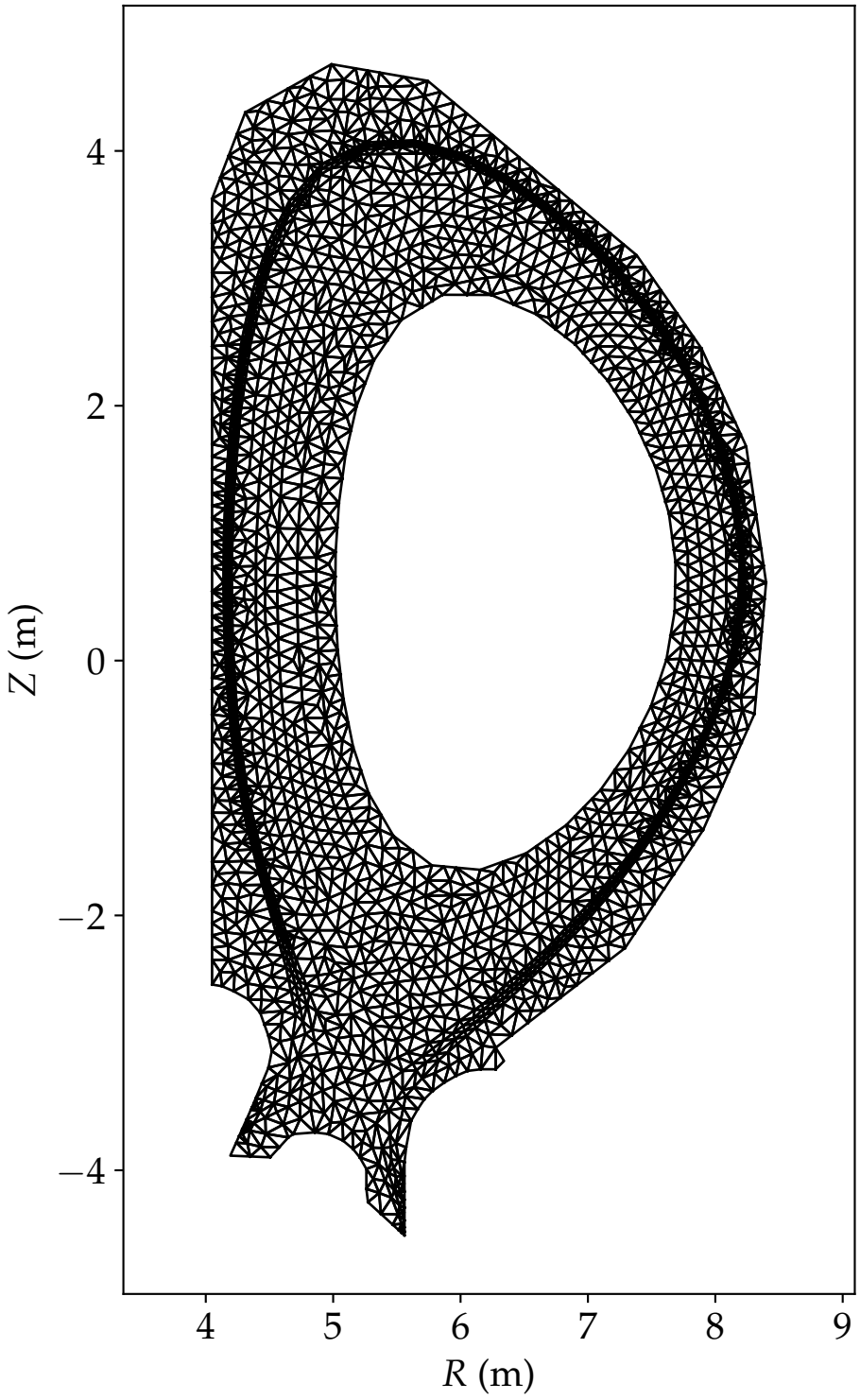

Figure B.9: An example of Triangle-generated mesh of ITER for use in Neutpy.

APPENDIX C

IMPROVED NEUTRAL DENSITY CALCULATIONS WITH NEUTPY

Neutpy is a python implementation of the two-group transmission escape probability (TEP) neutral transport methodology previously used in the GTNEUT code. Neutpy calculates neutrals densities and ionization rates everywhere in the plasma chamber using any of several cross section libraries. It improves upon GTNEUT in several ways, including improved treatment of uncollided neutrals, more accurate calculations of transmission coefficients, improved sparse matrix solving capabilities, and in the general structure and readability of the code. Although designed to be used as a standalone code, tokamak calculations are most easily accomplished by using it in conjunction with GT3, which generates the inputs required by neutpy. Neutpy is written in python and available from the FRC's github page: `https://github.com/gt-frc/neutpy`

C.1 Theory Overview

Most of the transport calculations in Neutpy are very similar to those in GTNEUT, which are described in great detail in the literature. [95, 96, 97] This section will only give a relatively brief overview of the transport theory involved.

The transport equations are written in terms of the partial currents (loosely referred to as "fluxes" in the code) through the sides of each cell. The flux Γ from cell i into an adjacent cell j can be written in terms of the angular flux $\psi\left(\mathbf{r}, \mathbf{\Omega}\right)$ as

$$\Gamma_{i,j} \equiv \int\limits_{S_{i,j}} dS \int\limits_{\mathbf{\Omega}\cdot\hat{\mathbf{n}}>0} d\mathbf{\Omega}\left(\mathbf{\Omega}\cdot\hat{\mathbf{n}}\right)\psi\left(\mathbf{r}_{i,j}, \mathbf{\Omega}\right) \tag{C.1}$$

where $S_{i,j}$ is the interface between cells i and j, $\hat{\mathbf{n}}$ is the normal unit vector at that interface (pointing away from cell i), and $\psi\left(\mathbf{r}_{i,j}, \mathbf{\Omega}\right)$ is the angular flux of the neutrals at $\mathbf{r}_{i,j}$.

The flux from cell i into cell j can be written as the sum of the fluxes from each side of the cell k (including cell j) times the probability that a particle entering through side k will exit the cell through $S_{i,j}$. Considering only the flux of neutrals that did not experience a collision in cell i, we can write this as

$$\Gamma^u_{i,j} = \sum_k \Gamma_{k,i} T^i_{k,j} \tag{C.2}$$

where the transmission coefficient from k to j via i, $T^i_{k,j}$ is equal to [95]

$$T^i_{k,j} = \frac{2}{\pi L_{ki}} \int_0^{L_{ki}} d\xi_{ki} \int_{\phi_{\min}(\xi_{ki})}^{\phi_{\max}(\xi_{ki})} d\phi \sin(\phi) K_{i,3} \left\{ \frac{l_i \left[\phi\left(\xi_{ki}\right)\right]}{\lambda_i} \right\} \tag{C.3}$$

Here, L_{ki} is the length of the interface between regions k and i, $\xi_{k,i}$ is the coordinate along the L_{ki} interface, l_i is the length of the distance travelled by the neutral in the 2D plane from a point ξ_{ki} on the entering surface to a point on the exiting surface along an angle ϕ relative to the entering surface, λ_i is the total mean free path (mfp) of the particle in cell i and $K_{i,3}$ is the third-order Bickley-Naylor function [95] given by

$$K_{i,n}(\tau) = \int_0^{\pi/2} d\theta \sin^{n-1}(\theta) \exp\left(\frac{-\tau}{\sin(\theta)}\right) \tag{C.4}$$

The collided flux can similarly be written as

$$\Gamma^u_{i,j} = \sum_k \Gamma_{k,i} \left(1 - \sum_l T^i_{k,l}\right) c_i P_i \Lambda_{ij} \tag{C.5}$$

where $\left(1 - \sum_l T^i_{k,l}\right)$ is the total fraction of the flux $\Gamma_{k,i}$ that experiences a collision in cell i, c_i is the fraction of particle collisions that do not remove the neutral from the system, P_i is the probability that a collided neutral born in cell i will escape, and Λ_{ij} is the probability that an escaping neutral will escape into cell j.

The number of secondary neutrals per collision, c_i can be calculated as the ratio of all the cross sections that will not remove a particle from the system to the sum of all interaction cross sections that are used in the calculation of λ_i. The charge exchange cross section must be treated carefully when modeling two energy groups, because although a charge exchange event does not remove a neutral from the system, it can remove one from a slower energy group and effectively move it to a higher energy group.

The escape probability P_i is calculated as

$$P_i = P_{0i} \sum_{n=0}^{\infty} \left[c_i \left(1 - P_{0i}\right)\right]^n = \frac{P_{0i}}{1 - c_i \left(1 - P_{0i}\right)} \tag{C.6}$$

The first flight escape probability P_{0i} is calculated as

$$P_{0i} = \frac{1}{X_i} \left[1 - \left(1 + \frac{X_i}{n}\right)^{-n}\right] \tag{C.7}$$

where

$$X_i = \frac{4V_i}{\lambda_i S_i} \tag{C.8}$$

with V_i being the volume of the cell in 3D or the surface area in 2D, S_i being the total surface area of the cell in 3D or perimeter in 2D. n = 2.09 is a value taken from Monte Carlo simulations. For more detailed information on the calculation of these parameters, please see Reference [95].

In addition to the flux contributions from collided and uncollided neutrals that streamed into cell i, we must also consider the flux contribution from neutrals born in cell i through recombination. This source can be written as

Writing equations for $\Gamma_{i,j}$ in terms of the other fluxes entering the cell and cell properties allows us to write a system of equations that is readily solvable. Because fluxes are only directly determined by a small number of other fluxes, almost all entries in the matrix will be zero, Sparse matrix solvers can cut down on the memory requirements, as the ma-

trix can become rather large otherwise. The right hand side of the system consists of the sources that do not depend on fluxes entering the cell. These are the contributions from ion recombination, gas puffing, wall out-gassing, etc. The source from recombination can be calculated as

$$\Gamma^s_{i,j} = S^i_{\mathrm{rec}} \left[P_{0i} \Lambda^s_{ij} + (1 - P_{0i} c_i P_i \Lambda_{ij}) \right] \tag{C.9}$$

C.2 Summary of Differences between GTNEUT and Neutpy

1. Neutpy is written in one python module consisting of about 1600 lines of code. By contrast, GTNEUT consisted of over 5000 lines of Fortran 77 code in over 30 files.

2. GTNEUT used a rather ancient sparse matrix solver that was often mentioned[61] as a source of problems. Neutpy uses much more modern and advanced sparse matrix solvers.

3. The accuracy of the transmission coefficient calculation is improved in Neutpy. The impetus for creating Neutpy in the first place was the unreliability of GTNEUT, which was likely the result of the limitations of integration scheme used for calculating the transmission coefficients.

4. Neutpy solves for both slow and thermal fluxes everywhere in the problem space. GTNEUT assumed that the slow particles emitted from the wall experienced a collision within the first wall-adjacent cell they entered into and joined the thermal group. This is a reasonable approximation when wall-adjacent cells are large, but could effect the accuracy of the results when cells are smaller. Typical GTNEUT input files were constructed at least partially by hand and the halo region was often divided into large regions. This is no longer the case because the mesh generation is done using constrained, conforming Delauney triangulation.

5. The improved approach to integration in neutpy make it much more reliable, but come at the cost of increased run times. Several strategies have been developed for

speeding the code up and will be explored in the future. At present, it takes about 30 minutes to run neutpy on a DIII-D shot, although this can vary somewhat with the choice of parameters.

C.3 Data Visualization using NeutpyTools

NeutpyTools is a module included with Neutpy that makes several Neutpy-related tasks simple, including generating cell and interface output files, plotting cell quantities, cell mesh structure, and flow visualizations such as the one shown in Figure C.1. NeutpyTools was created to help keep the Neutpy codebase clean. Virtually all data processing and plotting occurs outside of Neutpy using Neutpy's outputs.

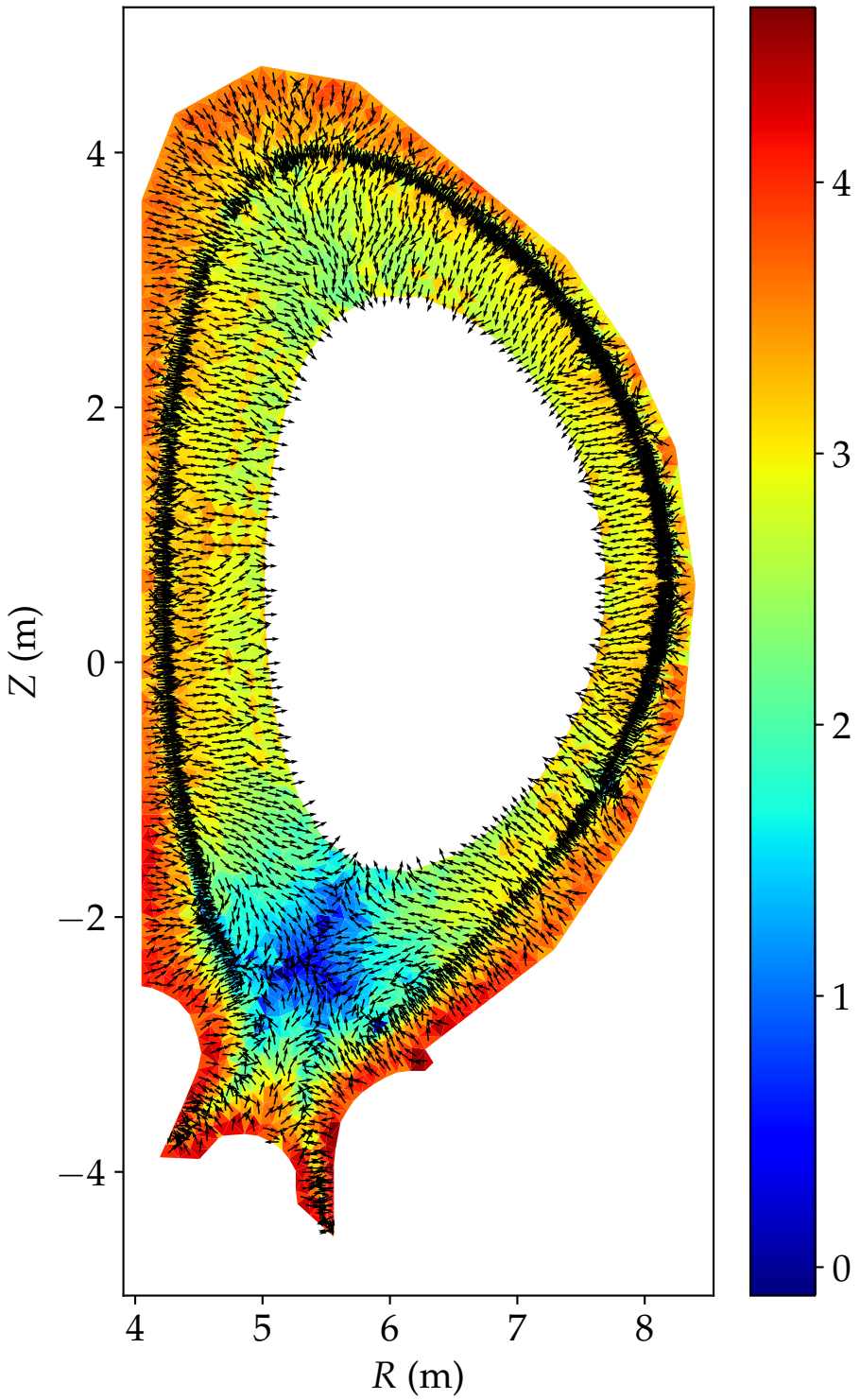

Figure C.1: An illustration of calculated neutral flow direction (arrows) and magnitude (color). This was generated using NeutpyTools for an ITER Neutpy calculation.

APPENDIX D
EXTENDING THE MILLER FLUX SURFACE MODEL INTO THE X-POINT REGION

D.1 Introduction and Miller Model Overview

Although primarily intended to parameterize experimental flux surfaces calculated by Grad-Shafranov solvers like EFIT [98], the Miller model can also be used to synthesize flux surface geometry and ψ values. By specifying a relatively small number of parameters (elongation (κ), triangularity (δ), etc.), and a background density and temperature distribution, we can map r, θ space into R, Z space and calculate $\psi\left(R,Z\right)$. The mappint of r, θ to R, Z is done using

$$R = R_0\left(r\right) + r\cos\left\{\theta + \left[\sin^{-1}\delta\left(r\right)\right]\sin\left(\theta\right)\right\} \tag{D.1}$$

$$Z = \kappa\left(r\right) r\sin\theta \tag{D.2}$$

It is important to note that R_0, κ, and δ are all functions of r. $R_0\left(r\right)$ includes the effect of the Shafranov shift [58, 8].

D.2 Extended Miller Parameterization

The Miller model seperatrix can be extended into the x-point region by modifying the equations for elongation and triangularity to include a poloidally dependence, as shown in Equations D.3 and D.4.

$$\kappa = \kappa\left(r\right) + \widetilde{\kappa}\left(r,\theta\right) \tag{D.3}$$

$$\delta = \delta\left(r, \theta\right) \tag{D.4}$$

In practice, it is often not necessary to include the poloidal dependence of the triangularity to get a reasonable fit to flux surfaces.

D.2.1 Modification of κ

At the seperatrix, $\widetilde{\kappa}$ should be chosen to approximately "fill in" the difference between a Miller equilibrium seperatrix and the correct seperatrix.

The discrepancy can be represented reasonably well using a function of the form shown in Equation D.5,

$$f\left(x\right) = C\left(1 - \left|x\right|^{\gamma 1}\right)^{\gamma 2} \tag{D.5}$$

in which $x \in [-1, 1]$, C is a scaling factor, and $\gamma 1$ and $\gamma 2$ control the concavity and shape of the function. Changing variables from x to $\theta \in [\pi, 2\pi]$ and allowing for different values of $\gamma 1$ and $\gamma 2$ on either side of the peak to better control the shape of the seperatrix yields

$$\widetilde{\kappa}_{\text{sep}} = \begin{cases} \Delta_{\kappa}\left(1 - \left|\frac{2\theta}{\pi} - 3\right|^{\gamma 1,in}\right)^{\gamma 2,in} & \pi < \theta < \theta_{\text{xpt}} \\ \Delta_{\kappa}\left(1 - \left|\frac{2\theta}{\pi} - 3\right|^{\gamma 1,out}\right)^{\gamma 2,out} & \theta_{\text{xpt}} \leq \theta < 2\pi \end{cases} \tag{D.6}$$

where Δ_{κ} is the scaling factor necessary for the peak of the function to extend to the vertical position of the x-point, i.e.,

$$\Delta_{\kappa} = \frac{Z_{\text{xpt}}}{a\sin\left(\theta_{\text{xpt}}\right) - \kappa_{\text{miller}}\left(a\right)} \tag{D.7}$$

In mathematics, mollification is the process of smoothing a function by convolving it with a smoothing convolution kernel called a "mollifier." In our case, we wish to smooth the $\widetilde{\kappa}_{\text{sep}}$ and $\widetilde{\delta}_{\text{sep}}$ functions such that the resulting function approximates the necessary modification to κ and δ to represent the shape of an internal flux surface.

There are several potential mollifying functions that one can choose from. Several of the most common are shown in Table D.1. Each results in slightly different flux surface shapes. In this paper, we have chosen to use the "Standard Bump" kernel because of its familiarity, despite the fact that it requires the convolution operation to be performed numerically.

Table D.1: Convolution Kernels That Could be Used with the X-Miller Model

Kernel Name	Base Convolution Kernel $\eta_0(x)$	Domain	Evaluated Analytically
Standard Bump	$C exp\left(\frac{-1}{1-x^2}\right)$ $C = \int_{-\infty}^{\infty} exp\left(\frac{-1}{1-x^2}\right) \approx 2.25$	$\|x\| < 1$	No
Epanechnikov	$\frac{3}{4}(1-x^2)$	$\|x\| < 1$	Yes
Triangular	$1 - \|x\|$	$\|x\| < 1$	Yes
Fejer	$\frac{1-cos(nx)}{n[1-cos(x)]}$	$\|x\| < \frac{\pi}{2}$	No
Tri-cube	$\frac{70}{81}\left(1-\|x^3\|\right)^3$	$\|x\| < 1$	Yes
Moving Average	$\frac{1}{2}$	$\|x\| < 1$	Yes

Implementing a radially dependent convolution kernel

For flux surfaces, the localization of smoothing resulting from the convolution should vary with r such that the contours smoothly approach the seperatrix. Additionally, the flux surfaces need to be increasing (i.e. not crossing).

To accomplish this, we first define a parameter ϵ as shown in Equation D.8 that modifies the base convolution kernel $\eta_0(x)$ as shown in Equation D.9. This narrows the mollifying

function and allows us to control how rounded or "pointy" the resulting function is.

$$\epsilon\left(r\right) = 1 - \left(\frac{r}{a}\right)^{\nu} \tag{D.8}$$

$$\eta_{\epsilon}\left(x\right) = \frac{1}{\epsilon\left(r\right)}\eta_{0}\left(\frac{x}{\epsilon\left(r\right)}\right) \tag{D.9}$$

The second modification is to scale the convolution kernel by a factor λ that sets the height of the bump function equal to the height of the peak of κ_{sep} minus the classic miller model elongation. This must be at least monotonically increasing and can be fit by a parameter as shown in Equation D.10. This process should be done to guarantee that condition two is true.

$$\lambda = \left(\frac{r}{a}\right)^{\nu}\left(\frac{Z_{\text{xpt}}}{a\sin\left(3\pi/2\right)} - \kappa_{\text{miller}}\right) \tag{D.10}$$

This results in a final convolution kernel of the form shown in Equation D.11.

$$\eta_{\epsilon}\left(x\right) = \lambda\frac{1}{\epsilon\left(r\right)}\eta_{0}\left(\frac{x}{\epsilon\left(r\right)}\right) \tag{D.11}$$

The equation for $\widetilde{\kappa}\left(r,\theta\right)$ can now be written as shown in Equation D.12.

$$\widetilde{\kappa}\left(r,\theta\right) = \begin{cases} \kappa_{\text{sep}}\left(\theta\right) * \eta_{\epsilon}\left(x\right) & r < a \\ \kappa_{\text{sep}}\left(\theta\right) & r = a \end{cases} \tag{D.12}$$

Post-Convolution Corrections

The convolution operation gives the overall desired behavior, however, as shown in Figure D.1a, the endpoints of the smoothed functions are not identically zero at $\theta = \pi$ and $\theta = 3\pi/2$, which is necessary for $\kappa\left(r,\theta\right)$ to be continuous. There are two ways to solve this problem. The first is to subtract the straight line defined by the two endpoints from the

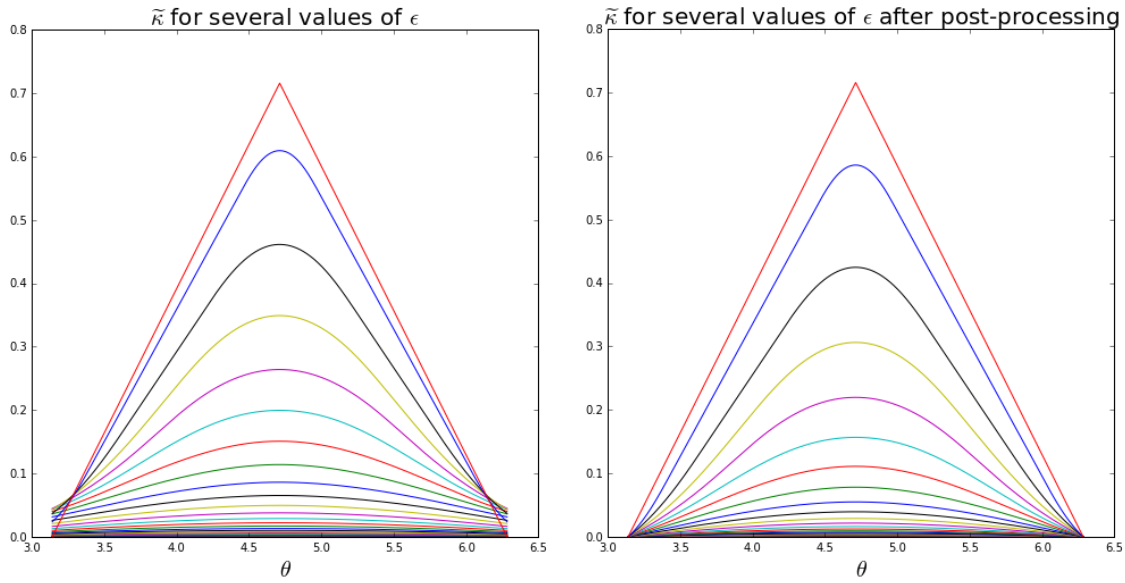

(a) $\widetilde{\kappa}$ before post processing

(b) $\widetilde{\kappa}$ after post processing as described by Equation D.13

Figure D.1: Plot of $\widetilde{\kappa}$ for several values of ϵ resulting from the convolution in Equation

entire function, i.e.

$$\widetilde{\kappa}\left(r,\theta\right)' = \widetilde{\kappa}\left(r,\theta\right) - H\left(r,\theta\right) \tag{D.13}$$

where

$$H\left(r,\theta\right) = \frac{\widetilde{\kappa}\left(r,2\pi\right) - \widetilde{\kappa}\left(r,\pi\right)}{\pi}\left(\theta - \pi\right) + \widetilde{\kappa}\left(r,\pi\right) \tag{D.14}$$

The results of this operation are shown in Figure D.1b

The second is to rescale θ variable for after convolution. The specifics of this recasting depend upon the specific domain of interest. In the case examined here, the rescaling can be accomplished using

$$\theta' = \theta(1 + \frac{2\epsilon}{\pi}) - 3\epsilon \tag{D.15}$$

Although the second of these approaches is perhaps more mathematically elegant, we have obtained better results using the first approach, in which a straight line is subtracted to ensure κ continuity at the inboard and outboard midplanes.

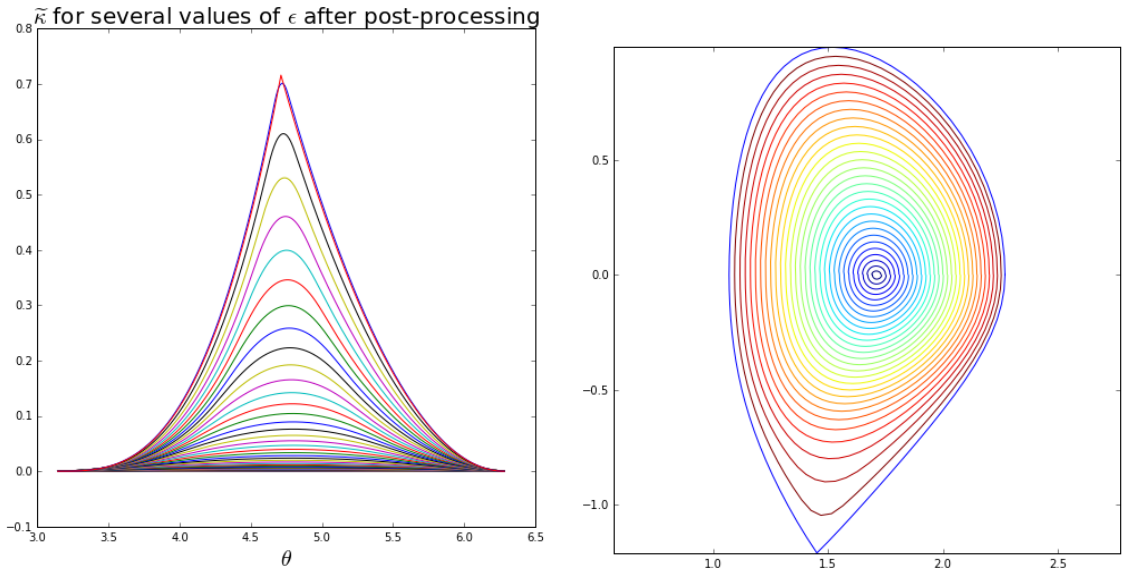

(a) Calculated B_p (b) Experimental B_p

Figure D.2: Comparison of Calculated and Experimental B_p

D.3 Triangularity Calculations

For the current implementation of this model, θ_{xpt} is set to $\theta_{\text{xpt}} = 3\pi/2$. The maximum value of the lower triangularity at $\theta = 3\pi/2$ is calculated such that the x-point is placed at the desired location, i.e.,

$$\delta_{\text{xpt}}\left(r = a, \theta = 3\pi/2\right) = \sin\left\{\cos^{-1}\left[\frac{R_{\text{xpt}} - R_0\left(a\right)}{a}\right] - \frac{3\pi}{2}\right\} \tag{D.16}$$

D.4 Flux Surfaces

After $\kappa\left(r, \theta\right)$ and $\delta\left(r, \theta\right)$ have been determined, the Shafranov shift and resulting flux surfaces can be calculated as in Miller et. al. An

D.5 Rederivation of $\vec{\nabla} r$

The poloidal field in the plasma can be calculated from

$$B_p = \frac{1}{R}\frac{\partial \psi}{\partial r}\left|\vec{\nabla} r\right| \tag{D.17}$$

Miller et al. calculated $\vec{\nabla} r$ based on the assumption that κ varied only with r. Because we have relaxed that assumption, a new form of $\vec{\nabla} r$ must be calculated as shown below.

$$\vec{\nabla} r = \frac{\frac{\partial Z}{\partial \theta} dR - \frac{\partial R}{\partial \theta} dZ}{\frac{\partial R}{\partial r}\frac{\partial Z}{\partial \theta} - \frac{\partial R}{\partial \theta}\frac{\partial Z}{\partial r}} = \frac{\sqrt{\frac{\partial Z}{\partial \theta}^2 + \frac{\partial R}{\partial \theta}^2}}{\frac{\partial R}{\partial r}\frac{\partial Z}{\partial \theta} - \frac{\partial R}{\partial \theta}\frac{\partial Z}{\partial r}} \hat{\mathbf{e}}_{\mathbf{r}} \tag{D.18}$$

Although analytical representations of these partial derivatives and the resulting equation for $\vec{\nabla} r$ can be obtained, it is typically much easier to differentiate numerically.

REFERENCES

[1] A. Einstein, "Does the inertia of a body depend upon its energy-content", *Annalen der Physik*, vol. 18, no. 13, pp. 639–641, 1905.

[2] V. D. Shafranov, B. Bondarenko, G. A. Goncharov, O. A. Lavrent'ev, A. D. Sakharov, *et al.*, "On the history of the research into controlled thermonuclear fusion", *Physics-Uspekhi*, vol. 44, no. 8, pp. 835–843, 2001.

[3] V. Smirnov, "Tokamak foundation in ussr/russia 1950–1990", *Nuclear fusion*, vol. 50, no. 1, p. 014 003, 2009.

[4] R. Mills, "I fundamental considerations for toroidal fusion reactors", *FUSION REACTOR DESIGN, JUNE 2-5, 1970*, p. 38, 1970.

[5] W. M. Stacey, M. Abdou, J. Brooks, I Charak, R. Clemmer, J Dawson, K Evans, J. Fasolo, R Fuja, S. Harkness, *et al.*, "Tokamak experimental power reactor", Argonne National Lab.(ANL), Argonne, IL (United States), Tech. Rep., 1977.

[6] I. Group *et al.*, "International tokamak reactor–phase i (executive summary of the iaea workshop, 1981)", *Nuclear Fusion*, vol. 22, no. 1, p. 135, 1982.

[7] ITER Organization. (2016). Iter council endorses updated project schedule, (visited on 09/09/2018).

[8] W. M. Stacey, *Fusion Plasma Physics*. John Wiley & Sons, 2012.

[9] I. Team *et al.*, "Iter physics basis", *Nucl. Fusion*, vol. 39, p. 2137, 1999.

[10] D. Humphreys, J. Ferron, M Bakhtiari, J. Blair, Y In, G. Jackson, H Jhang, R. Johnson, J. Kim, R. LaHaye, *et al.*, "Development of iter-relevant plasma control solutions at DIII-D", *Nuclear Fusion*, vol. 47, no. 8, p. 943, 2007.

[11] D. Post, K Borrass, and J. Callen, "Iter physics", 1991.

[12] J. Cordey, J. Snipes, and M Greenwald, "The scaling of confinement in iter with β and collisionality", Tech. Rep., 2005.

[13] M. Greenwald, J. Terry, S. Wolfe, S Ejima, M. Bell, S. Kaye, and G. Neilson, "A new look at density limits in tokamaks", *Nuclear Fusion*, vol. 28, no. 12, p. 2199, 1988.

[14] R. J. Hawryluk, “What will we learn from ITER?”, Conference Presentation, Sherwood Fusion Theory Conference, Auburn University, Auburn, Alabama, 2018.

[15] R. Mills, “The problem of control of thermonuclear reactors”, Princeton Univ., NJ Plasma Physics Lab., Tech. Rep., 1970.

[16] H.-S. Bosch and G. Hale, “Improved formulas for fusion cross-sections and thermal reactivities”, *Nuclear Fusion*, vol. 32, no. 4, p. 611, 1992.

[17] M. D. Hill and W. M. Stacey, “Confinement tuning of a 0-D plasma dynamics model”, *Fusion Science and Technology*, vol. 72, no. 2, pp. 162–175, 2017.

[18] S. Tamor, “Calculation of energy transport by cyclotron radiation in fusion plasmas”, *Nuclear Technology - Fusion*, vol. 3, no. 2, pp. 293–303, 1983. eprint: `https://doi.org/10.13182/FST83-A20853`.

[19] F Albajar, M Bornatici, G Cortes, J Dies, F Engelmann, J Garcia, and J Izquierdo, “Importance of electron cyclotron wave energy transport in iter”, *Nuclear Fusion*, vol. 45, no. 7, p. 642, 2005.

[20] R. Pitts, S Carpentier, F Escourbiac, T Hirai, V Komarov, S Lisgo, A. Kukushkin, A Loarte, M Merola, A. S. Naik, *et al.*, “A full tungsten divertor for iter: Physics issues and design status”, *Journal of Nuclear Materials*, vol. 438, S48–S56, 2013.

[21] T Casper, Y Gribov, A Kavin, V Lukash, R Khayrutdinov, H Fujieda, C Kessel, I. D. Agencies, *et al.*, “Development of the iter baseline inductive scenario”, *Nuclear Fusion*, vol. 54, no. 1, p. 013 005, 2013.

[22] A. C. Sips *et al.*, “Advanced scenarios for iter operation”, *Plasma physics and controlled fusion*, vol. 47, no. 5A, A19, 2005.

[23] K. Borrass, “Disruptive tokamak density limit as scrape-off layer/divertor phenomenon”, *Nuclear Fusion*, vol. 31, no. 6, p. 1035, 1991.

[24] J. R. Roth, *Introduction to fusion energy*. Classworks, 1986.

[25] F Albajar, M Bornatici, and F Engelmann, “Raytec: A new code for electron cyclotron radiative transport modelling of fusion plasmas”, *Nuclear Fusion*, vol. 49, no. 11, p. 115 017, 2009.

[26] F Albajar, J Johner, and G Granata, “Improved calculation of synchrotron radiation losses in realistic tokamak plasmas”, *Nuclear Fusion*, vol. 41, no. 6, p. 665, 2001.

[27] I. T. Basis, *Iter eda documentation series no. 24*, 2002.

[28] B. Trubnikov, "Magnetic emission of high temperature plasma", 1958.

[29] W. Drummond and M. Rosenbluth, "Cyclotron radiation from a hot plasma", *The Physics of Fluids*, vol. 6, no. 2, pp. 276–283, 1963.

[30] F. Albajar, M. Bornatici, and F. Engelmann, "Electron cyclotron radiative transfer in fusion plasmas", *Nuclear Fusion*, vol. 42, no. 6, p. 670, 2002.

[31] T. H. Stix, *Waves in plasmas*. Springer Science & Business Media, 1992.

[32] R. A. Hulse, "Numerical studies of impurities in fusion plasmas", *Nuclear Technology-Fusion*, vol. 3, no. 2, pp. 259–272, 1983.

[33] S. Hirshman and D. Sigmar, "Neoclassical transport of impurities in tokamak plasmas", *Nuclear Fusion*, vol. 21, no. 9, p. 1079, 1981.

[34] K Schmid, K Krieger, A Kukushkin, and A Loarte, "Divimp modeling of tungsten impurity transport in iter", *Journal of nuclear materials*, vol. 363, pp. 674–679, 2007.

[35] T. Fülöp and J. Weiland, "Impurity transport in iter-like plasmas", *Physics of plasmas*, vol. 13, no. 11, p. 112 504, 2006.

[36] R Dux, A Loarte, E Fable, and A Kukushkin, "Transport of tungsten in the h-mode edge transport barrier of iter", *Plasma Physics and Controlled Fusion*, vol. 56, no. 12, p. 124 003, 2014.

[37] G. Pacher, H. Pacher, G Janeschitz, and A. Kukushkin, "Iter operation window determined from mutually consistent core–sol–divertor simulations: Definition and application", *Nuclear Fusion*, vol. 48, no. 10, p. 105 003, 2008.

[38] R Dux and A. Peeters, "Neoclassical impurity transport in the core of an ignited tokamak plasma", *Nuclear fusion*, vol. 40, no. 10, p. 1721, 2000.

[39] S. Brezinsek, J.-E. contributors, *et al.*, "Plasma-surface interaction in the be/w environment: Conclusions drawn from the jet-ilw for iter", *Journal of nuclear materials*, vol. 463, pp. 11–21, 2015.

[40] R Dux, V Bobkov, A Herrmann, A Janzer, A Kallenbach, R Neu, M Mayer, H. Müller, R Pugno, T Pütterich, *et al.*, "Plasma-wall interaction and plasma behaviour in the non-boronised all tungsten asdex upgrade", *Journal of Nuclear Materials*, vol. 390, pp. 858–863, 2009.

[41] N Commaux, L. R. Baylor, T. C. Jernigan, E. Hollmann, P. Parks, D. Humphreys, J. Wesley, and J. Yu, "Demonstration of rapid shutdown using large shattered deuterium pellet injection in DIII-D", *Nuclear Fusion*, vol. 50, no. 11, p. 112 001, 2010.

[42] L. R. Baylor, P. Parks, T. C. Jernigan, J. B. Caughman, S. K. Combs, C. R. Foust, W. A. Houlberg, S Maruyama, and D. A. Rasmussen, "Pellet fuelling and control of burning plasmas in iter", *Nuclear Fusion*, vol. 47, no. 5, p. 443, 2007.

[43] T Petrie, "High performance double-null plasma operation under radiating mantle conditions on DIII-D", Conference Presentation, 59th Annual Meeting of the APS Division of Plasma Physics, Madison, Wisconsin, 2017.

[44] C. Maggi, R Dux, L. Horton, R Neu, D Nishijima, T Pütterich, A. Sips, B Zaniol, and A. U. Team, "Impurity control in improved h-mode scenarios in asdex upgrade", in *Europhysics Conference Abstracts (CD-ROM, Proc. of the 31st EPS Conference on Controlled Fusion and Plasma Physics, London, 2004)*, vol. 28, 2004.

[45] R Dux, R Neu, C. Maggi, A. Peeters, T Pütterich, G Pereverzev, A Mück, F Ryter, J Stober, and B Zaniol, "Impurity transport and control in asdex upgrade", ASDEX Upgrade Team, Tech. Rep., 2005.

[46] K Behringer, "Description of the impurity transport code'strahl'", Commission of the European Communities, Tech. Rep., 1987.

[47] T. Onjun and Y. Pianroj, "Simulations of iter with combined effects of internal and edge transport barriers", *Nuclear Fusion*, vol. 49, no. 7, p. 075 003, 2009.

[48] R. Budny, R Andre, G Bateman, F Halpern, C. Kessel, A Kritz, and D McCune, "Predictions of h-mode performance in iter", *Nuclear Fusion*, vol. 48, no. 7, p. 075 005, 2008.

[49] C. Angioni, A. Peeters, G. Pereverzev, A. Bottino, J Candy, R. Dux, E. Fable, T Hein, and R. Waltz, "Gyrokinetic simulations of impurity, he ash and α particle transport and consequences on iter transport modelling", *Nuclear Fusion*, vol. 49, no. 5, p. 055 013, 2009.

[50] A Kallenbach, M Bernert, R Dux, L Casali, T. Eich, L Giannone, A Herrmann, R McDermott, A Mlynek, H. Müller, *et al.*, "Impurity seeding for tokamak power exhaust: From present devices via iter to demo", *Plasma Physics and Controlled Fusion*, vol. 55, no. 12, p. 124 041, 2013.

[51] K. Miyamoto, "Direct ion orbit loss near the plasma edge of a divertor tokamak in the presence of a radial electric field", *Nuclear fusion*, vol. 36, no. 7, p. 927, 1996.

[52] W. M. Stacey, "Effect of ion orbit loss on the structure in the h-mode tokamak edge pedestal profiles of rotation velocity, radial electric field, density, and temperature", *Physics of Plasmas*, vol. 20, no. 9, p. 092 508, 2013.

[53] W. M. Stacey, "The effect of ion orbit loss and x-loss on the interpretation of ion energy and particle transport in the DIII-D edge plasma", *Physics of Plasmas*, vol. 18, no. 10, p. 102 504, 2011.

[54] W. Stacey, J. Boedo, T. Evans, B. Grierson, and R. Groebner, "Intrinsic rotation produced by ion orbit loss and x-loss", *Physics of Plasmas*, vol. 19, no. 11, p. 112 503, 2012.

[55] T. Wilks, W. Stacey, and T. Evans, "Calculation of the radial electric field from a modified ohm's law", *Physics of Plasmas*, vol. 24, no. 1, p. 012 505, 2017.

[56] T. Wilks and W. Stacey, "Improvements to an ion orbit loss calculation in the tokamak edge", *Physics of Plasmas*, vol. 23, no. 12, p. 122 505, 2016.

[57] W. Stacey, "Extended fluid transport theory in the tokamak plasma edge", *Nuclear Fusion*, vol. 57, no. 6, p. 066 034, 2017.

[58] R. Miller, M. Chu, J. Greene, Y. Lin-Liu, and R. Waltz, "Noncircular, finite aspect ratio, local equilibrium model", *Physics of Plasmas*, vol. 5, no. 4, pp. 973–978, 1998.

[59] F. Wagner, G Becker, K Behringer, D Campbell, A Eberhagen, W Engelhardt, G Fussmann, O Gehre, J Gernhardt, G. v. Gierke, *et al.*, "Regime of improved confinement and high beta in neutral-beam-heated divertor discharges of the asdex tokamak", *Physical Review Letters*, vol. 49, no. 19, p. 1408, 1982.

[60] B Lipschultz, B LaBombard, E. Marmar, M. Pickrell, J. Terry, R Watterson, and S. Wolfe, "Marfe: An edge plasma phenomenon", *Nuclear Fusion*, vol. 24, no. 8, p. 977, 1984.

[61] Z. Friis, "An examination of the effects of neutral particles on the edge plasma in tokamaks", PhD thesis, Georgia Institute of Technology, May 2010.

[62] W. Stacey, Z. Friis, T. Petrie, and A. Leonard, "Investigation of the cause of the high-to-low mode confinement transition following multifaceted asymmetric radiation from edge formation in diii-d", *Physics of plasmas*, vol. 12, no. 7, p. 072 518, 2005.

[63] A. Leonard, W. Meyer, B Geer, D. Behne, and D. Hill, "2d tomography with bolometry in diii-da", *Review of scientific instruments*, vol. 66, no. 2, pp. 1201–1204, 1995.

[64] T. Carlstrom, G. Campbell, J. DeBoo, R Evanko, J Evans, C. Greenfield, J Haskovec, C. Hsieh, E McKee, R. Snider, *et al.*, "Design and operation of the multipulse thomson scattering diagnostic on diii-d", *Review of scientific instruments*, vol. 63, no. 10, pp. 4901–4906, 1992.

[65] D. W. Ross, "Critique of atomic physics instability mechanisms: Ionization-driven and radiative microinstabilities in the tokamak edge plasma", *Physics of plasmas*, vol. 1, no. 8, pp. 2630–2636, 1994.

[66] X. Chen, B. Shi, and Q. Gao, "Multifaceted asymmetric radiation from the edge: A strong condensation phenomenon", *Physics of Plasmas*, vol. 3, no. 12, pp. 4507–4512, 1996.

[67] M. Tokar, J Rapp, D Reiser, U Samm, F. Schüller, G Sergienko, and P. de Vries, "Localized recycling as a trigger of marfe", *Journal of nuclear materials*, vol. 266, pp. 958–962, 1999.

[68] M. Tokar, W Biel, J Rapp, D Reiser, U Samm, and G Sergienko, "Study of the relevance of thermal instability caused by impurity radiation to marfe development in a limiter tokamak", *Contributions to Plasma Physics*, vol. 42, no. 2-4, pp. 290–295, 2002.

[69] M. Tokar and F. Kelly, "The role of plasma–wall interactions in thermal instabilities at the tokamak edge", *Physics of Plasmas*, vol. 10, no. 11, pp. 4378–4386, 2003.

[70] F. Kelly and M. Tokar, "Theoretical study of the effect of the dynamic ergodic divertor on marfe onset", *Contributions to Plasma Physics*, vol. 44, no. 1-3, pp. 176–181, 2004.

[71] U Samm, M Brix, F Durodié, M Lehnen, A Pospieszczyk, J Rapp, G Sergienko, B Schweer, M. Tokar, and B Unterberg, "Marfe feedback experiments on textor-94", *Journal of nuclear materials*, vol. 266, pp. 666–672, 1999.

[72] W. Stacey, "A survey of thermal instabilities in tokamak plasmas: Theory, comparison with experiment, and predictions for future devices", *Fusion Science and Technology*, vol. 52, no. 1, p. 29, 2007.

[73] W. M. Stacey, "Explanation for marfe formation and subsequent evolution into a detached symmetric plasma edge", *Physics of Plasmas*, vol. 3, no. 7, pp. 2673–2678, 1996.

[74] W. M. Stacey, "Thermal stability of the tokamak plasma edge", *Plasma physics and controlled fusion*, vol. 39, no. 8, p. 1245, 1997.

[75] W. M. Stacey, "Density limits for multifaceted asymmetric radiation from the edge", *Fusion technology*, vol. 36, no. 1, pp. 38–46, 1999.

[76] W. Stacey, M. Mahdavi, R Maingi, and T. Petrie, "Multi-faceted asymmetric radiation from the edge formation in diii-d high-confinement mode discharges with continuous gas puffing", *Physics of Plasmas*, vol. 6, no. 10, pp. 3941–3954, 1999.

[77] W. M. Stacey and T. Petrie, "The role of thermal instabilities in limiting the density in diii-d", *Physics of Plasmas*, vol. 7, no. 12, pp. 4931–4941, 2000.

[78] W. M. Stacey, E. Thomas, and T. Evans, "Data and extended diffusion theories for neutral particle transport in tokamak divertors", *Physics of Plasmas*, vol. 2, no. 10, pp. 3740–3756, 1995.

[79] A. T. Bopp and W. M. Stacey, "Dynamic safety analysis of a subcritical advanced burner reactor", *Nuclear Technology*, vol. 200, no. 3, pp. 250–268, 2017.

[80] P. a. Sonato, P Agostinetti, G Anaclerio, V Antoni, O Barana, M Bigi, M Boldrin, M Cavenago, S Dal Bello, M Dalla Palma, *et al.*, "The iter full size plasma source device design", *Fusion Engineering and Design*, vol. 84, no. 2-6, pp. 269–274, 2009.

[81] M. Gouge, K. S. Onge, S. Milora, P. Fisher, and S. Combs, "Pellet fueling system for iter", *Fusion Engineering and Design*, vol. 19, no. 1, pp. 53–72, 1992.

[82] S. K. Combs, L. R. Baylor, S. J. Meitner, J. Caughman, D. A. Rasmussen, and S. Maruyama, "Overview of recent developments in pellet injection for iter", *Fusion Engineering and Design*, vol. 87, no. 5-6, pp. 634–640, 2012.

[83] L. Guazzotto and R. Betti, "From lawson to burning plasmas: A multi-fluid approach", in *APS Meeting Abstracts*, 2017.

[84] M. D. Boyer and E. Schuster, "Nonlinear burn control in tokamak fusion reactors via output feedback", in *Proc. 19th World Congress of the International Federation of Automatic Control (Cape Town, South Africa,)*, 2014.

[85] W. Heidbrink and G. Sadler, "The behaviour of fast ions in tokamak experiments", *Nuclear Fusion*, vol. 34, no. 4, p. 535, 1994.

[86] W. Heidbrink, "Alpha particle physics in a tokamak burning plasma experiment", *Physics of Plasmas*, vol. 9, no. 5, pp. 2113–2119, 2002.

[87] G. Matthews, M Beurskens, S Brezinsek, M Groth, E Joffrin, A Loving, M Kear, M. Mayoral, R Neu, P Prior, *et al.*, "Jet iter-like wall—overview and experimental programme", *Physica Scripta*, vol. 2011, no. T145, p. 014 001, 2011.

[88] J. R. Shewchuk, "Triangle: Engineering a 2d quality mesh generator and delaunay triangulator", in *Applied computational geometry towards geometric engineering*, Springer, 1996, pp. 203–222.

[89] S. I. Krasheninnikov, "On scrape off layer plasma transport", *Physics Letters A*, vol. 283, no. 5-6, pp. 368–370, 2001.

[90] J. Graves, J Horacek, R. Pitts, and K. Hopcraft, "Self-similar density turbulence in the tcv tokamak scrape-off layer", *Plasma physics and controlled fusion*, vol. 47, no. 3, p. L1, 2005.

[91] J Neuhauser, W Schneider, R Wunderlich, and K Lackner, "Modelling of impurity flow in the tokamak scrape-off layer", *Nuclear Fusion*, vol. 24, no. 1, p. 39, 1984.

[92] B LaBombard, J. Rice, A. Hubbard, J. Hughes, M Greenwald, J Irby, Y Lin, B Lipschultz, E. Marmar, C. Pitcher, *et al.*, "Transport-driven scrape-off-layer flows and the boundary conditions imposed at the magnetic separatrix in a tokamak plasma", *Nuclear fusion*, vol. 44, no. 10, p. 1047, 2004.

[93] O. Batishchev, S. Krasheninnikov, P. J. Catto, A. Batishcheva, D. Sigmar, X. Xu, J. Byers, T. Rognlien, R. Cohen, M. Shoucri, *et al.*, "Kinetic effects in tokamak scrape-off layer plasmas", *Physics of Plasmas*, vol. 4, no. 5, pp. 1672–1680, 1997.

[94] J Neuhauser, D Coster, H. Fahrbach, J. Fuchs, G Haas, A Herrmann, L Horton, M Jakobi, A Kallenbach, M Laux, *et al.*, "Transport into and across the scrape-off layer in the asdex upgrade divertor tokamak", *Plasma Physics and Controlled Fusion*, vol. 44, no. 6, p. 855, 2002.

[95] J. Mandrekas, "Gtneut: A code for the calculation of neutral particle transport in plasmas based on the transmission and escape probability method", *Computer physics communications*, vol. 161, no. 1-2, pp. 36–64, 2004.

[96] D. Zhang, J. Mandrekas, and W. M. Stacey, "Extensions of the tep neutral transport methodology", *Contributions to Plasma Physics*, vol. 44, no. 1-3, pp. 45–50, 2004.

[97] D. Zhang, J Mandrekas, and W. Stacey, "Higher order approximations of the transmission and escape probability method for neutral particle transport in edge plasmas", *Physics of plasmas*, vol. 13, no. 6, p. 062 509, 2006.

[98] L. Lao, H. S. John, R. Stambaugh, A. Kellman, and W Pfeiffer, "Reconstruction of current profile parameters and plasma shapes in tokamaks", *Nuclear fusion*, vol. 25, no. 11, p. 1611, 1985.